The Impact of Parametrization on Randomized Search Heuristics

Gießen, Christian; Witt, Carsten

Publication date:
2018

Document Version
Publisher's PDF, also known as Version of record

Topological bifurcations of coherent structures and dimension reduction of plasma convection models

Magnus Dam

Kgs. Lyngby 2017
PHD-2017-461

Topological bifurcations of coherent structures and dimension reduction of plasma convection models

Magnus Dam

PhD thesis

Principal supervisor:
Professor Morten Brøns
Technical University of Denmark
Department of Applied Mathematics and Computer Science
Asmussens Allé, Building 303B,
DK–2800 Kgs. Lyngby, Denmark
Email: mobr@dtu.dk

Co-supervisors:
Professor Jens Juul Rasmussen
Technical University of Denmark
Department of Physics
Fysikvej, Building 309,
DK-2800 Kgs. Lyngby, Denmark
Email: jjra@fysik.dtu.dk

Professor Volker Naulin
Technical University of Denmark
Department of Physics
Fysikvej, Building 309,
DK-2800 Kgs. Lyngby, Denmark
Email: vona@fysik.dtu.dk

Department of Applied Mathematics and Computer Science
Technical University of Denmark
DK-2800 Kgs. Lyngby, Denmark
www.compute.dtu.dk

This thesis was set in LaTeX by the author.

ISSN 0909-3192
PHD-2017-461

Summary

Research in fusion energy seeks to develop a clean, safe, and sustainable energy source. Nuclear fusion can be achieved by heating a hydrogen gas to temperatures of millions of kelvin. At fusion temperatures, some or all the electrons leave the atomic nucleus of the hydrogen atom. This results in an overall neutral gaseous state of negatively charged free electrons and positively charged ions. This state of matter is called plasma. To achieve and maintain fusion temperatures, the plasma must avoid direct contact with any solid material. Since the plasma consists of charged particles, it can be confined with an appropriate configuration of strong magnetic fields. Toroidal magnetic confinement devices, such as the tokamak, are the most promising designs for a fusion reactor. A tokamak can operate in two distinct modes of operation. These are the low confinement mode (L-mode) and the high confinement mode (H-mode). H-mode is the preferred operating mode for a fusion reactor. The transition from L-mode to H-mode is called the L–H transition. The confinement properties of a plasma are largely determined by the physics near the edge of the confinement region of the plasma.

The edge transport of a magnetically confined plasma is predominantly caused by recurring bursts of coherent plasma structures. These structures are in L-mode called blob filaments (blobs) and in H-mode categorized into edge localized mode (ELM) filaments or inter-ELM filaments. To improve the plasma confinement, it is important to understand the evolution of these structures. We apply a dynamical systems approach to quantitatively describe the time evolution of these structures. Three state variables describe blobs in a plasma convection model. A critical point of a variable defines a feature point where that variable is significant. For a range of Rayleigh and Prandtl numbers, we analyze the bifurcations of the critical points of the three variables with time as the main bifurcation parameter.

Plasma simulations can be computationally demanding. We apply a Galerkin method to approximate a plasma convection model with a reduced model. The time evolution of the energies of the pressure profile, the turbulent flow, and the zonal flow capture the dynamic behavior of the convection model. Rayleigh decomposition splits the variables of the model into averaged variables and fluctuation variables. We approximate the fluctuation variables by truncated Fourier series and project the equations onto the Fourier basis functions. This results in a computationally simpler model with the spatial dimension reduced by one. Bifurcation diagrams for the energies show consistency between the bifurcation structures of the full and the reduced model.

Finally, we utilize a data-driven modeling approach called SINDy to identify a reduced model from simulation data of a convection model. The reduced model reveals a predator-prey relationship between the zonal flow energy and the turbulent energy. The analytically derived bifurcation diagram for the reduced model has the same structure as the data-based bifurcation diagram for the full model.

Dansk Resumé

Forskning i fusionsenergi søger at udvikle en ren, sikker og bæredygtig energikilde. Kernefusion kan opnås ved at opvarme en hydrogengas til temperaturer på millioner af kelvin. Ved fusionstemperaturer vil nogle af, eller alle, elektronerne forlade hydrogenatomets atomkerne. Dette resulterer i en samlet set neutral gasagtig tilstand af negativt ladede frie elektroner og positivt ladede ioner. Denne tilstandsform kaldes for plasma. For at opnå og opretholde fusionstemperaturer må plasmaet undgå direkte kontakt med ethvert fast materiale. Da plasmaet består af ladede partikler, kan det indesluttes med en passende konfiguration af stærke magnetfelter. Toroidale magnetiske indeslutningsenheder, såsom tokamakken, er de mest lovende designs for en fusionsreaktor. En tokamak kan operere i to forskellige driftstilstande. Disse er lav indeslutningstilstand (L-mode) og høj indeslutningstilstand (H-mode). H-mode er den foretrukne driftstilstand for en fusionsreaktor. Overgangen fra L-mode til H-mode kaldes L–H-overgangen. Et plasmas indeslutningsegenskaber bestemmes i høj grad af fysikken nær kanten af plasmaets indeslutningsområde.

Kanttransporten af et magnetisk indesluttet plasma er overvejende forårsaget af gentagende udbrud af kohærente plasmastrukturer. Disse strukturer kaldes i L-mode for blob-filamenter (blobs) og kategoriseres i H-mode som enten edge localized mode (ELM)-filamenter eller inter-ELM-filamenter. For at forbedre plasmaindeslutningen er det vigtigt at forstå udviklingen af disse strukturer. Vi anvender en fremgangsmåde fra teorien om dynamiske systemer til kvantitativt at beskrive tidsudviklingen af disse strukturer. Tre tilstandsvariable beskriver blobs i en plasmakonvektionsmodel. Et kritisk punkt for en variabel definerer et karakteristisk punkt, hvor denne variabel er signifikant. For en række Rayleigh- og Prandtl-tal analyserer vi bifurkationerne af de kritiske punkter for de tre variable med tiden som hovedbifurkationsparameter.

Plasmasimuleringer kan være beregningsmæssigt krævende. Vi anvender en Galerkin metode til at approksimere en plasmakonvektionsmodel med en reduceret model. Tidsudviklingen af energierne for trykprofilen, den turbulente strømning og zonalstrømningen indfanger konvektionsmodellens dynamiske opførsel. Rayleigh dekomposition opdeler variablene i en plasmakonvektionsmodel i middelvariable og fluktuationsvariable. Vi approksimerer fluktationsvariablene med trunkerede Fourierrækker og projekterer ligningerne på Fourier-basisfunktionerne. Dette resulterer i en beregningsmæssigt simplere model med den rumlige dimension reduceret med én. Bifurkationsdiagrammer for energierne viser sammenfald mellem bifurkationsstrukturerne for den fulde og den reducerede model.

Til sidst gør vi brug af en datadrevet modelleringsmetode kaldet SINDy til at identificere en reduceret model fra simuleringsdata for en konvektionsmodel. Den reducerede model afslører et rovdyr-byttedyr forhold mellem zonalstrømningsenergien og den turbulente energi. Det analytisk udledte bifurkationsdiagram for den reducerede model har den samme struktur som det databaserede bifurkationsdiagram for den fulde model.

Preface

This thesis was prepared at the Department of Applied Mathematics and Computer Science at the Technical University of Denmark in partial fulfillment of the requirements for acquiring the PhD degree. The PhD project was supervised by Professor Morten Brøns, Professor Jens Juul Rasmussen, and Professor Volker Naulin. The PhD scholarship was 2/3 funded by DTU Compute and 1/3 funded by DTU Physics.

The results in Chapter 2 are published in *Physics of Plasmas* [24] coauthored with Jens Juul Rasmussen, Volker Naulin, and Morten Brøns. The results in Chapter 4 are published in *Physics of Plasmas* [23] coauthored with Morten Brøns, Jens Juul Rasmussen, Volker Naulin, and Jan S. Hesthaven.

Acknowledgements

In the spring of 2016 I worked with Professor Jan S. Hesthaven during a research stay at the Institute of Mathematics, EPFL (École Polytechnique Fédérale de Lausanne). I am thankful for the valuable discussions I had with Prof. Jan S. Hesthaven and for the hospitality of the institute. I would like to thank my supervisor Morten Brøns for his mathematical insightfulness that have helped keeping my PhD project on track. I thank Jens Juul Rasmussen for our many lengthy discussions on plasma physics and Volker Naulin for his guidance during the project.

Magnus Dam

Kgs. Lyngby, 14-10-2017

Contents

Chapter 1

Introduction

The main goal for research in controlled nuclear fusion is the development of a clean and sustainable energy source at competitive energy costs. Thermonuclear fusion requires the fusion plasma to be heated to very high temperatures. To achieve these high temperatures, the plasma must avoid direct contact with any solid material. This can be achieved with magnetic plasma confinement. Toroidal confinement devices can operate in the low confinement mode (L-mode) or in the high confinement mode (H-mode). The transition from L-mode to H-mode is called the L–H transition. The level of confinement is largely governed by the dynamics at the plasma edge. The edge transport of plasma is largely caused by recurring bursts of coherent plasma structures. These structures are in L-mode known as blob filaments and in H-mode known as edge localized mode (ELM) filaments or inter-ELM filaments. To improve plasma confinement, it is important to understand the time evolution of these structures. Plasma dynamics is often modeled with a set of fluid equations. Many models exist which describe different types of physics and utilize different approximations. A plasma convection model is one of the simplest models to describe plasma edge dynamics. High computational costs of running fluid simulations motivates the need for reduced plasma models.

1.1 Fusion energy

Population increase and economic growth cause a yearly increase in the world's energy demand. Today, fossil fuels cover the majority of the world's energy consumption. Projections estimate depletion of all readily accessible fossil fuel reserves within the next few hundred years. However, the burning of fossil fuels releases greenhouse gases such as CO_2 into the atmosphere. The higher concentrations of greenhouse gases in the atmosphere cause climate change, which has many environmental consequences. This precipitates the need for an alternative and sustainable energy source. Controlled nuclear fusion has the potential of providing a clean and safe energy source that is practically inexhaustible for humankind [18].

A nuclear fusion reaction is the process in which light nuclei combine to form a heavier one. The mass of a nuclide is less than the sum of the masses of the nucleons of which it is composed. This mass difference is called the mass defect. The mass defect Δm of a nuclide corresponds, by conversion with Einsteins formula $E = (\Delta m)c^2$ (c is the speed of light in vacuum), to the binding energy of the nuclide. The average binding energy per nucleon is largest in nuclides with atomic mass number around 60 and smaller in lighter or heavier nuclides. Therefore, energy is released when light nuclei fuse or heavy nuclei split. The mass defect of a nuclear fusion reaction is the difference between the masses of the fusion reactants and the fusion products. The amount of energy released by nuclear fusion is the mass defect of the reaction converted into energy.

Thermonuclear fusion is the fusion of nuclei at extremely high temperatures. The nuclear force binds the nucleons together in an atomic nucleus. Only within very short distances, the attracting nuclear force is stronger than the repelling electrical force between the positively charged protons in the nucleus. To make two nuclei fuse, it is necessary to bring them so close together that the attractive nuclear force overpowers the repulsive electrical forces between the nuclei. Having sufficient kinetic energy will cause a colliding pair of nuclei to fuse instead of deflecting their trajectories.

When gases are heated to fusion temperatures, the high energy causes some or all the electrons to leave the atomic nucleus. The resulting ionized state is quasineutral, meaning that on a macroscopic scale the density of negative charges is approximately equal to the density of positive charges, but on smaller scales there may be local concentrations of positive or negative charge. The small charged regions give rise to electric fields that accelerate the charged particles, and the resulting currents induce magnetic fields. These electric and magnetic fields affect the motion of other charged particles far away. Such a gaseous state of positive ions and free electrons with quasineutrality and collective interaction between the charged particles is called a plasma.

The easiest accessible nuclear reaction, which will be used in first generation power plants, is the fusion of the two hydrogen isotopes deuterium (hydrogen-2) and tritium (hydrogen-3) to a helium-4 nucleus and a neutron

$$^{2}_{1}\mathrm{H} + ^{3}_{1}\mathrm{H} \longrightarrow ^{4}_{2}\mathrm{He}\,(3.52\,\mathrm{MeV}) + ^{1}_{0}\mathrm{n}\,(14.06\,\mathrm{MeV}).$$

The released energy is carried as kinetic energy by the helium-4 nucleus and the neutron. In comparison with the chemical reaction

$$\mathrm{H_2} + \frac{1}{2}\,\mathrm{O_2} \longrightarrow \mathrm{H_2O} + \text{energy}\,(2.96\,\mathrm{eV}),$$

the energy released by the fusion of two hydrogen nuclei is about a million times greater than this chemical burning of a hydrogen molecule. Deuterium is abundant in nature and can be obtained from sea water. Tritium is radioactive with a half-life of 12.3 years, and naturally occurring tritium is therefore extremely rare on Earth. Tritium can be produced in the fusion reactor by surrounding the plasma with a lithium blanket. When a neutron from the fusion processes hits the lithium blanket, tritium can be produced by one of the following reactions

$$\begin{aligned} ^{6}_{3}\mathrm{Li} + ^{1}_{0}\mathrm{n} &\longrightarrow ^{3}_{1}\mathrm{H} + ^{4}_{2}\mathrm{He} + \text{energy}\,(4.8\,\mathrm{MeV}),\\ ^{7}_{3}\mathrm{Li} + ^{1}_{0}\mathrm{n}\,(2.5\,\mathrm{MeV}) &\longrightarrow ^{3}_{1}\mathrm{H} + ^{4}_{2}\mathrm{He} + ^{1}_{0}\mathrm{n}. \end{aligned}$$

To achieve and maintain the temperatures of hundreds of millions kelvin necessary for thermonuclear fusion, the fusion plasma must avoid direct contact with any solid material. The predominant approaches for plasma confinement in the development of nuclear fusion are inertial confinement and magnetic confinement.

For inertial confinement, an extremely dense and hot plasma is produced within a very short time by using an intense energy driver, making the fusion reaction occur before the plasma starts to expand. This concept is utilized in a hydrogen bomb, where the fusion fuel is compressed and heated with a fission bomb. In laboratory experiments, inertial confinement fusion is obtained by compressing a small solid deuterium-tritium pellet with a high-power laser or particle beam to a particle density 10^3–10^4 times that of the solid pellet. The compression is achieved by irradiating the pellet evenly over its entire surface to form a hot plasma envelope surrounding the pellet. The heated plasma expands explosively. The resulting outward plasma jet compresses the inner pellet. The pellet implosion ignites thermonuclear fusion, which rapidly spreads throughout the compressed pellet.

In the magnetic confinement configuration, the fusion plasma is confined with a strong magnetic field. The magnetic approach is more developed and is for now considered the most promising for energy production [61].

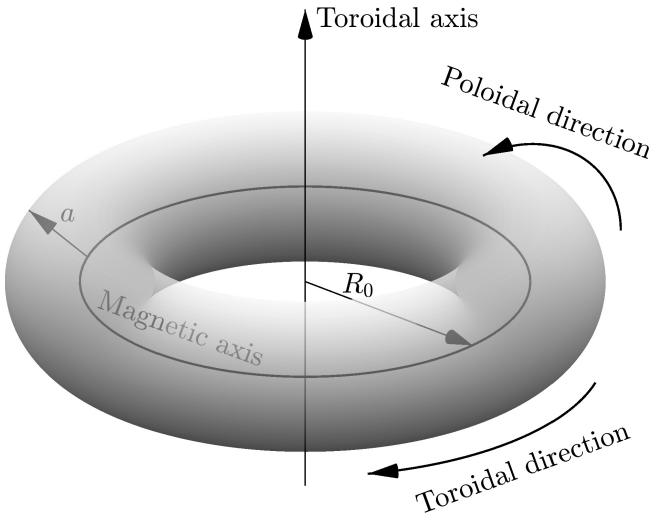

Figure 1.1. Toroidal coordinates. R_0 is the major radius and a is the minor radius.

1.2 Magnetic plasma confinement

A particle of charge q moving with velocity $\boldsymbol{v}$ in the presence of an electric field $\boldsymbol{E}$ and a magnetic field $\boldsymbol{B}$ is subject to the Lorentz force $\boldsymbol{F} = q(\boldsymbol{E} + \boldsymbol{v} \times \boldsymbol{B})$. Since a plasma consists of charged particles, it can be confined by an appropriate arrangement of strong magnetic fields. Magnetic confinement geometries are classified into open end and toroidal configurations.

An open end magnetic field system confines the plasma within a cylinder with magnetic mirrors at each end. Coils wrapped around the cylinder produce a magnetic field along the cylinder. Charged particles with velocity components both parallel and perpendicular to the magnetic field lines will, due to the Lorentz force, change their perpendicular motion into a circular motion called a Larmor motion, while their parallel velocity stays the same. This causes the particles to gyrate about the magnetic field lines in helical orbits. The center of the Larmor motion is called the guiding center. The magnetic mirrors at the open ends repel charged particles. Particles with a large parallel velocity component $v_{\parallel}$, compared to the perpendicular velocity component $v_{\perp}$, will still pass through the open ends making end-losses the most critical issue for open end systems.

A toroidal plasma is a plasma confined in a region with a boundary topologically equivalent to a torus, as shown in Fig. 1.1. A toroid wrapped with coils has in

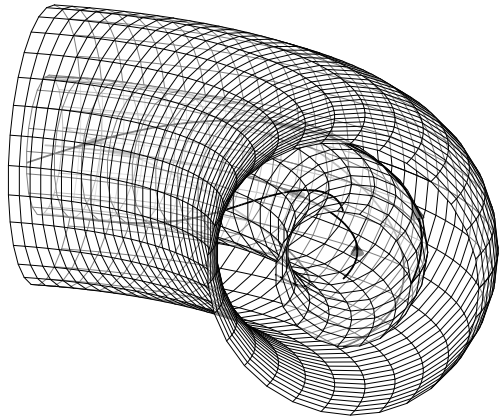

Figure 1.2. The helical magnetic field lines form magnetic surfaces also called flux surfaces. The ions and electrons gyrate about the magnetic field lines.

cylindrical coordinates (R, φ, z) (z-axis is the toroidal axis) the simple toroidal field $\boldsymbol{B} = (0, B_0 R_0/R, 0)$, where R_0 is the major radius, and B_0 is the magnetic field strength on the magnetic axis. Charged particles in such a simple toroidal magnetic field gyrate about the magnetic field lines in helical orbits. The non-uniform magnetic field causes a slow toroidal drift of the guiding centers in the z-direction, where the ions and electrons drift in opposite direction. The resultant charge separation induces an electric field $\boldsymbol{E}$ in the z-direction. This causes an radial outward $\boldsymbol{E} \times \boldsymbol{B}$-drift of both ions and electrons.

To reduce the $\boldsymbol{E} \times \boldsymbol{B}$-drift, a poloidal magnetic field must be applied to bend the magnetic field lines into helices that short-circuit the separated charges. Since the electrons are much lighter and faster than the ions, they are responsible for most of the charge neutralization. The helically shaped magnetic field lines lie in nested toroidal surfaces called magnetic surfaces or flux surfaces, as shown in Fig. 1.2. If there were no radial diffusion, each plasma particle would be trapped to move on the same magnetic surface forever. This is essentially what confines a toroidal plasma.

Toroidal plasma confinement devices may be classified according to the method used to generate the poloidal field. The tokamak (Russian acronym for toroidal chamber with magnetic coils) and reversed field pinch devices induce a toroidal current in the plasma that induces a poloidal magnetic field. In a stellarator, the shape of the coils surrounding the toroid are altered to produce appropriate rotating magnetic field lines [41, 61].

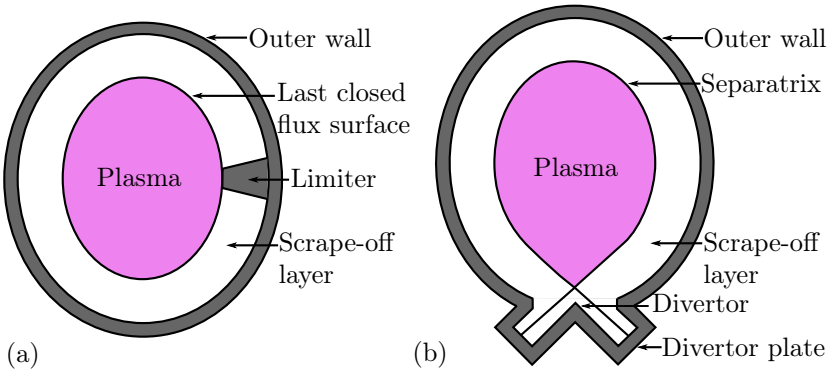

Figure 1.3. Cross sectional view of a toroidal chamber with (a) a limiter and (b) a divertor.

1.3 Plasma edge physics

The level of plasma confinement is largely governed by the plasma dynamics near the plasma edge. This section introduces edge physics phenomena relevant for this project.

1.3.1 Plasma-wall interaction control

Hot plasma striking the reactor walls causes ions from the wall material to diffuse into the plasma. Heavy ions absorb a lot of energy from the light ions and thereby cool the plasma. Two interfaces exist to reduce plasma-wall interaction: the limiter and the divertor. These are illustrated schematically in Fig. 1.3. The limiter configuration is a simple design that isolates the plasma from the first wall by a solid object, called the limiter, protruding from the wall. The last closed flux surface (LCFS) defines the boundary of the confinement region of the plasma, and separates the inside region with closed magnetic surfaces from the outside region with open magnetic surfaces. A divertor configuration modifies the magnetic field to create a magnetic null point in the poloidal magnetic field near the edge of the plasma. A separatrix of the magnetic field line topology constitutes the LCFS. The region of open magnetic field lines outside the separatrix is called the scrape-off layer (SOL). Particles in the SOL follow the open magnetic field lines into the divertor region, where they strike the rapidly cooled divertor plates. In the divertor, the ions and electrons recombine into gas that is pumped out [27].

1.3.2 The L–H transition

Tokamaks have two distinct modes of operation. These are the low confinement mode (L-mode) and the high confinement mode (H-mode). The energy confinement time is about a factor two higher in H-mode than in L-mode. A main parameter that determines which operation mode prevails is the amount of external heating power supplied. For low heating power, tokamaks operate in L-mode. As the external power increases, a transition from L- to H-mode occurs. This transition is called the L–H transition. It was first observed in 1982 at the ASDEX tokamak [70], and has been subsequently observed on all other large tokamaks. In 1993, H-mode was achieved at the W7-AS stellarator [26]. This demonstrated that H-mode is not achievable in only tokamaks, but in all toroidal confinement devices. H-mode is more easily accessible in tokamaks with a divertor than in tokamaks with a limiter [27]. The L–H transition can be either abrupt or have an oscillatory intermediate mode (I-mode).

The L–H transition is caused by the formation of a transport barrier at the plasma edge. The edge transport barrier is a thin layer (in the order of centimeters thick) of highly sheared toroidal flows that significantly reduces the radial diffusion rate. The resulting steepening of the radial pressure gradients within the edge transport barrier builds up a H-mode pedestal, as shown in Fig. 1.4.

Models of the L–H transition [5, 7, 8, 22, 46–48, 59, 60, 79, 80] focus on the interaction between the energies related to the ion pressure gradient P, the turbulence level N, and the zonal flow F. Figure 1.5 shows an example of a solution to the Kim-Diamond model [46, 47] for the L–H transition. In the L-mode, the turbulence builds up with the pressure gradient, but also suppresses the pressure gradient. Reynolds stress transfers turbulent energy to zonal flow energy. This creates a predator-prey relationship between the zonal flow and the turbulence, which results in oscillations in the I-mode. In the quiescent H-mode, the mean flow has become strong enough to fully suppress the turbulence, which further stops the generation of zonal flow. A full bifurcation analysis of the Kim-Diamond model can be found in Ref. [22].

1.3.3 Plasma filaments

Fusion ignition requires a proper balance between the maintenance of a high plasma core temperature and the removal of helium and impurity ions. The edge-SOL transport of a magnetically confined plasma is dominated by recurring bursts of coherent plasma structures. The structures are localized regions in the turbulent flow, which are significantly denser and hotter than the surrounding

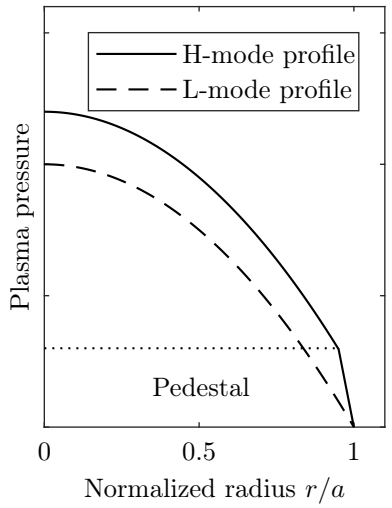

Figure 1.4. Sketch of the radial pressure profile in L-mode and H-mode.

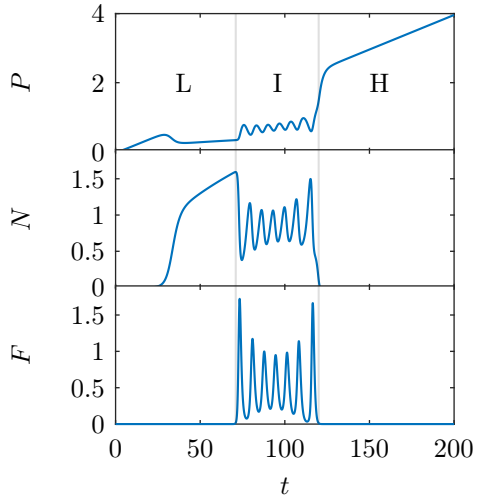

Figure 1.5. A solution example of the Kim-Diamond L–H transition model. P is the ion pressure gradient, N is the turbulence level, and F is the zonal flow shear. The input power is $Q(t) = 0.01t$.

plasma. The plasma structures are in L-mode known as blob filaments (or simply blobs) and in H-mode categorized into edge localized mode (ELM) filaments or inter-ELM filaments. These plasma filaments are highly localized in the plane perpendicular to the magnetic field, and elongate along the magnetic field lines. Blobs form at the outboard mid-plane near the separatrix. The interchange instability causes the formation of finger-like structures that detach from the core plasma and create blobs. The grad-B and curvature drifts, caused by the nonuniform magnetic field, charge polarize the blobs perpendicular to the directions of the magnetic field and the magnetic field variation. The resulting electric field generates an $\boldsymbol{E} \times \boldsymbol{B}$-drift, causing the blob to propagate in the radially outward direction. The blobs propagate far into the scrape-off-layer (SOL) and increase unwanted plasma–wall interactions. Bursts of ELM filaments are caused by a quasi-periodic relaxation of the edge transport barrier, which causes the edge pedestal to collapse. ELM filaments form at the top of the edge pedestal, which typically makes them larger, hotter, and denser than blobs. ELM filaments transport large amounts of energy in short bursts, which can damage the wall components and divertor plates. The time between ELMs is much longer than the duration of an ELM. Inter-ELM filaments form in between ELMs, and are smaller than both ELM and blob filaments [29].

1.4 Fluid simulations of plasma

In a plasma, each particle moves according to the equations of motion $\dot{\boldsymbol{x}} = \boldsymbol{v}$ and $\dot{\boldsymbol{v}} = \frac{q}{m}(\boldsymbol{E} + \boldsymbol{v} \times \boldsymbol{B})$. Besides the external coil generated magnetic field, the interaction of each charged particle with all other charged particles generates complicated electric fields, while currents in the plasma induce magnetic fields. The electric field $\boldsymbol{E}$ and the magnetic field $\boldsymbol{B}$ may be determined from Maxwell's equations. The time evolution of the position and velocity of each particle can be computed from these equations. However, a fusion plasma typically has a number density in the order of $10^{18}\,\mathrm{m}^{-3}$, so solving for each single particle is possible for only tiny volumes of plasma.

In the continuum approximation, a plasma can be described by a set of fluid equations. For each species of particles, let $\boldsymbol{u}$ be the fluid velocity and n the number density. Then, the equations of motion are for each species given by the plasma equation (neglecting collisions and viscosity)

$$mn\left[\frac{\partial \boldsymbol{u}}{\partial t} + (\boldsymbol{u} \cdot \nabla)\boldsymbol{u}\right] = qn(\boldsymbol{E} + \boldsymbol{u} \times \boldsymbol{B}) - \nabla p, \tag{1.1}$$

and the equation of continuity

$$\frac{\partial n}{\partial t} + \nabla \cdot (n\boldsymbol{u}) = 0. \tag{1.2}$$

Maxwell's equations determine the evolution of $\boldsymbol{E}$ and $\boldsymbol{B}$, while the thermodynamic equation of state relates p to n. If we add a viscosity term $mn\nu\nabla^2\boldsymbol{u}$, and remove the magnetoelectric forces in the plasma equation (1.1), we get the Navier-Stokes equation from fluid dynamics [19].

Even the fluid equations are often too computationally demanding to solve, and thus further approximations are necessary. The simplest type of models used to describe plasma edge dynamics are plasma convection models [3, 10, 11, 30, 31, 33, 49–51]. The curvature of the magnetic field creates an effective gravity for the plasma in the outward radial direction. The plasma convection models are similar to the models that describe free convection in fluid dynamics.

A typical example of free convection is when a plane horizontal fluid is heated from below. This type of free convection is called Rayleigh-Bénard convection [37]. Initially, an increasingly hot layer is created near the bottom boundary. Blob formation occurs when a sufficiently high temperature gradient is reached within the bottom boundary layer. Thermal blobs then detach from the heated boundary layer, and advectively transport heat through the upper layers. A possibly unstable pattern of convection rolls form. This type of dynamics is similar to the dynamics observed at the edge of a magnetically confined plasma.

The ESEL (edge-SOL electrostatic turbulence) model by Garcia et al. [34] is an example of a typical model for the dynamics in the edge-SOL region. The model successfully simulates blob formation at the edge of magnetically confined plasma operating in L-mode.

The HESEL (Hot edge-SOL electrostatic) model by Juul Rasmussen et al. [44] is a four-field drift fluid model. The model is capable of simulating an L–H-like transition during increase of the input power. A generalized vorticity included in the model causes the ion pressure curvature to drive a mean flow. This is thought to be a key component for setting up the edge transport barrier that supports the H-mode pedestal.

1.5 Outline of thesis

This project applies methods from dynamical systems theory to analyze plasma convection models. For an introduction to dynamical systems, the textbooks by Meiss [58] or Wiggins [76] are recommended. We aim to introduce a few analysis methods from other fields into the field of plasma physics.

To improve plasma confinement, it is important to better understand the evolution of coherent structures at the edge-SOL. Blob evolution is typically described by visual interpretation of time instant plots of the state variables. Chapter 2 utilizes a method from topological fluid dynamics to quantitatively describe the evolution of plasma blobs.

Fluid simulations of plasma can be computationally demanding. Chapter 3 applies a Galerkin method to reduce the spatial dimension of a plasma convection model from two to one.

Chapter 4 applies a system identification approach to extract an ordinary differential equation (ODE) model from simulation data of a convection model. This effectively reduces the spatial dimension of the model from two to zero.

Chapter 2

Topological bifurcations in the evolution of coherent structures in a convection model

Blob filaments are coherent structures in a turbulent plasma flow. Understanding the evolution of these structures is important to improve magnetic plasma confinement. Three state variables describe blob filaments in a plasma convection model. A dynamical systems approach analyzes the evolution of these three variables. A critical point of a variable defines a feature point for a region where that variable is significant. For a range of Rayleigh and Prandtl numbers the bifurcations of the critical points of the three variables are investigated with time as the primary bifurcation parameter. Bifurcation curves separate the parameter planes into regions with different critical point configurations for the state variables. For the Prandtl number equal to 1, the number of critical points of each state variable increases for an increasing Rayleigh number. For the Rayleigh number equal to 10^4, the number of critical points is greatest for Prandtl numbers of magnitude 10^0.

The results in this chapter are published in Physics of Plasmas [24].

2.1 Introduction

The edge transport of a magnetically confined plasma is dominated by recurring bursts of coherent plasma structures. To improve the plasma confinement, it is crucial to understand the evolution of these structures. The plasma structures are in the low confinement (L-mode) regime known as blob filaments (blobs) and in the high confinement (H-mode) regime categorized as either edge localized mode (ELM) filaments or inter-ELM filaments [28]. Blobs are localized meso-scale coherent structures in a turbulent flow, which are significantly denser and hotter than the surrounding plasma. They are highly localized in the plane perpendicular to the magnetic field and elongate along the magnetic field [21]. Blobs form at the outboard mid-plane near the separatrix. The interchange instability causes the formation of finger-like structures that detach from the core plasma and create blobs [35, 64, 65, 81]. The grad-B and curvature drifts, caused by the nonuniform magnetic field, charge polarize the blobs perpendicular to the directions of the magnetic field and the magnetic field variation. The resulting electric field generates an $\boldsymbol{E} \times \boldsymbol{B}$-drift causing the blob to propagate in the radial outward direction. The blobs propagate far into the scrape-off-layer (SOL) and increase unwanted plasma-wall interactions. During propagation in the SOL, the blobs deform and may lose coherence [1–3, 25, 36, 39, 49–52, 67, 71–73]. The inclusion of finite Larmor radius effects in simulations enhances the blob coherence [43, 55, 66, 75].

References [11, 30, 33] investigate the dependency of the blob position, velocity, and amplitude on Rayleigh and Prandtl numbers in a convection model. To describe the blob evolution, they apply the common practice of visual interpretation of time instant plots of the state variables. In fluid flows, the streamline topology and the vortices can be analyzed using dynamical systems theory [4, 14–16, 42]. This method can analyze the topology of level curves of any function in the plane.

The present chapter applies this dynamical systems approach to quantitatively describe the evolution of plasma blobs. A plasma convection model describes the evolution of seeded blobs. The electrostatic potential ϕ, the thermodynamic variable θ, and the vorticity Ω are the two-dimensional state variables describing the blobs. An extremum of a variable defines a feature point for a region where that variable is significant [45]. Critical points of the electrostatic potential are instantaneous stagnation points for the unsteady plasma flow. Maxima of the thermodynamic variable are feature points for the blob, and the creation of additional maxima indicates the blob splits into smaller blobs. Extrema of vorticity are feature points for vortices. For a range of Rayleigh and Prandtl numbers, we determine for each of the state variables ϕ, θ, and Ω the critical points and their type. We track the evolution, creation, and annihilation of the critical points as time increases.

2.2 Bifurcations of structures

The structure of a fluid flow can be analyzed using dynamical systems theory as described in Refs. [4, 14–16, 42]. In topological fluid dynamics, the analysis is typically based on the stream function, and sometimes on the scalar vorticity, but the same method can be generalized to analyze the topology of any analytically or numerically given function defined on a subset of $\mathbb{R}^2$.

2.2.1 Streamline topology

We consider an incompressible two-dimensional fluid flow. We assume the velocity field $\boldsymbol{v} = (u, v)$ is given from simulation, experiment, or theory. The streamlines are the instantaneous integral curves of $\boldsymbol{v}$. At a given time instant t_0 they are the solution curves $\boldsymbol{x}(s) = (x(s), y(s))$ to the system

$$\frac{d\boldsymbol{x}}{ds} = \boldsymbol{v}(\boldsymbol{x}, t_0). \tag{2.1}$$

The incompressibility of the fluid makes the velocity field divergence free such that $\nabla \cdot \boldsymbol{v} = 0$. Then, a stream function $\psi(x, y)$ exists such that

$$u = \frac{\partial \psi}{\partial y}, \quad v = -\frac{\partial \psi}{\partial x}.$$

The equations for the streamlines now become

$$\frac{dx}{ds} = \frac{\partial \psi}{\partial y}, \qquad \frac{dy}{ds} = -\frac{\partial \psi}{\partial x}. \tag{2.2}$$

This is a Hamiltonian system with Hamiltonian ψ. The stream function ψ is constant along streamlines. Let $(x(s), y(s))$ be a streamline. Then,

$$\frac{d\psi}{ds} = \frac{\partial \psi}{\partial x}\frac{dx}{ds} + \frac{\partial \psi}{\partial y}\frac{dy}{ds} = -vu + uv = 0.$$

Hence, the streamlines lie on the level curves of ψ. The velocity vanishes at the equilibrium points of the Hamiltonian system (2.2), and these points are therefore called stagnation points. A collection of streamlines comprises a streamline pattern. Topological fluid dynamics typically characterizes the flow by carrying out a bifurcation analysis of the system (2.2). If the flow is steady, the bifurcation parameter could be any parameter that the velocity field depends on. If the flow is unsteady, the time instant t_0 could also be included as a bifurcation parameter.

2.2.2 Hamiltonian phase curve topology

We now generalize the concept of analyzing the stream line topology though the stream function, to analyze the topology of any structure through a Hamiltonian. Let $H : M \mapsto \mathbb{R}$ be any analytically or numerically given function defined on a subset of the plane $M \subseteq \mathbb{R}^2$. We assume that H also depends on time t and possibly some system parameters. For our application, H represents the electrostatic potential ϕ, the thermodynamic variable θ, or the vorticity Ω given numerically from simulations. We fix all parameters and consider a single time instant. We consider $H(x, y)$ as a Hamiltonian for the autonomous Hamiltonian system

$$\frac{dx}{ds} = \frac{\partial H}{\partial y}, \qquad \frac{dy}{ds} = -\frac{\partial H}{\partial x}. \tag{2.3}$$

The phase curves of the Hamiltonian system (2.3) lie on the level curves of H,

$$\frac{dH}{ds} = \frac{\partial H}{\partial x}\frac{dx}{ds} + \frac{\partial H}{\partial y}\frac{dy}{ds} = \frac{\partial H}{\partial x}\frac{\partial H}{\partial y} - \frac{\partial H}{\partial y}\frac{\partial H}{\partial x} = 0.$$

A collection of level curves of H comprises the Hamiltonian contour pattern. A point (x^*, y^*) is an equilibrium point of the system (2.3) if and only if it is a critical point (i.e. a minimum, maximum, or saddle) of H. A saddle of H is a saddle point for the corresponding Hamiltonian system (2.3), while a local extremum of H is a center for the corresponding Hamiltonian system (2.3).

The Hamiltonian contour line topology can now be analyzed by carrying out a bifurcation analysis of the system (2.3) with time t and other parameters H might depend on as bifurcation parameters.

2.2.3 Bifurcations of critical points

We want to analyze the bifurcations of the critical points of H. We consider the time as the primary bifurcation parameter and the system parameters as secondary bifurcation parameters.

To describe whether two sets of contour patterns are qualitatively alike we use the notion of topological equivalence [14, 40]:

Definition 2.1 *Topological equivalence:* Two Hamiltonians H and K define topologically equivalent Hamiltonian systems if there exists a homeomorphism h, that maps the trajectories of H onto the phase curves of K. If h is defined in only a subset of the flow domain, H and K define locally topologically equivalent Hamiltonian systems.

This means that Hamiltonian systems with Hamiltonians H and K are topologically equivalent if the contour pattern of H can be continuously deformed into the contour pattern of K. In particular, the Hamiltonians of two topologically equivalent Hamiltonian systems have the same number of critical points of each type. To describe the robustness of a Hamiltonian contour pattern, we use the following definition of structural stability [14, 40]:

Definition 2.2 *Structural stability:* A Hamiltonian H defines a structurally stable Hamiltonian system if for every Hamiltonian K close to H the two systems are topologically equivalent. A Hamiltonian system that is not structurally stable is structurally unstable. A Hamiltonian system is locally structurally stable at (x_0, y_0) if for every Hamiltonian K close to H the two systems are locally topologically equivalent at (x_0, y_0).

The definition says that a Hamiltonian H is structurally stable if every perturbation of H is topologically equivalent to H. The Flow Box Theorem states that the dynamics near a non-equilibrium point is topologically equivalent to the dynamics created by a constant vector field [14]:

Theorem 2.3 (Flow Box Theorem) *Let H be Hamiltonian and let (x_0, y_0) be a regular point for the corresponding Hamiltonian system, such that $\nabla H(x_0, y_0) \neq 0$. Then there exists a neighborhood of (x_0, y_0) where the Hamiltonian system defined by H is topologically equivalent to the system $\dot{x} = 0$, $\dot{y} = 1$.*

The Flow Box Theorem implies that regular points are locally structurally stable. Hamiltonian systems in the plane allow only two types of structurally stable equilibrium points: saddles and centers. A small perturbation of the Hamiltonian near a center or a saddle will make the equilibrium move only slightly, keeping its type. Therefore, only degenerate critical points are locally structurally unstable. A small perturbation of the Hamiltonian near a degenerate critical point cause a local bifurcation.

In the analysis, we encounter three types of bifurcations [13, 15, 40]. The most common bifurcation we observe is the saddle-center bifurcation, where a saddle and a center appear simultaneously through a cusp singularity as a bifurcation parameter μ is varied. This bifurcation is the Hamiltonian analogue to a saddle-node bifurcation. The normal form Hamiltonian for the saddle-center bifurcation is

$$H(x, y) = \frac{a}{2}x^2 + \frac{b}{6}y^3 - \mu x, \tag{2.4}$$

where a, b are constants and μ is the bifurcation parameter. The qualitative changes of the Hamiltonian contour pattern during the bifurcation is shown in

Fig. 2.1(a). The degenerate singularity existing at $\mu = 0$ is called a cusp due to its shape. For $\mu > 0$, a homoclinic orbit of the saddle forms a separatrix around the center.

A Hamiltonian with the symmetry $H(x, y) = H(x, -y)$ allows the Hamiltonian pitchfork bifurcation, where a center bifurcates into a saddle and two centers. The normal form Hamiltonian for the Hamiltonian pitchfork bifurcation is

$$H(x, y) = \frac{a}{2}x^2 + \frac{b}{24}y^4 - \frac{1}{2}\mu y^2, \tag{2.5}$$

where $ab > 0$ and μ is the bifurcation parameter. The qualitative changes of the phase curve pattern during the bifurcation is shown in Fig. 2.1(b). The degenerate singularity existing for $\mu = 0$ is a degenerate center. For $\mu > 0$, two homoclinic orbits of the saddle form separatrices around each center.

A Hamiltonian with the symmetry $H(x, y) = -H(x, -y)$ allows a bifurcation where two saddles and two centers appear simultaneously through a degenerate saddle. We refer to this bifurcation as a duplex saddle-center bifurcation. The normal form Hamiltonian for the duplex saddle-center bifurcation is

$$H(x, y) = ax^2y + by^3 - \mu y, \tag{2.6}$$

where $ab > 0$ and μ is the bifurcation parameter. The qualitative changes of the phase curve pattern during the bifurcation is shown in Fig. 2.1(c). For $\mu > 0$, three heteroclinic orbits form separatrices around the centers [40].

The topological property called the Poincaré index is a useful tool to keep track of equilibria during bifurcations. The index of a node, focus, or center $+1$ and the index of a saddle is -1. The sum of the indices of the equilibria remains constant during a bifurcation [58]. To keep track of the bifurcations, we follow all critical points even when only some types of critical points are of physical interest.

2.3 Convection model

We consider viscous plasma flow in a rectangular domain at the edge of a magnetically confined plasma in the plane perpendicular to the magnetic field $\boldsymbol{B} = B_0\boldsymbol{e}_z$. The flow is described using Cartesian coordinates $(x, y) \in M$, where $M = [-\frac{2}{5}L_x, \frac{3}{5}L_x] \times [-\frac{1}{2}L_y, \frac{1}{2}L_y]$. The normalized $\boldsymbol{E} \times \boldsymbol{B}$ drift velocity field $\boldsymbol{v} = (v_x, v_y)^\intercal$ is

$$\boldsymbol{v} = (\boldsymbol{e}_z \times \nabla\phi)_\perp = \begin{pmatrix} -\partial_y\phi \\ \partial_x\phi \end{pmatrix}. \tag{2.7a}$$

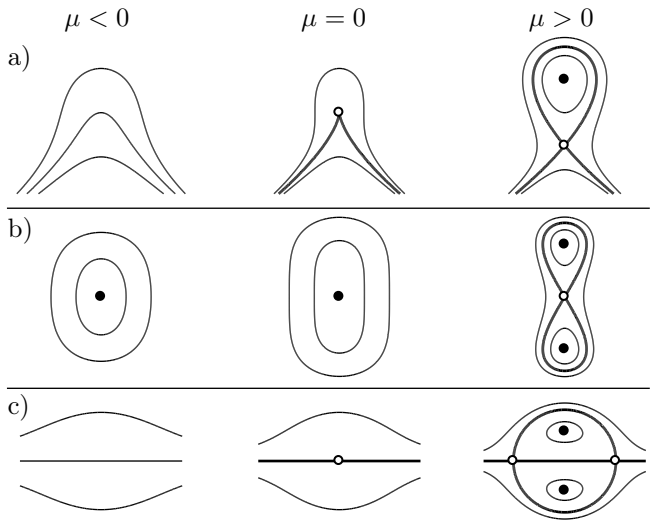

Figure 2.1. The Hamiltonian contour patterns during (a) the saddle-center bifurcation, (b) the Hamiltonian pitchfork bifurcation, (c) the duplex saddle-center bifurcation. The left panel ($\mu < 0$) is before the bifurcation, the middle panel ($\mu = 0$) is at the bifurcation, and the right panel ($\mu > 0$) is after the bifurcation. Filled dots are Lyapunov stable equilibria and unfilled dots are unstable equilibria. Thick lines are separatrices.

Let $\Omega = (\partial_x v_y - \partial_y v_x)$ be the z-component of the normalized vorticity vector $\boldsymbol{\Omega} = \nabla \times B_0 \boldsymbol{v}_E = (\partial_x v_y - \partial_y v_x)\boldsymbol{e}_z$. Then, the normalized electrostatic potential $\phi(x, y, t)$ is obtained from

$$\nabla_\perp^2 \phi = \Omega. \tag{2.7b}$$

To describe the evolution of a generic thermodynamic variable $\theta(x, y, t)$ (e.g. density, pressure, or temperature) and the vorticity $\Omega(x, y, t)$, we employ a normalized convection model

$$\left(\frac{\partial}{\partial t} + \boldsymbol{v} \cdot \nabla_\perp \right) \theta = \kappa \nabla_\perp^2 \theta, \tag{2.7c}$$

$$\left(\frac{\partial}{\partial t} + \boldsymbol{v} \cdot \nabla_\perp \right) \Omega + \frac{\partial \theta}{\partial y} = \nu \nabla_\perp^2 \Omega. \tag{2.7d}$$

Here, κ is the nondimensional diffusion coefficient and ν is the nondimensional viscocity. These coefficients are related to Rayleigh and Prandtl numbers by $\mathrm{Ra} = 1/(\kappa\nu)$ and $\mathrm{Pr} = \nu/\kappa$. We apply zero Dirichlet boundary conditions on all four boundaries for each of the variables ϕ, θ, and Ω. The thermodynamic variable is initialized as a Gaussian function,

$$\theta(x, y, 0) = \exp\left(-\frac{1}{2} \left(x^2 + y^2 \right) \right), \tag{2.8a}$$

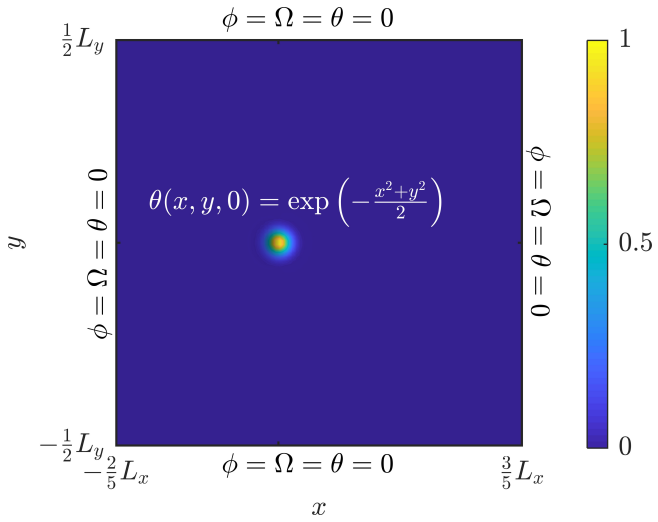

Figure 2.2. The initial condition function $\theta(x, y, 0)$ given by Eq. (2.8a) shown inside the computational domain. The Dirichlet boundary conditions for the problem are shown at each boundary.

while the vorticity and the electrostatic potential are initialized to zero,

$$\phi(x, y, 0) = \Omega(x, y, 0) = 0. \tag{2.8b}$$

Figure 2.2 shows a plot of the initial condition for θ in the computational domain with the boundary conditions written on each boundary.

In Eq. (2.7) the thermodynamic variable has the reflection symmetry $\theta(x, y, t) = \theta(x, -y, t)$, while the electrostatic potential and the vorticity satisfy the symmetry $\phi(x, y, t) = -\phi(x, -y, t)$ and $\Omega(x, y, t) = -\Omega(x, -y, t)$. These symmetries, together with the symmetric initial conditions, imply that θ is symmetric, while Ω and ϕ are antisymmetric for all times.

System (2.7) is one of the simplest models used to describe nonlinear plasma dynamics. References [11, 30, 33] model the evolution of plasma blobs with system (2.7), while Refs. [3, 49–51] use similar convection models also to describe plasma blob evolution.

2.4 Numerical method

We define the size of the computational domain by $L_x = L_y = 50$. This is sufficiently large to ensure that the evolution of the blobs is insignificantly affected by the boundary conditions. To obtain the simulation data, we first fix $\mathrm{Pr} = 1$ and and solve the convection problem (2.7) for numerous Rayleigh numbers. Then, we fix $\mathrm{Ra} = 10^4$ and solve problem (2.7) for numerous Prandtl numbers.

The FEM software package COMSOL Multiphysics® is used as the numerical solver [20]. To obtain the required simulation results with sufficient precision, we use a triangular mesh and activate the adaptive mesh refinement, which automatically refines the mesh in regions with large gradient of θ or Ω. The triangular mesh size is defined with the code

```
model.mesh('mesh1').feature('size').set('table', '
    plasma');
model.mesh('mesh1').feature('size').set('hauto', '1');
```

and the adaptive mesh refinement is activated with

```
model.study('std1').feature('time').set('timeadaption'
    , 'on');
```

The maximum number of mesh refinement iterations is set to 10, and the error estimate is set to depend on the derivatives of both θ and Ω with the code

```
model.sol('sol1').feature('t1').feature('taDef').set('
    ngenlocal',
'10');
model.sol('sol1').feature('t1').feature('taDef').set('
    eefunctime', 'sqrt(comp1.Omegax^2+comp1.Omegay^2) +
     sqrt(comp1.thetax^2+comp1.thetay^2)');
```

An example of the generated adaptive mesh is shown in Fig. 2.3. This mesh contains approximately 3×10^5 domain elements. The relative error tolerance were set to 10^{-6} by

```
model.study('std1').feature('time').set('rtolactive',
    'on');
model.study('std1').feature('time').set('rtol', '1e-6'
    );
```

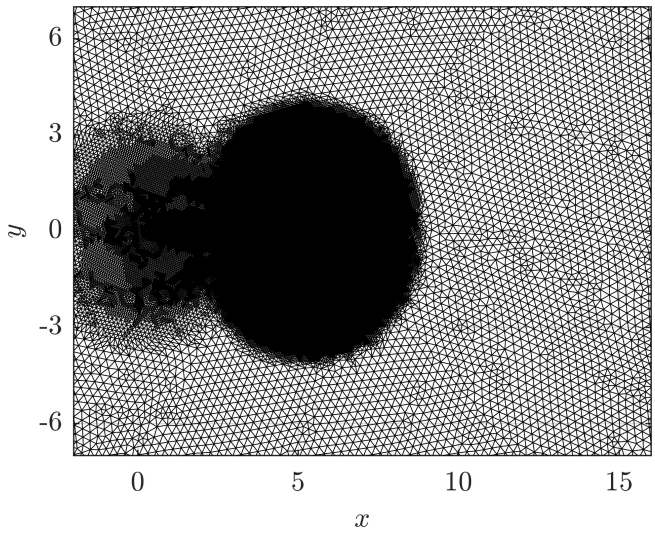

Figure 2.3. A zoom in of the adaptive mesh for the $(\mathrm{Pr}, \mathrm{Ra}) = (1, 10^4)$ solution at $t = 10$. The mesh is greatly refined where the gradients of θ or Ω are large.

The convection problem is initialized at $t = 0$, and runs with output time steps of $\Delta t = 0.05$ until $t = 20$. The mesh reinitializes and iteratively refines, at $t = 0, 2, \ldots, 18$, for a total of 10 times during each simulation.

In the analysis, we track the evolution, creation, and annihilation of the critical points of ϕ, θ, and Ω. The eigenvalues determine whether a critical point is a saddle, maximum, or minimum. For each simulation, we determine the critical points of ϕ, θ, and Ω numerically as follows: The nullclines of the Hamiltonian system (2.3) are

$$N_x = \{(x, y) \in M \,|\, \partial_y H(x, y) = 0\},$$
$$N_y = \{(x, y) \in M \,|\, \partial_x H(x, y) = 0\}.$$

Here, H represents either ϕ, θ, or Ω at a fixed time t. The set of critical points of H is $N_x \cap N_y$. To numerically determine the set of critical points, we first compute N_y. Points in regions where θ is smaller than 1% of $\theta_{\max} = \max_{(x,y)\in M} \theta(x, y, t)$ are removed from N_y. These regions contain very few particles or little energy and are therefore physically uninteresting. The nullcline set N_y consists of a number of parametrized curve segments $\gamma_i(s)$, $i = 1, \ldots, N$. Along each curve segment we compute $\partial_y H(\gamma_i(s))$ and determine the values of s_j for which $\partial_y H(\gamma_i(s_j)) = 0$. These zeros are found by finding indices j for which $\partial_y H(\gamma_i(s_j))$ subsequently changes sign,

$$\partial_y H(\gamma_i(s_j)) \partial_y H(\gamma_i(s_{j+1})) < 0.$$

The corresponding points $\gamma_i(s_j)$ are the critical points of H. The type of a critical point of H is determined from the eigenvalues $\lambda_{1,2}$ of the Hessian matrix of H evaluated in the critical point. The Hessian matrix of H is

$$\mathcal{D}^2 H = \begin{pmatrix} H_{xx} & H_{xy} \\ H_{yx} & H_{yy} \end{pmatrix}.$$

Let $\tau = \operatorname{tr}(\mathcal{D}^2 H) = H_{xx} + H_{yy}$ be the trace and $\delta = \det(\mathcal{D}^2 H) = H_{xx}H_{yy} - H_{xy}^2$ be the determinant of $\mathcal{D}^2 H$. Then the eigenvalues of $\mathcal{D}^2 H$ are $\lambda_\pm = \frac{1}{2}\left(\tau \pm \sqrt{\tau^2 - 4\delta}\right)$. Since $\mathcal{D}^2 H$ is symmetric, $\mathcal{D}^2 H = (\mathcal{D}^2 H)^\intercal$, both eigenvalues are real. The critical point is a saddle if λ_1 and λ_2 are of opposite sign, a local maximum if $\lambda_{1,2}$ are both negative, a local minimum if $\lambda_{1,2}$ are both positive, and a degenerate point if either λ_1 or λ_2 is zero. Hence, in the (τ, δ)-plane there are four different eigenvalue regions separated by lines at $\delta = 0$ and $\{\tau = 0 \,|\, \delta > 0\}$:

$$\begin{cases} \text{Saddle} & \text{for } \delta < 0 \ (\lambda_+\lambda_- < 0), \\ \text{Degenerate point} & \text{for } \delta = 0 \ (\lambda_+\lambda_- = 0), \\ \text{Local maximum} & \text{for } \delta > 0 \text{ and } \tau < 0 \ (\lambda_\pm < 0), \\ \text{Local minimum} & \text{for } \delta > 0 \text{ and } \tau > 0 \ (\lambda_\pm > 0). \end{cases} \tag{2.9}$$

The critical points are categorized as saddles, maxima or minima according Eq. (2.9). Fig. 2.4 shows an example of a scalar vorticity function at a time instant overlayed by the nullclines and equilibrium points for the corresponding Hamiltonian system.

2.5 Bifurcation analysis

This section analyzes the bifurcations of the critical points of the electrostatic potential ϕ, the thermodynamic variable θ, and the vorticity Ω as time increases from $t = 0$ to $t = 20$ for a range of Rayleigh and Prandtl numbers. We use the same set of simulation data for the analysis of ϕ, θ, and Ω. We first fix $(\mathrm{Pr}, \mathrm{Ra}) = (1, 10^4)$ and track the evolution, creation, and annihilation of the critical points as time evolves. We then fix $\mathrm{Pr} = 1$ and track the creation and annihilation of the critical points for numerous Rayleigh numbers in the range $\mathrm{Ra} \in [10, 10^5]$. Similarly, we fix $\mathrm{Ra} = 10^4$ and track the creation and annihilation of the critical points for numerous Prandtl numbers in the range $\mathrm{Pr} \in [10^{-3}, 10^4]$. We draw the bifurcation curves in the (t, Ra)- and (t, Pr)-parameter planes.

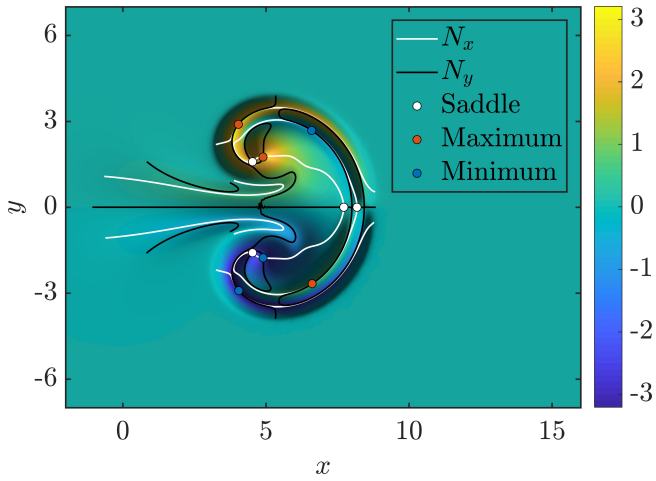

Figure 2.4. A zoom in of the instant vorticity $\Omega(x, y, t)$ for the $(\mathrm{Pr}, \mathrm{Ra}) = (1, 10^4)$ solution at $t = 10$. The white curves are the x-nullcline, the black curves are the y-nullcline, and the extremum points are marked in their intersection points.

2.5.1 Critical points of the electrostatic potential

The electrostatic potential defines the velocity field of a plasma flow analogous to the way the stream function defines the velocity field of a fluid flow. The critical points of ϕ define the instantaneous stagnation points of the flow.

Figure 2.5 shows representative time instant plots of ϕ for three different critical point configurations labeled ①–③ superimposed by the contour patterns of ϕ. The symmetry $\phi(x, y, t) = -\phi(x, -y, t)$ causes the x-axis to be the zero level set and imposes a symmetry of the critical points such that we can limit our comments to bifurcations in the upper half-plane (uhp). Table 2.1 characterizes the different critical point configurations of ϕ by the number of each type of critical point.

For $(\mathrm{Pr}, \mathrm{Ra}) = (1, 10^4)$, we consider $\phi(x, y, t)$ with time $t \in [0, 20]$ as a bifurcation parameter. Figure 2.6 shows the physical positions of all critical points of ϕ plotted with t as an external parameter. All critical points are constantly moving to the right with nonconstant velocity. Hence, the x-coordinates of the critical point positions are monotonically increasing functions of t. The bifurcation diagram in Fig. 2.7 shows the y-coordinates of the critical points of ϕ as functions of t. The electrostatic potential ϕ is initialized to zero, but quickly a minimum emerges at $(x, y) \approx (0, 1.58)$ such that ϕ has the configuration ①. At $t = 10.13$, a saddle-center bifurcation creates a saddle and a minimum changing

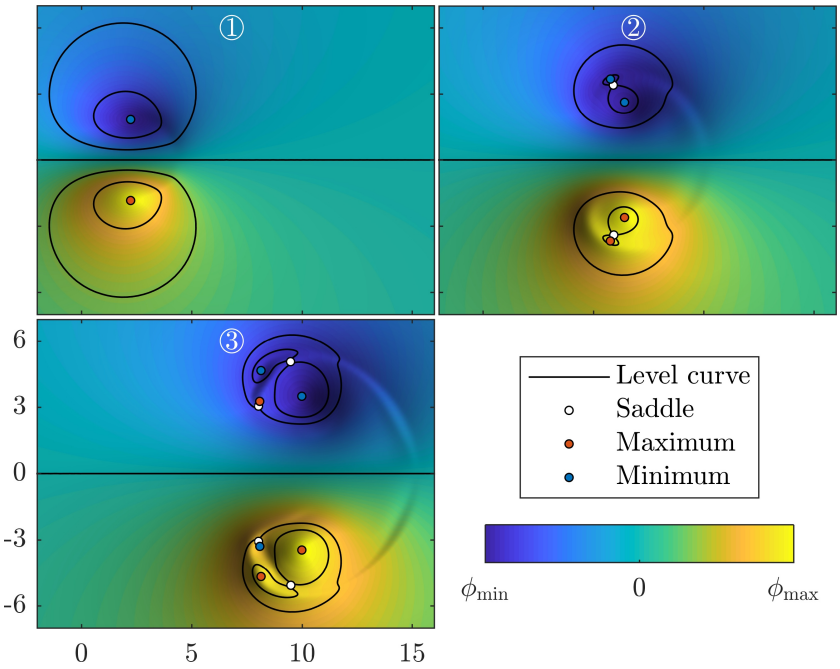

Figure 2.5. Representative critical point configurations for ϕ corresponding to different level curve topologies of ϕ.

Critical points of ϕ	①	②	③
Saddles in uhp and lhp	0	1	2
Max in uhp and min in lhp	0	0	1
Min in uhp and max in lhp	1	2	2
Total (uhp+lhp)	2	6	10

Table 2.1. Number of saddles, maxima (max), and minima (min) in the upper half-plane (uhp) and the lower half-plane (lhp) for the different critical point configurations of ϕ shown in Fig. 2.5. The index +2 is preserved.

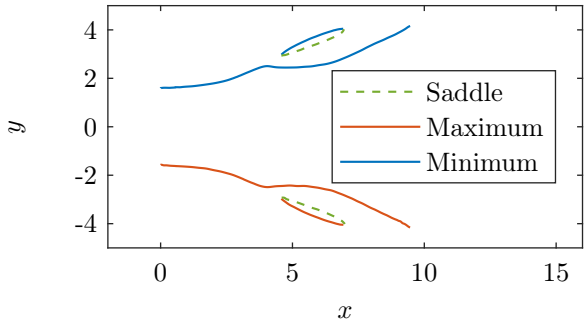

Figure 2.6. The physical position of all critical points of ϕ for $(\mathrm{Pr}, \mathrm{Ra}) = (1, 10^4)$ and with time $t \in [0, 20]$ as external parameter.

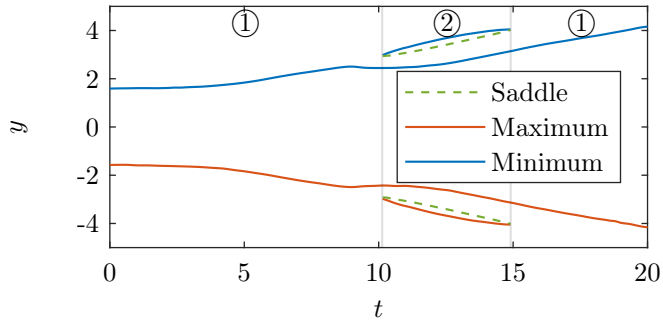

Figure 2.7. Bifurcation diagram showing the y-coordinates of all critical point of ϕ for $(\mathrm{Pr}, \mathrm{Ra}) = (1, 10^4)$ and time as bifurcation parameter. Saddle-center bifurcations occur at $t = 10.13$ and $t = 14.91$. The different critical point configurations of ϕ are shown in Fig. 2.5.

Critical points of θ	①	②	③	④	⑤	⑥	⑦	⑧
Saddles in uhp and lhp	0	1	2	2	1	3	0	2
Max in uhp and lhp	0	1	2	3	2	3	1	2
Min in uhp and lhp	0	0	0	0	0	1	0	1
Saddles on the x-axis	0	0	0	1	1	1	1	1
Max on the x-axis	1	1	1	0	0	0	0	0
Total (uhp+lhp+x-axis)	1	5	9	11	7	15	3	11

Table 2.2. Number of saddles, maxima (max), and minima (min) in the upper half-plane (uhp) and the lower half-plane (lhp) for the different critical point configurations of θ shown in Fig. 2.9. The index +1 is preserved.

the configuration to ②. At $t = 14.91$, this saddle and minimum vanish again in a saddle-center bifurcation and ϕ has again the configuration ①.

We fix $\mathrm{Pr} = 1$, and for numerous Rayleigh numbers, we determine all bifurcation values of t for the critical points of ϕ. Then, we fix $\mathrm{Ra} = 10^4$, and for numerous Prandtl numbers, we determine all bifurcation values of t. Figure 2.8 shows the bifurcation curves in the (t, Ra)- and (t, Pr)-planes. Two types of saddle-center bifurcations are observed: The saddle-center bifurcation (min) creates or annihilates a saddle and a minimum in the upper half-plane, while the saddle-center bifurcation (max) creates or annihilates a saddle and a maximum in the upper half-plane. The bifurcation curves divide these sections of the parameter planes into regions with configurations ①–③. For fixed $\mathrm{Pr} = 1$, no bifurcations occur for $\mathrm{Ra} \lesssim 5.1 \times 10^3$. The number of critical points of ϕ increases for an increasing Rayleigh number. For fixed $\mathrm{Ra} = 10^4$, no bifurcations occur for $\mathrm{Pr} \lesssim 3.0 \times 10^{-1}$ or $\mathrm{Pr} \gtrsim 9.0$.

2.5.2 Critical points of the thermodynamic variable

The thermodynamic variable defines the physical shape of the blob. A maximum of θ is a feature point for the blob. The creation of additional maxima indicates the blob splits into smaller blobs. We can use the number of maxima of θ as a measure for the level of coherence of a blob. A blob with a single maximum is a fully coherent blob and a blob with more maxima is less coherent.

Figure 2.9 shows representative time instant plots of θ for different critical point configurations labeled ①–⑧. Table 2.2 characterizes the different configurations of θ by the number of each type of critical point.

Figure 2.10 shows for $(\mathrm{Pr}, \mathrm{Ra}) = (1, 10^4)$ the positions of all critical points of θ in physical space plotted with t as an external parameter. The bifurcation

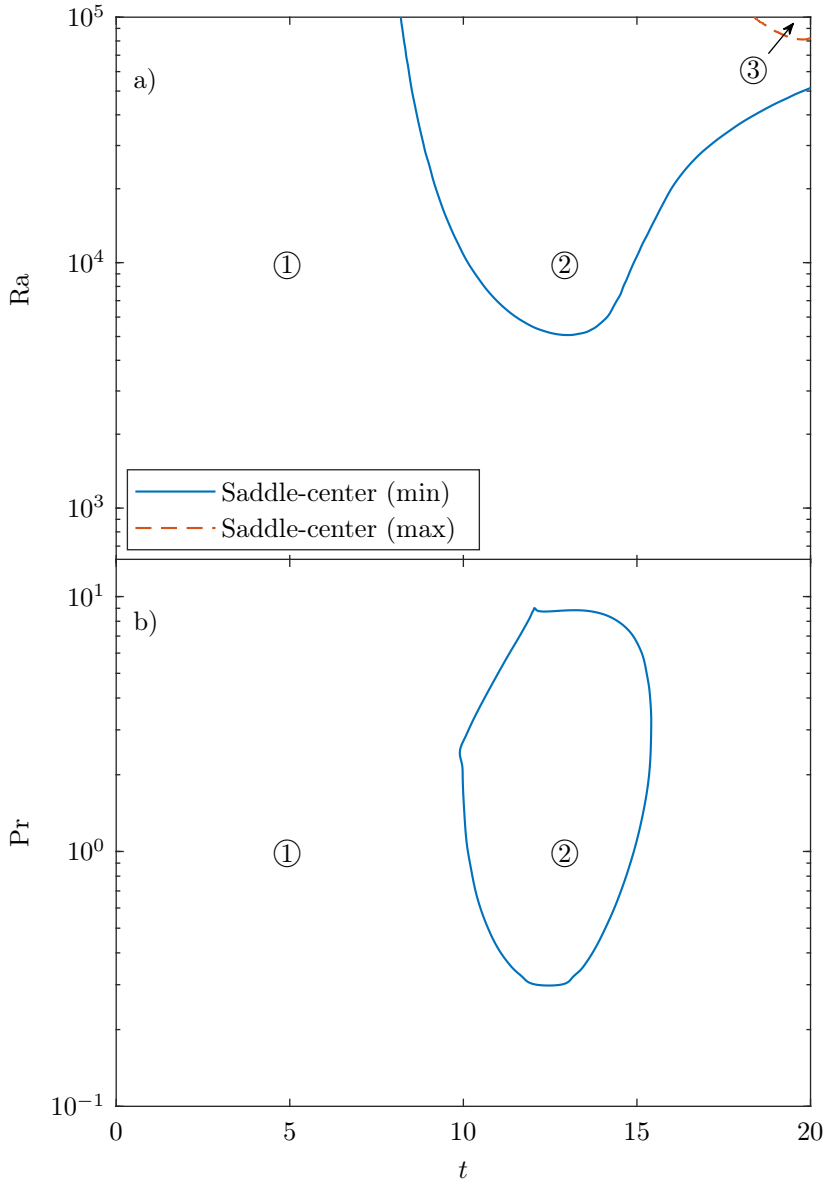

Figure 2.8. Bifurcation curves for the critical points of ϕ in a) the (t, Ra)-parameter plane for $\mathrm{Pr} = 1$, b) the (t, Pr)-parameter plane for $\mathrm{Ra} = 10^4$. The different critical point configurations of ϕ are shown in Fig. 2.5.

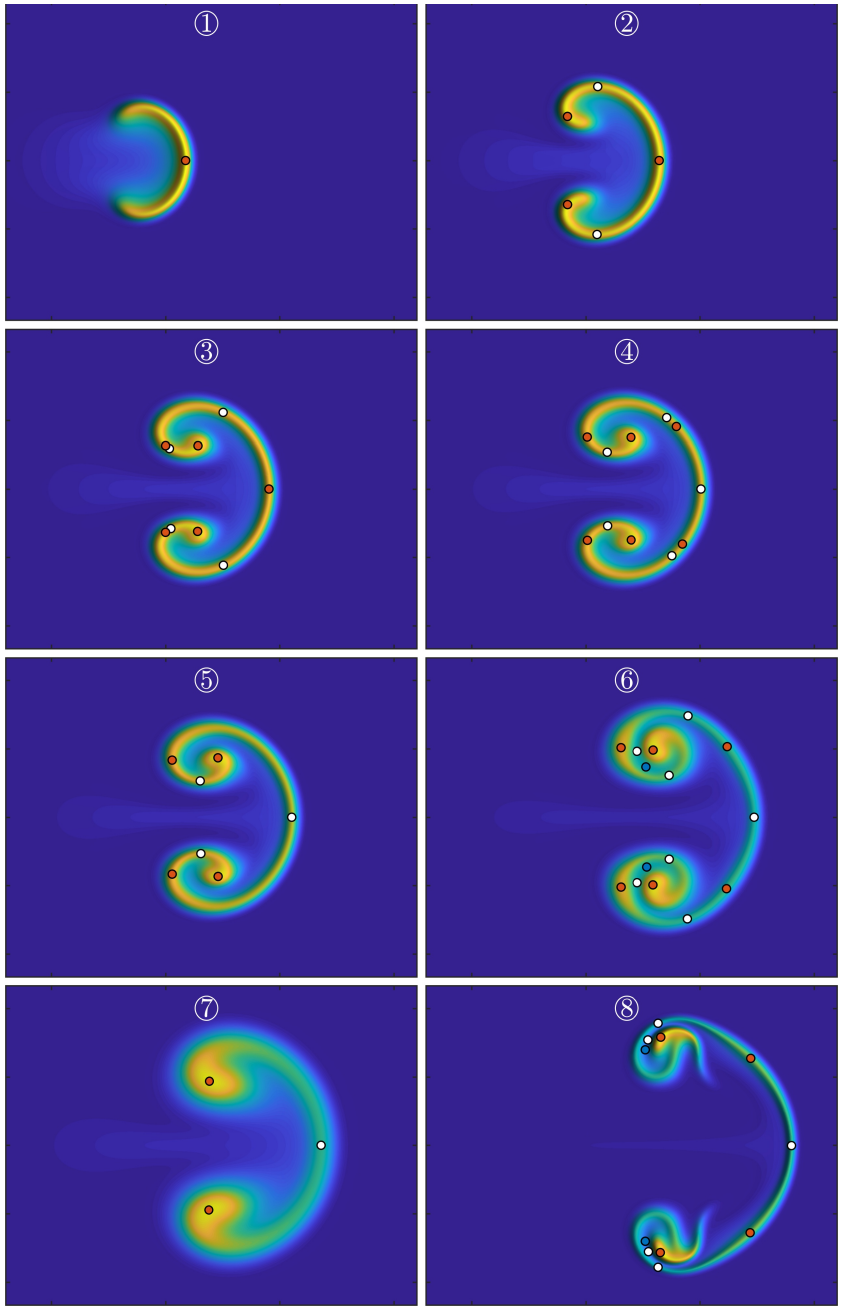

Figure 2.9. Representative critical point configurations for θ.

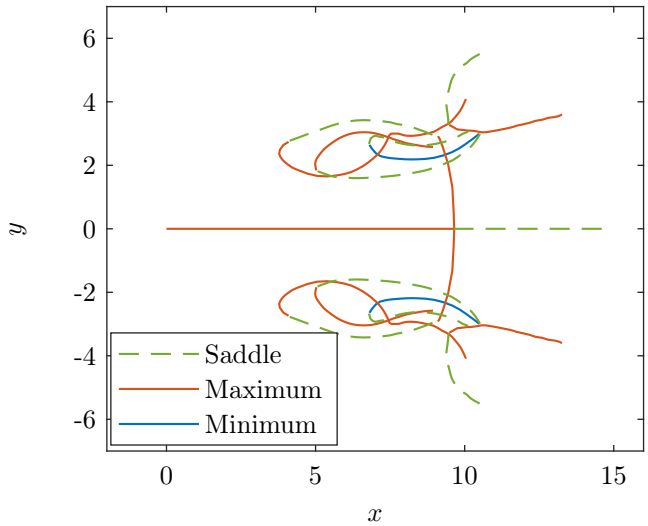

Figure 2.10. The physical position of all critical points of θ for $(\mathrm{Pr}, \mathrm{Ra}) = (1, 10^4)$ and with time $t \in [0, 20]$ as external parameter.

diagram in Fig. 2.11 shows for $(\mathrm{Pr}, \mathrm{Ra}) = (1, 10^4)$ the y-coordinates of the critical points of θ as functions of t. The thermodynamic variable θ is initialized with a maximum at $(x, y) = (0, 0)$ corresponding to the critical point configuration ①. Saddle-center bifurcations at $t = 8.55$ and $t = 11.69$ change the critical point configuration to ② and further to ③. At $t = 11.91$, a Hamiltonian pitchfork bifurcation, allowed by the reflection symmetry, changes the critical point configuration to ④. Four more saddle-center bifurcations bring the critical point configuration through ⑤–④–⑥–④.

Figure 2.12 shows the bifurcation curves in the (t, Ra)- and (t, Pr)-planes. We observe three types of bifurcations: The saddle-center bifurcation (max) creates or annihilates a saddle and a maximum in the upper and lower half-plane, the saddle-center bifurcation (min) creates or annihilates a saddle and a minimum in the upper and lower half-plane, and the Hamiltonian pitchfork bifurcation splits a maximum on the x-axis into a saddle on the x-axis and two maxima symmetrically located in the upper and lower half-plane. The first bifurcation marks the time the blob starts to lose coherence. For $\mathrm{Pr} = 1$, no bifurcations occur for $\mathrm{Ra} \lesssim 5.3 \times 10^1$. The number of critical points increases with an increasing Rayleigh number. For $\mathrm{Ra} = 10^4$, no bifurcations occur for $\mathrm{Pr} \lesssim 1.1 \times 10^{-3}$ or $\mathrm{Pr} \gtrsim 1.5 \times 10^3$. The number of critical points of θ is greatest for Prandtl numbers of magnitude 10^0. Hence, blobs stay more coherent for small Rayleigh numbers, and for small or large Prandtl numbers.

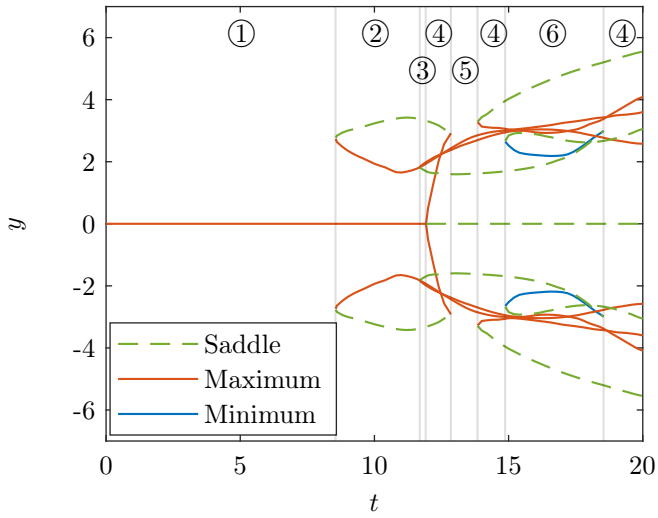

Figure 2.11. Bifurcation diagram showing the y-coordinates of all critical points of θ for $(\mathrm{Pr}, \mathrm{Ra}) = (1, 10^4)$ and time as bifurcation parameter. Saddle-center bifurcations occur at $t = 8.55$, 11.69, 12.85, 13.84, 14.87, 18.54, and a Hamiltonian pitchfork bifurcation occurs at $t = 11.91$. The different critical point configurations of θ are shown in Fig. 2.9.

2.5.3 Critical points of the vorticity

The extrema of Ω define vortex centers and are feature points of the vortices. A typical vortex analysis follows the full evolution of the vortical regions enclosed by separatrices. Here, we simply track the evolution of the extrema of vorticity, and in this way, disregard all information about the actual vortex shape. The sign of vorticity in an extremum defines the direction of rotation for the vortex.

Figure 2.13 shows representative time instant plots of Ω for different critical point configurations labeled ①–⑧. The symmetry $\Omega(x, y, t) = -\Omega(x, -y, t)$ causes the x-axis to be a zero level set and imposes a symmetry of the critical points such that we can limit our comments to bifurcations in the upper half-plane and on the x-axis. Table 2.3 characterizes the different configurations of Ω by the number of each type of critical point.

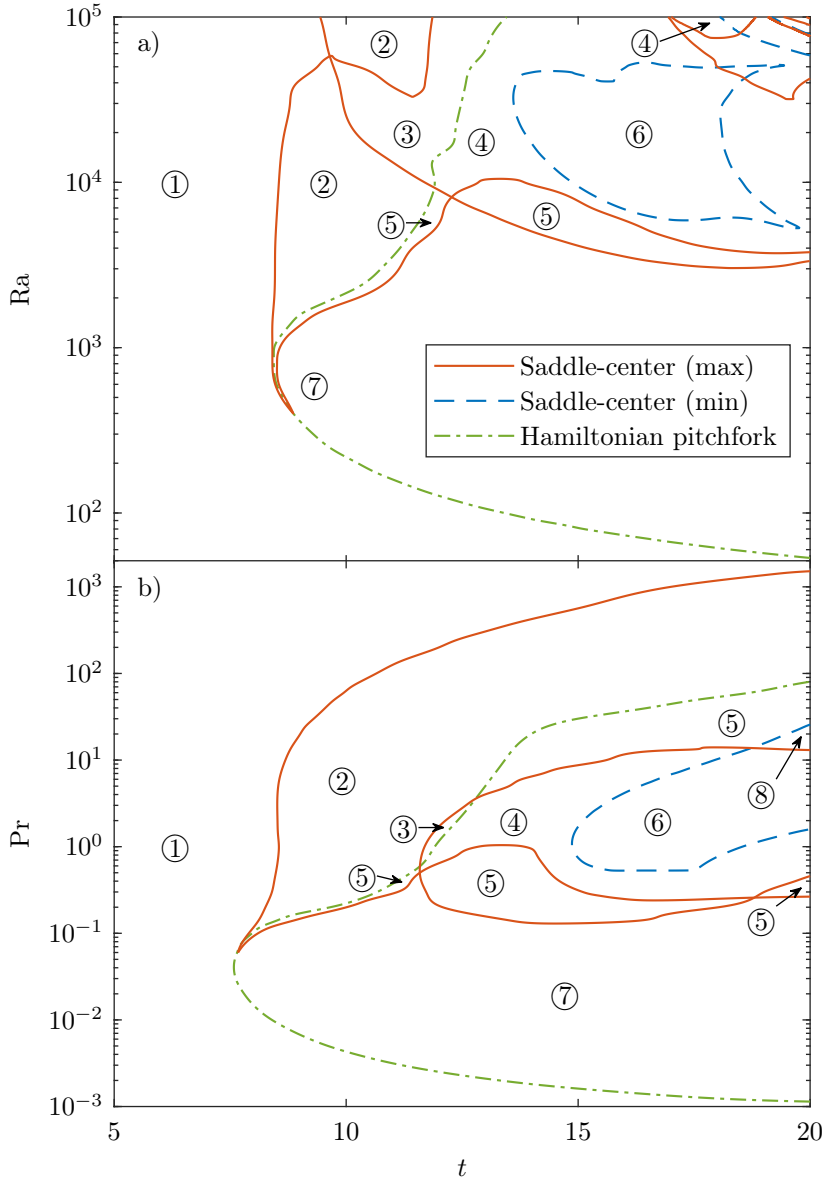

Figure 2.12. Bifurcation curves for the critical points of θ in a) the (t, Ra)-parameter plane for $\mathrm{Pr} = 1$, b) the (t, Pr)-parameter plane for $\mathrm{Ra} = 10^4$. The different critical point configurations of θ are shown in Fig. 2.9.

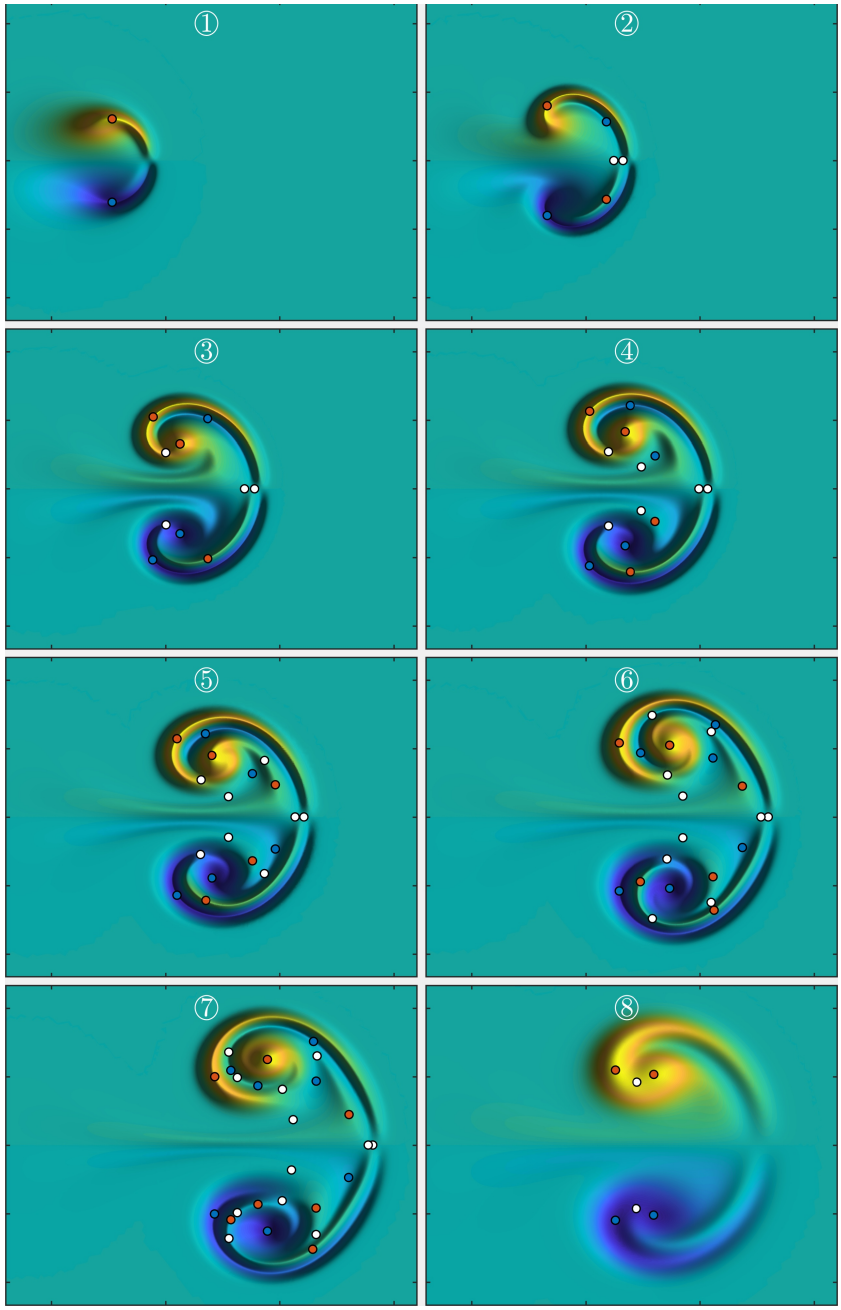

Figure 2.13. Representative critical point configurations for Ω.

Critical points of Ω	①	②	③	④	⑤	⑥	⑦	⑧
Saddles in uhp and lhp	0	0	1	2	3	4	5	1
Max in uhp and min in lhp	1	1	2	2	3	3	3	2
Min in uhp and max in lhp	0	1	1	2	2	3	4	0
Saddles on the x-axis	0	2	2	2	2	2	2	0
Total (hhp+lhp+x-axis)	2	6	10	14	18	22	26	6

Table 2.3. Number of saddles, maxima (max), and minima (min) in the upper half-plane (uhp) and the lower half-plane (lhp) for the different critical point configurations of Ω shown in Fig. 2.13. The index +2 is preserved.

Figure 2.14 shows for $(\mathrm{Pr}, \mathrm{Ra}) = (1, 10^4)$ the positions of all critical points of Ω in physical space plotted with t as an external parameter. The bifurcation diagram in Fig. 2.15 shows for $(\mathrm{Pr}, \mathrm{Ra}) = (1, 10^4)$ the y-coordinates of the critical points of Ω as functions of t. The vorticity Ω is initialized to zero, but a maximum at $(x, y) \approx (0.0, 1.0)$ quickly emerges giving Ω the critical point configuration ①. A duplex saddle-center bifurcation, allowed by the symmetry $\Omega(x, y, t) = -\Omega(x, -y, t)$, changes the configuration to ②. A series of saddle-center bifurcations then creates or annihilates saddles and extrema, which changes the critical point configuration through ③–④–⑤–⑥–⑦–⑥.

Figure 2.16 shows the bifurcation curves for the critical points of Ω in the (t, Ra)- and (t, Pr)-planes. Three types of bifurcations are observed: The saddle-center bifurcation (max) creates or annihilates a saddle and a maximum in the upper half-plane, the saddle-center bifurcation (min) creates or annihilates a saddle and a minimum in the upper half-plane, and the duplex saddle-center (min) creates two saddles on the x-axis, a minimum in the upper half-plane and a symmetrically located maximum in the lower half-plane. For $\mathrm{Pr} = 1$, no bifurcations occur for $\mathrm{Ra} \lesssim 6.5 \times 10^2$. For $\mathrm{Ra} = 10^4$, no bifurcations occur for $\mathrm{Pr} \lesssim 8.0 \times 10^{-3}$ or $\mathrm{Ra} \gtrsim 2.8 \times 10^3$.

2.5.4 Discussion

The diagrams in Figs. 2.8, 2.12, and 2.16 follow qualitatively the same pattern: For $\mathrm{Pr} = 1$, the number of critical points increases for an increasing Rayleigh number and for $\mathrm{Ra} = 10^4$, the number of critical points is greatest for Prandtl numbers of magnitude 10^0. The electrostatic potential ϕ is at each time instant related to the vorticity Ω by Eq. (2.7b). However, the vorticity has many more critical points than the electrostatic potential. A quantitative comparison of the three diagrams show no direct relation between the bifurcation values of t at which critical points are created or annihilated. Hence, the analysis of

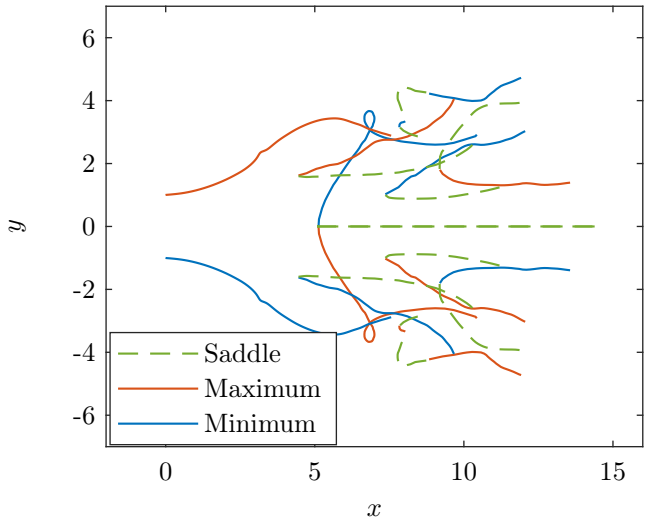

Figure 2.14. The physical position of all critical points of Ω for $(\mathrm{Pr}, \mathrm{Ra}) = (1, 10^4)$ and with time $t \in [0, 20]$ as external parameter.

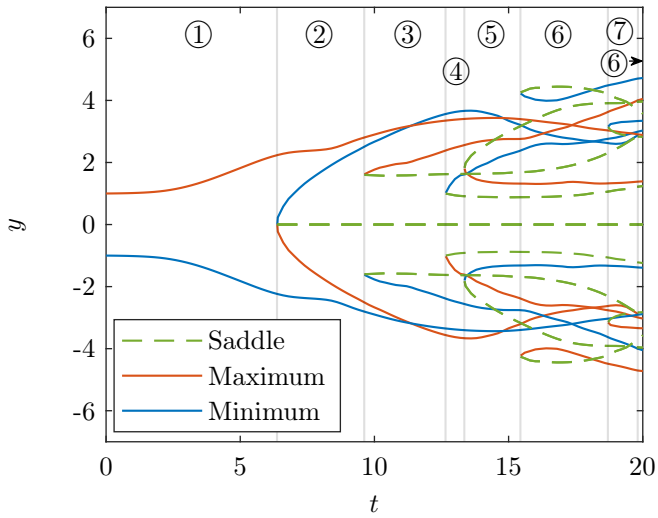

Figure 2.15. Bifurcation diagram showing the y-coordinates of all critical points of Ω for $(\mathrm{Pr}, \mathrm{Ra}) = (1, 10^4)$ and time as bifurcation parameter. A duplex saddle-center bifurcation occurs at $t = 6.37$ and saddle-center bifurcations occur at 9.62, 12.65, 13.35, 15.44, 18.70, and 19.81. The different critical point configurations of Ω are shown in Fig. 2.13.

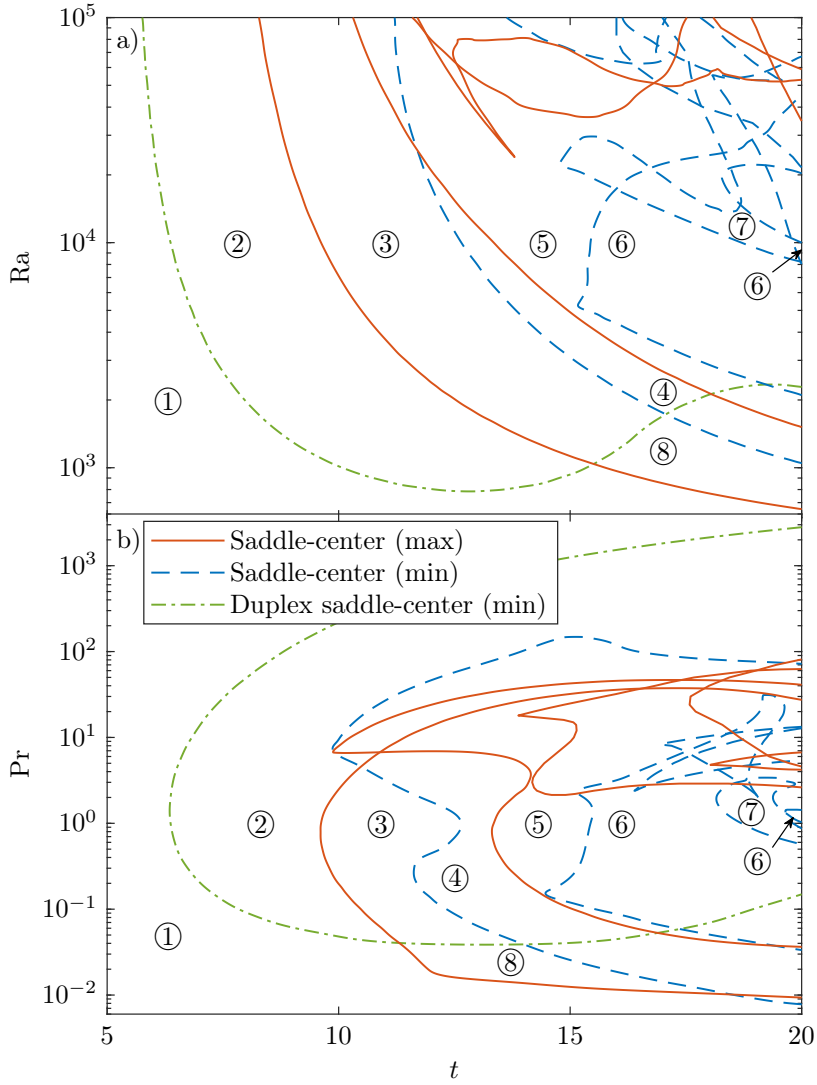

Figure 2.16. Bifurcation curves for the critical points of Ω in a) the (t, Ra)-parameter plane for $\mathrm{Pr} = 1$, b) the (t, Pr)-parameter plane for $\mathrm{Ra} = 10^4$. The different critical point configurations of Ω are shown in Fig. 2.13.

one state variable characterizes only the configurations of the feature points corresponding to that variable. The analysis restricts to $\mathrm{Ra} \leq 10^5$ and $t \leq 20$. By simultaneously increasing Ra and t further beyond these values, the number of bifurcations grows to the extent that it becomes both impractical and of limited interest to systematically track and distinguish the different bifurcations. The present method is unsuitable to describe structures in such a turbulent flow.

2.6 Conclusion

A convection model, with Rayleigh number, Ra, and Prandtl number, Pr, as parameters, describes the evolution of two-dimensional seeded plasma blobs. The blobs are described in terms of three variables: the electrostatic potential ϕ, the thermodynamic variable θ, and the vorticity Ω. The critical points of a variable define feature points where that variable is significant. Extrema of the electrostatic potential define stagnation points. Maxima of the thermodynamic variable are feature points for the blob such that the creation of additional maxima indicates a splitting of the blob into smaller blobs. Extrema of vorticiy are feature points for vortices.

We apply a dynamical systems approach to analyze bifurcations of the critical points of ϕ, θ, and Ω with time, $t \in [0, 20]$ as the primary bifurcation parameter. We fix the Prandtl number to $\mathrm{Pr} = 1$ and consider the Rayleigh number as an additional bifurcation parameter. We then fix the Rayleigh number to $\mathrm{Ra} = 10^4$ and use the Prandtl number as an additional bifurcation parameter. The bifurcation curves separate the parameter planes into multiple regions with different critical point configurations. The diagrams reveal that for $\mathrm{Pr} = 1$, the number of critical points of ϕ, θ, and Ω increases for an increasing Rayleigh number. For $\mathrm{Ra} = 10^4$, the number of critical points is greatest for Prandtl numbers of magnitude 10^0.

We have demonstrated that a bifurcation analysis of the critical points is a feasible method to quantitatively describe the evolution of coherent structures in a plasma physics convection model.

Chapter 3

Galerkin dimension reduction of plasma convection models

Plasma simulations can be computationally demanding. This complicates parameter dependency analysis of model solutions. We apply a Galerkin method to approximate a plasma convection model by a computationally simpler model of reduced spatial dimension. A convection model with a pressure source centered at the inner boundary models the edge dynamics of a magnetically confined plasma. The time evolution of the energies of the pressure profile, the turbulent flow, and the zonal flow represent the dynamics of a solution. Perturbing the vorticity variable with a term proportional to the pressure curvature causes the generation of an additional zonal flow, which qualitatively changes the solution. Rayleigh decomposition splits the variables of the model into averaged variables and fluctuation variables. The fluctuation variables are approximated by truncated Fourier series, and the equations are projected onto the Fourier basis functions. This results in a computationally simpler model with the spatial dimension reduced by one. Bifurcation diagrams reveal consistency between the bifurcation structures of the full model and the reduced model.

3.1 Introduction

The dynamics near the edge of a magnetically confined plasma is largely governed by convection-diffusion effects. A convection model, with governing equations for a thermodynamic variable and the vorticity, constitutes a simple model for interchange motions in the edge region. The pressure gradient drives the interchange motions in the plasma similarly to the way gravity drives Rayleigh–Bénard convection in fluids. The plasma flow can be decomposed into a non-zonal (turbulent, fluctuating) flow and a zonal flow. The non-zonal flow increases the radial transport and generates Reynolds stress that drives the zonal flow.

The L–H transition is a transition from a low confinement mode to a high confinement mode of a magnetically confined plasma. The 3-ODE Kim-Diamond L–H transition model [46, 47] and the 1D L–H transition model by Miki et al. [59, 60] include, in addition to the zonal flow, a pressure-gradient driven mean flow, which suppresses the turbulence and the growth rate of the zonal flow.

The HESEL model [44] is a 2D four-field drift fluid model. Solutions to the HESEL model reveal L–H-like transitions in response to ramping up the input power. A generalized vorticity replaces the vorticity in the HESEL model. This causes the curvature of the ion pressure to generate an additional zonal flow. This additional zonal flow can be thought of as the mean flow included in the low-dimensional L–H transition models. Hence, the generalized vorticity might be main responsible for allowing the observed transition.

Plasma models can be computationally demanding to solve. Capturing the physics with a model of reduced dimension simplifies the model analysis, and might enable the connection of specific terms to specific effects observed in the simulations.

In this chapter, we model the edge dynamics of a magnetically confined plasma with a convection model with a pressure source centered at the inner boundary. We introduce a perturbation to the vorticity, which is proportional to the pressure curvature, and investigate the solution dependency on the strength of this perturbation. We apply a Galerkin method to approximate the 2D convection model by a computationally simpler 1D convection model. The time evolution of the energies of the pressure profile P, the turbulent flow N, and the zonal flow F represent the dynamics of the solutions. Bifurcation diagrams, with the source strength as bifurcation parameter, reveal consistency between the bifurcation structures of the full model and the reduced model.

3.2 Galerkin method

To reduce the spatial dimension of a set of governing equations, we use a Reynolds decomposition of the state variables, followed by a Fourier series approximation of the fluctuation variables. We make a Galerkin projection of the resulting set of equations onto the Fourier basis functions. Benkadda et al. [9] and Bian et al. [12] use a similar approach to reduce a 2D interchange instability model to a 1D model for bursty transport.

3.2.1 The Reynolds decomposition principle

Reynolds decomposition is the decomposition of a variable $f(\boldsymbol{x}, t)$ into a mean part $\bar{f}$ and a fluctuating part $\tilde{f}$,

$$f = \bar{f} + \tilde{f}.$$

The mean $\bar{f}$ can be defined in different ways. The ensemble-average assumes f is a random variable, and defines the mean as the expectation value $\bar{f} = E[f(\boldsymbol{x}, t)]$. The ensemble-average of f can be computed from repeated measurements of $f(\boldsymbol{x}, t)$. The mean $\bar{f}$ can also be defined as a convolution between an appropriate filter function $H(\boldsymbol{x}, t)$ and f, $\bar{f} = (H * f)(\boldsymbol{x}, t)$. These definitions of $\bar{f}$ cause both $\bar{f}$ and $\tilde{f}$ to depend on the same independent variables as f depends on [63].

For a function $f : [0, L_x] \times [0, L_y] \times \mathbb{R} \mapsto \mathbb{R}$, we here define the mean $\bar{f}$ as the average of f taken over the y-variable

$$\bar{f}(x, t) = \frac{1}{L_y} \int_0^{L_y} f(x, y, t) dy.$$

With this definition, the mean part $\bar{f}$ depends on only (x, t), while the fluctuating part $\tilde{f} = f - \bar{f}$ depends on (x, y, t).

3.2.2 Fourier-series approximation of PDEs

After a Reynolds decomposition of the state variables, we approximate the (2+1)-dimensional partial differential equations (PDEs) for the fluctuation variables with truncated Fourier series and derive a (1+1)-dimensional PDE for each Fourier coefficient. We here outline the principle.

Let $L^2(0, L_y)$ be a Hilbert space equipped with the inner product

$$\langle f, g\rangle = \int_0^{L_y} f(y)g^*(y)dy, \qquad f, g \in L^2(0, L_y).$$

For each $x \in [0, L_x]$ and $t > 0$, assume $f(x, y, t) \in L^2(0, L_y)$ is a state variable, which is L_y-periodic in y. Let $\mathcal{D}$ be a nonlinear differential operator, which differentiates with respect to (x, y). Consider the PDE problem

$$\partial_t f = \mathcal{D}(f), \tag{3.1a}$$
$$f(x, y, 0) = 0, \tag{3.1b}$$
$$f(0, y, t) = f(L_x, y, t) = 0, \tag{3.1c}$$
$$f(x, 0, t) = f(x, L_y, t). \tag{3.1d}$$

Since the state variable f is periodic in the y-variable, but not in the x-variable, we approximate $f(x, y, t)$ by the Nth partial sum of its Fourier series expansion in the y-variable

$$f(x, y, t) \approx \sum_{n=-N}^{N} f_n(x, t)e^{inay}, \quad a = \frac{2\pi}{L_y}. \tag{3.2}$$

The Fourier coefficients f_n are given by

$$f_n(x, t) = \frac{1}{L_y}\langle f, e^{inay}\rangle = \frac{1}{L_y}\int_0^{L_y} f(x, y, t)e^{-inay}dy, \qquad f_{-n} = f_n^*.$$

The approximation (3.2) is inserted into the PDE (3.1a). For each $k \in \{-N, \dots N\}$, an equation for the Fourier coefficient f_k is obtained by projecting the differential equation onto the corresponding Fourier basis function e^{ikay}. The projection takes the inner product of the equation with e^{ikay}, which is equivalent to Fourier transforming the equation,

$$L_y\partial_t f_k(x, t) = \left\langle \mathcal{D}\left(\sum_{n=-N}^{N} f_n e^{inay}\right), e^{ikay}\right\rangle, \qquad k = -N, \dots, N. \tag{3.3}$$

The right-hand-side of Eq. (3.3) is calculated term-wise. For instance, the projection of f onto e^{ikay} is simply $\langle f, e^{ikay}\rangle = L_y f_k$, and the projection of $\partial_y f$ onto e^{ikay} is $\langle \partial_y f, e^{ikay}\rangle = ikaL_y f_k$.

If $\mathcal{D}(f)$ includes only linear terms, this procedure simply results in a set of uncoupled PDEs for f_k, $k = -N, \dots, N$, where each equation can be solved independently. If $\mathcal{D}(f)$ includes nonlinear terms, say f^2, the equations couple. System (3.3) can be solved numerically for the Fourier coefficients, and the approximated solution to the original problem (3.1) is then calculated by inserting the Fourier coefficients into Eq. (3.2).

3.3 Simulation data generation

A convection model is used as a simple model for convectively driven transport in a magnetized plasma. A pressure source at the inner boundary of the slab geometry describes plasma radially diffusing from the center into the computational domain. The source strength is considered the main bifurcation parameter of this problem. We define as state variables the potential energy related to the pressure, the kinetic energy of the turbulent flow, and the kinetic energy of the zonal flow. During the numerical solving process these three energies and their time-derivatives are computed and saved at each output time step.

3.3.1 Convection model

We consider viscous plasma flow in a small rectangular domain at the edge of a magnetically confined plasma in the plane perpendicular to the magnetic field $\boldsymbol{B} = B_0 \boldsymbol{e}_z$. The transport of plasma into the domain is modeled by a source centered at the left boundary. The flow is described using Cartesian coordinates $(x, y) \in [0, L_x] \times [0, L_y]$. The $\boldsymbol{E} \times \boldsymbol{B}$ drift velocity is given by

$$\boldsymbol{v}_E = \frac{\boldsymbol{E} \times \boldsymbol{B}}{B_0^2},$$

where $B_0 = \|\boldsymbol{B}\|$. We make the electrostatic approximation $\nabla \times \boldsymbol{E} = \partial_t \boldsymbol{B} = 0$, such that $\boldsymbol{E} = -\nabla\phi$. We define the normalized velocity field $\boldsymbol{v} = (v_x, v_y)^\intercal$ as

$$\boldsymbol{v} = B_0 \boldsymbol{v}_{E\perp} = (\boldsymbol{e}_z \times \nabla\phi)_\perp = \begin{pmatrix} -\partial_y \phi \\ \partial_x \phi \end{pmatrix}. \tag{3.4a}$$

Let Ω denote the z-component of the normalized vorticity vector $\boldsymbol{\Omega} = \nabla \times B_0 \boldsymbol{v}_E = (\partial_x v_y - \partial_y v_x)\boldsymbol{e}_z$. We introduce a perturbed scalar vorticity by $\omega = \Omega + \tau \nabla_\perp^2 p$, where τ is a coefficient of the perturbation. The introduction of this perturbation is inspired by the definition of the generalized vorticity in the HESEL model [44], with the aim to investigate how such a term affects solutions with everything else unchanged. Then, the normalized electrostatic potential is obtained from

$$\nabla_\perp^2 \phi = \omega - \tau \nabla_\perp^2 p. \tag{3.4b}$$

To describe the evolution of the pressure $p(x, y, t)$ and the perturbed vorticity $\omega(x, y, t)$, we employ a normalized convection model

$$\left(\frac{\partial}{\partial t} + \boldsymbol{v} \cdot \nabla \right) p = \kappa \nabla_\perp^2 p + S(x), \tag{3.4c}$$

$$\left(\frac{\partial}{\partial t} + \boldsymbol{v} \cdot \nabla \right) \omega + \frac{\partial p}{\partial y} = \nu \nabla_\perp^2 w. \tag{3.4d}$$

Here, κ is the diffusion coefficient, ν is the viscosity, and $S(x)$ is a pressure source. We choose the source as a Gaussian function of x centered at the left boundary,

$$S(x) = q\mathrm{e}^{-\frac{x^2}{2\sigma^2}}. \tag{3.4e}$$

The parameter q determines the strength of the source and σ determines the width of the source. At the $y = 0$ and $y = L_y$ boundaries, we apply periodic boundary conditions:

$$f(x,0,t) = f(x,L_y,t), \qquad \partial_y f(x,0,t) = \partial_y f(x,L_y,t), \qquad f = p,\omega,\phi. \tag{3.5a}$$

For the pressure, we apply a Neumann boundary condition at the left boundary, and a zero Dirichlet boundary condition at the right boundary,

$$\partial_x p(0,y,t) = 0, \qquad p(L_x,y,t) = 0. \tag{3.5b}$$

These boundary conditions allow the pressure gradient to increase as the source strength, q, increases. For the electrostatic potential and perturbed vorticity, we apply zero Dirichlet boundary conditions at both the left and right boundaries,

$$\omega(0,y,t) = \omega(L_x,y,t) = 0, \qquad \phi(0,y,t) = \phi(L_x,y,t) = 0. \tag{3.5c}$$

As initial condition, each of the system variables is set to zero at $t = 0$,

$$p(x,y,0) = \omega(x,y,0) = \phi(x,y,0) = 0. \tag{3.6}$$

These choices of computational domain, pressure source, and boundary conditions are visually summarized in Fig. 3.1.

For $\tau = 0$, system (3.4) is one of the simplest models used to describe nonlinear plasma dynamics. Bian et al. [12] and Garcia et al. [31] model the resistive g-instability in a plasma fluid layer with a system similar to Eq. (3.4) with $\tau = 0$. References [10, 30, 33] model the interchange motions of isolated structures in magnetized plasmas with a system equivalent to Eq. (3.4) with $\tau = 0$. In the field of fluid dynamics the system is often used to model Rayleigh-Bénard convection [37]. More accurate models for nonlinear plasma dynamics like the ESEL model [32, 34] can be regarded as extensions to the $\tau = 0$ convection model (3.4) by including additional terms and couple more fields to describe more nonlinear effects.

For $\tau > 0$, system (3.4) includes a perturbed vorticity that imitates the generalized vorticity in the HESEL model [44]. The generalized vorticity is thought to be a main component responsible for the L–H-like transition, that can be observed in HESEL simulations. This motivates the investigation of this perturbation to the vorticity in a simple convection model.

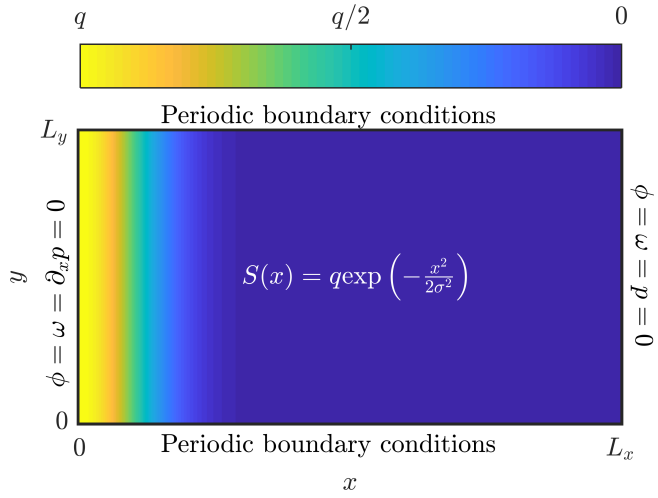

Figure 3.1. The pressure source $S(x)$ given by Eq. (3.4e) with $\sigma = 0.1L_x$ shown inside the domain. The boundary conditions (3.5) for the problem are shown at each boundary.

3.3.2 State variable definitions

Predator-prey models for the L–H transition are often based on three state variables; the potential energy related to the pressure profile, the turbulent flow energy, and the zonal flow energy. To formally define these variables in terms of the state variables of the PDE system (3.4), we first introduce some useful notation: An overline denotes average over the y-variable, a tilde denotes the spatial fluctuations, and angle brackets denote average over the x-variable

$$\begin{aligned}
\bar{f}(x,t) &= \frac{1}{L_y}\int_0^{L_y} f(x,y,t)\,dy,\\
\tilde{f}(x,y,t) &= f(x,y,t) - \bar{f}(x,t),\\
\langle\bar{f}\rangle(t) &= \frac{1}{L_x}\int_0^{L_x} \bar{f}(x,t)\,dx.
\end{aligned}$$

To consistently define the state variables, we consider Eq. (3.4) with unchanged boundary conditions in the limit of no source, no viscosity, no diffusivity, and no perturbation of the vorticity, i.e. with $\kappa = \nu = S = \tau = 0$. Then we obtain the

system

$$\Omega = \nabla^2 \phi, \tag{3.7a}$$

$$\partial_t p = -\boldsymbol{v} \cdot \nabla p, \tag{3.7b}$$

$$\partial_t \Omega = -\boldsymbol{v} \cdot \nabla \Omega + \frac{\partial p}{\partial y}. \tag{3.7c}$$

Averaging Eq. (3.7b) over y and x, followed by integration by parts with the boundary conditions (3.5), gives

$$\partial_t \langle \bar{p} \rangle = -\langle \overline{v_x (\partial_x p)} \rangle - \langle \overline{v_y (\partial_y p)} \rangle = \langle \overline{(\partial_x v_x + \partial_y v_y) p} \rangle = 0.$$

Since the average of p is constant in time, even when the pressure drives a flow, it can not be used as a measure for the potential energy of the system. If we instead consider Eq. (3.7b), multiply by x, and then average over y and x, we obtain

$$\partial_t \langle \overline{xp} \rangle = \langle \overline{v_x p} \rangle. \tag{3.8}$$

The spatially averaged kinetic energy of the flow is given by $K = \frac{1}{2} \langle \overline{\boldsymbol{v} \cdot \boldsymbol{v}} \rangle$. Considering Eq. (3.7c), multiplying by ϕ, and using integration by parts, it can be shown that

$$\frac{1}{2} \partial_t \langle \overline{\boldsymbol{v} \cdot \boldsymbol{v}} \rangle = -\langle \overline{\phi (\partial_t \Omega)} \rangle = -\langle \overline{v_x p} \rangle. \tag{3.9}$$

Adding Eqs. (3.8) and (3.9) gives the conservation equation

$$\partial_t \left(\frac{1}{2} \langle \overline{\boldsymbol{v} \cdot \boldsymbol{v}} \rangle + \langle \overline{xp} \rangle \right) = 0. \tag{3.10}$$

Since the first term in Eq. (3.10) is the time derivative of the kinetic energy, we define the second term to be the time derivative of the potential energy. We now separate the kinetic energy into the zonal flow energy and the fluctuation energy. Inserting the decomposition $v_x = \bar{v}_x + \tilde{v}_x$, with $\bar{v}_x = 0$ and $v_y = \bar{v}_y + \tilde{v}_y$, into the expression $\boldsymbol{v} \cdot \boldsymbol{v}$ and averaging over y and x gives

$$\frac{1}{2} \langle \overline{\boldsymbol{v} \cdot \boldsymbol{v}} \rangle = \frac{1}{2} \langle \overline{\tilde{v}_x^2} + \overline{\tilde{v}_y^2} \rangle + \frac{1}{2} \langle \bar{v}_y^2 \rangle. \tag{3.11}$$

The first term on the right-hand side is the kinetic energy related to the fluctuations, while the second term is the kinetic energy related to the zonal flow.

We can now define the average potential energy P, related to the pressure profile, the average fluctuation energy N, and the zonal flow energy F, by

$$P = \langle \overline{xp} \rangle, \qquad N = \frac{1}{2} \langle \overline{\tilde{v}_x^2} + \overline{\tilde{v}_y^2} \rangle, \qquad F = \frac{1}{2} \langle \bar{v}_y^2 \rangle. \tag{3.12}$$

Sugama and Horton [68], and Ball, Dewar, and Sugama [8] define state variables for their L–H transition models which are equivalent to the definitions in Eq. (3.12).

L_x	L_y	κ	ν	σ
1	1	0.05	0.05	0.1

Table 3.1. The fixed parameter values for the system (3.4). $q \in [0, 10]$ is a bifurcation parameter.

3.3.3 Parameters and numerical solver

The convection problem (3.4) contains six parameters: L_x and L_y determines the size and aspect ratio of the rectangular domain, κ is the diffusion coefficient, ν is the viscosity, σ determines the width of the pressure source, and q determines the strength of the pressure source. The value of each of these parameters affect the solution and could be chosen as the main parameter for the analysis.

We fix all parameter values except q, which we consider as a bifurcation parameter. The values of the fixed parameters in Eq. (3.4) are listed in Table 3.1. The values of κ and ν were chosen sufficiently large that equilibrium solutions existed for small values of q and a period-1 solution could be observed for a range of q-values. The bifurcation parameter q is fixed for each simulation, but we consider multiple simulation data sets obtained for different values of $q \in [0, 10]$.

The FEM software package COMSOL Multiphysics® is used as the numerical solver [20]. The PDE system (3.4) and the corresponding boundary conditions are defined on the rectangular domain $[0, L_x] \times [0, L_y]$. To obtain the required simulation data we use a triangular mesh containing 6282 domain elements. The triangular mesh size was set with the command:

```
model.mesh('mesh1').feature('size').set('table', '
    plasma');
model.mesh('mesh1').feature('size').set('hauto', '5');
```

The generated mesh is shown in Fig. 3.2. The solution is initialized at $t = 0$ and run with output time steps of $\Delta t = 0.05$ until $t = 400$. At each output time of the simulation the three energies (3.12) and their time-derivatives are computed and saved. We set the relative error tolerance by

```
model.study('std1').feature('time').set('rtolactive',
    'on');
model.study('std1').feature('time').set('rtol', '1e-6'
    );
```

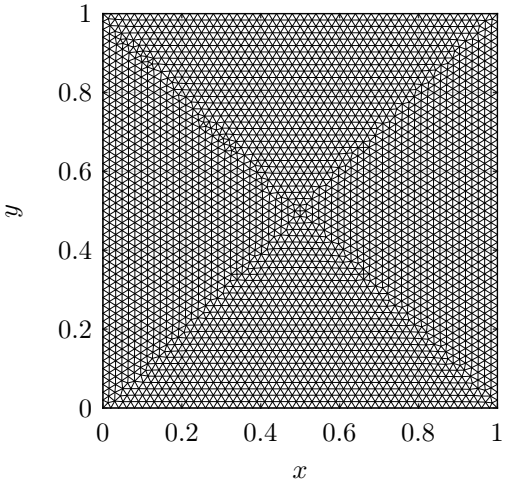

Figure 3.2. The used triangular mesh contained 6282 domain elements and 200 boundary elements.

3.3.4 Solution examples

The source strength q is the bifurcation parameter for the system (3.4), and as q varies, the solution moves through different modes. To investigate the additional dependency on τ, we increase q linearly in time from zero to 30, by defining $q(t) = 30t/400$, and plot the energies (P, N, F) as functions of time, for different values of τ.

Figures 3.3–3.6 show the solutions for $\tau = 0.00$, $\tau = 0.02$, $\tau = 0.04$, and $\tau = 0.06$, respectively. The perturbation with τ as coefficient generates an additional zonal flow, which suppresses the turbulence. Increasing τ from zero to 0.06 heavily changes the solution type. For $\tau = 0.04$ the turbulence grows up, enters an oscillating phase, and converges to zero. A similar behavior can be observed in the minimal L–H transition suggested by Kim and Diamond [46, 47]. Their model includes, in addition to the zonal flow, a mean flow. In our solutions, the mean flow is included in the zonal flow. The $\tau = 0.04$ solution suggests that a generalized vorticity could be the source of this so-called mean flow, which enables the L–H transition. For $\tau = 0.06$ the zonal flow is so strong that it prevents the turbulence to grow at all. We shall work further with the $\tau = 0$ and $\tau = 0.04$ solutions.

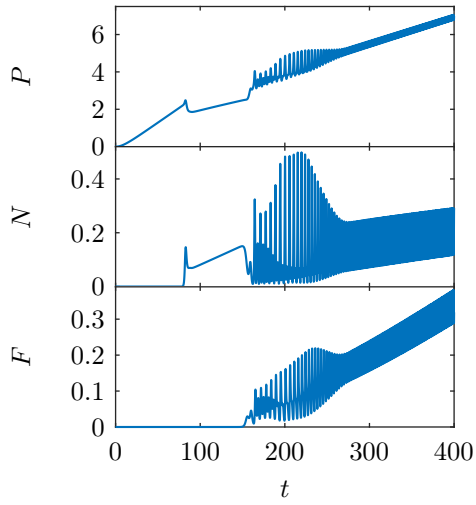

Figure 3.3. For $\tau = 0.00$ and $q(t) = 30t/400$, the time evolution of the energies P, N, and F.

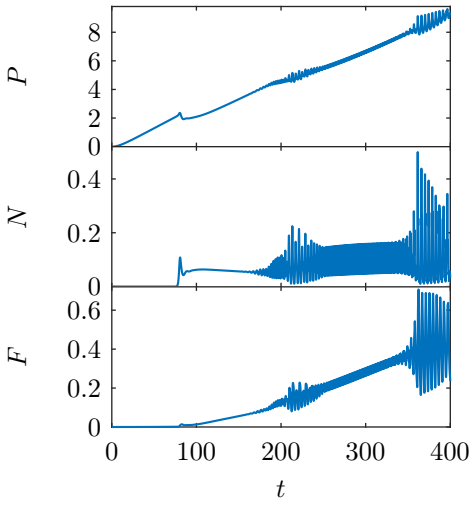

Figure 3.4. For $\tau = 0.02$ and $q(t) = 30t/400$, the time evolution of the energies P, N, and F.

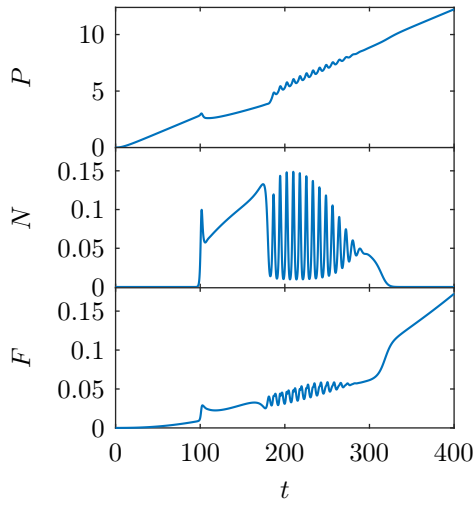

Figure 3.5. For $\tau = 0.04$ and $q(t) = 30t/400$, the time evolution of the energies P, N, and F.

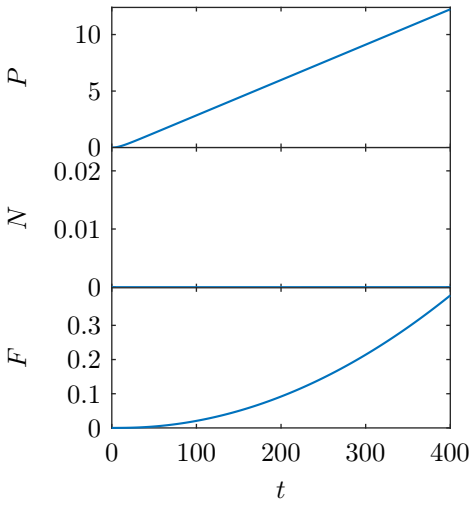

Figure 3.6. For $\tau = 0.06$ and $q(t) = 30t/400$, the time evolution of the energies P, N, and F.

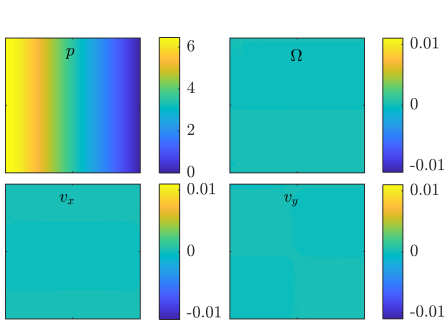

Figure 3.7. For $\tau = 0$, the $q = 2.8$ static solution at $t = 200$ showing p (upper left), Ω (upper right), v_x (lower left), and v_y (lower right).

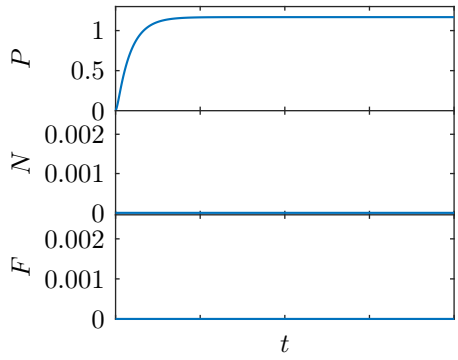

Figure 3.8. For $\tau = 0$, the $q = 2.8$ time evolution of the energies P, N, and F. P converges to a constant value while $N = F = 0$ for all t.

3.3.5 Solution parameter dependency

For $\tau = 0$, simulation data were obtained for multiple values of $q \in [0, 10]$, and for $\tau = 0.04$, simulation data were obtained for $q \in [0, 24]$. As q varies, we observe four qualitatively different types of solutions. In the (P, N, F)-state space, each solution type is characterized by the stability type of the observed equilibrium points. We pair each of the four distinct solution types observed in the (P, N, F)-state space with the corresponding full solutions of the convection problem, represented by the variables p, ω ($\omega = \Omega$ when $\tau = 0$), v_x, and v_y.

3.3.5.1 The static solution

For $\tau = 0$ and $q = 2.8$, the solution to Eqs. (3.4)–(3.6) converges to the static solution shown in Fig. 3.7. Here, the pressure is independent of the y-coordinate, and there is no vorticity and therefore no flow. For the time evolution of the energies P, N, and F, shown in Fig. 3.8, P converges to a positive constant value, while $N = F = 0$ for all time. We denote the equilibrium (P_s, N_s, F_s) corresponding to this static state the s-equilibrium.

For $\tau = 0.04$ and $q = 2.8$, the solution converges to the static solution shown in Fig. 3.9. Here, all variables are independent of the y-coordinate, and $\omega = 0$. There is a poloidal flow induced by the pressure curvature, v_y, but with a static profile. The time evolution of the energies P, N, and F is shown in Fig. 3.10. P and F converge to positive constant values, while $N = 0$ for all time.

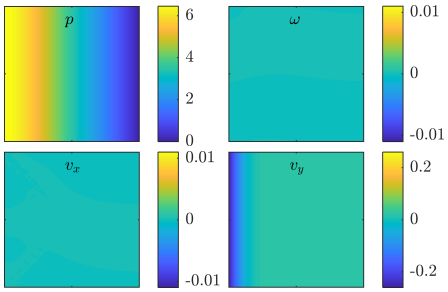

Figure 3.9. For $\tau = 0.04$, the $q = 2.8$ static solution at $t = 200$ showing p (upper left), ω (upper right), v_x (lower left), and v_y (lower right).

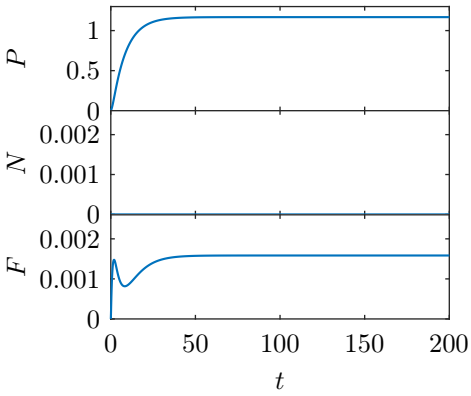

Figure 3.10. For $\tau = 0.04$, the $q = 2.8$ time evolution of the energies P, N, and F. P and F converge to constant values while $N = 0$ for all t.

3.3.5.2 The low confinement solution

For $\tau = 0$ and $q = 6$, the solution converges to the stable solution shown in Fig. 3.11. For this equilibrium solution, p and v_x are symmetric, while Ω and v_y are antisymmetric through a line at $y = 1/2$. The time evolution of the energies P, N, and F is shown in Fig. 3.12. The solution contains two phases: The first phase is similar to the solution for $q = 2$, where $N = F = 0$, while P approaches an equilibrium value. However, this equilibrium solution is unstable and, during the second phase, N first increases rapidly and then decreases toward an equilibrium value. This causes P to make a little bump on the curve and then decreases toward a lower stable equilibrium value. Since v_x and v_y are nonzero almost everywhere, there is a non-zonal flow, $N > 0$, while the symmetry of v_x and the antisymmetry of v_y cause the vanishing zonal flow, $F = 0$. The potential energy of the pressure, P, is a measure of the level of plasma confinement. Since this state results in the lowest confinement level of the four states, we denote this state the low confinement state and the corresponding equilibrium point (P_L, N_L, F_L) is denoted the L-equilibrium.

For $\tau = 0.04$ and $q = 8$, the solution converges to the pattern shown in Fig. 3.13. Here, p, ω, v_x, and v_y drift downward. The time evolution of the energies P, N, and F is shown in Fig. 3.14. The solution contains two phases: The first phase is similar to the static solution, but the s-equilibrium is unstable, and N first increases rapidly and then decreases toward an equilibrium value. This cause P and F to make small bumps and decrease toward the L-equilibrium, where P is smaller and F is larger than in the s-equilibrium.

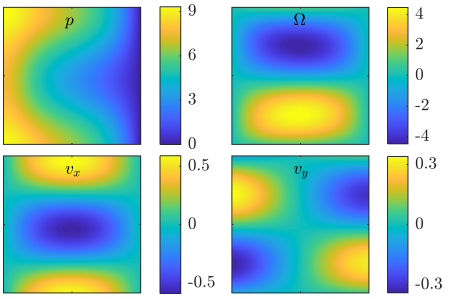

Figure 3.11. For $\tau = 0$, the $q = 6.0$ low confinement solution at $t = 200$ showing p (upper left), Ω (upper right), v_x (lower left), and v_y (lower right). The patterns are constant in time.

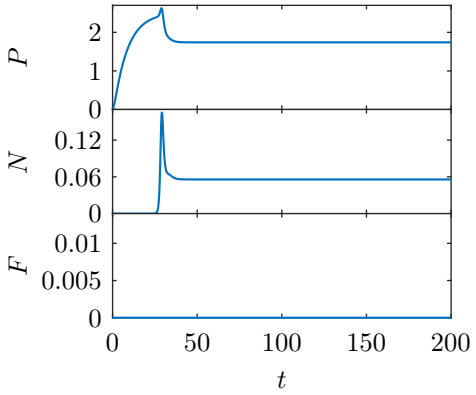

Figure 3.12. For $\tau = 0$, the $q = 6$ time evolution of the energies P, N, and F. P and N converge to constant values while $F = 0$ for all t. This is the low confinement solution.

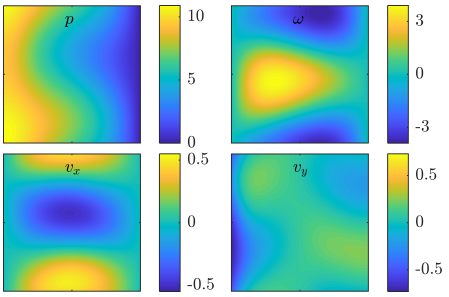

Figure 3.13. For $\tau = 0.04$, the $q = 6.0$ low confinement solution at $t = 200$ showing p (upper left), ω (upper right), v_x (lower left), and v_y (lower right). The patterns drift downward for increasing time.

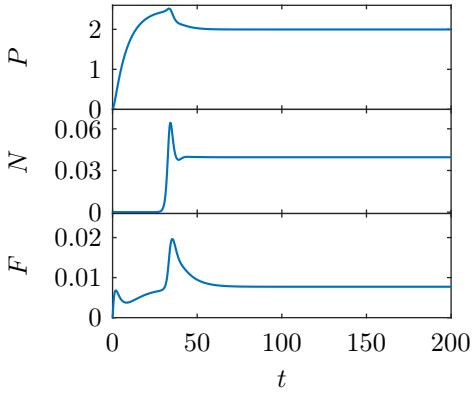

Figure 3.14. For $\tau = 0.04$, the $q = 6$ time evolution of the energies P, N, and F. P, N, and F converge to constant values. This is the low confinement solution.

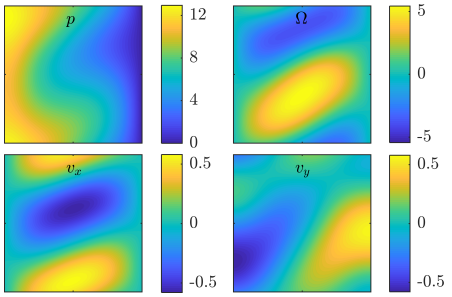

Figure 3.15. For $\tau = 0$, the $q = 8.0$ high confinement solution at $t = 200$ showing p (upper left), Ω (upper right), v_x (lower left), and v_y (lower right). The patterns are in motion and are drifting downwards for increasing time.

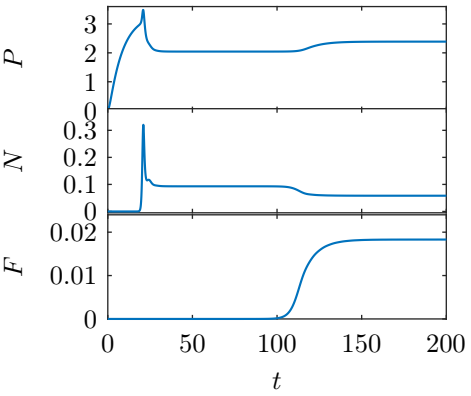

Figure 3.16. For $\tau = 0$, the $q = 8.0$ time evolution of the energies P, N, and F. The solution converges to the H-equilibrium, where all three energies are positive.

3.3.5.3 The high confinement solution

For $\tau = 0$ and $q = 8$, the solution converges to the down-drifting patterns shown in Fig. 3.15. The symmetry of the patterns that exist for $q = 6$ is now broken. The time evolution of the energies P, N, and F is shown in Fig. 3.16. The solution now consist of three phases: The first two phases are similar to the solution phases for $q = 6$ shown in Fig. 3.12. In the third phase, F increases and approaches an equilibrium value. This causes P to converge to a larger equilibrium value and N to converge to a smaller equilibrium value. Compared to the $q = 6$ solution in Fig. 3.15, breaking of the symmetry of v_x and v_y causes the zonal flow, $F > 0$. Since this state results in a higher confinement than before, we denote this state the high confinement state. The corresponding equilibrium point (P_H, N_H, F_H) is denoted the H-equilibrium.

For $\tau = 0.04$ and $q = 20$, the solution converges to the down-drifting patterns shown in Fig. 3.17. The time evolution of the energies P, N, and F is shown in Fig. 3.18. Similarly to the low confinement solution, the solution consist of two phases, but the equilibrium values of N and F are lower and P is higher than in the L-equilibrium.

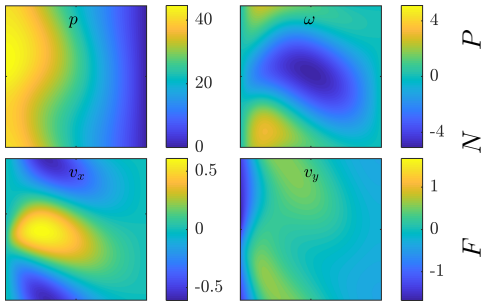

Figure 3.17. For $\tau = 0.04$, the $q = 20.0$ high confinement solution at $t = 200$ showing p (upper left), ω (upper right), v_x (lower left), and v_y (lower right). The patterns are in motion and are drifting downward for increasing time.

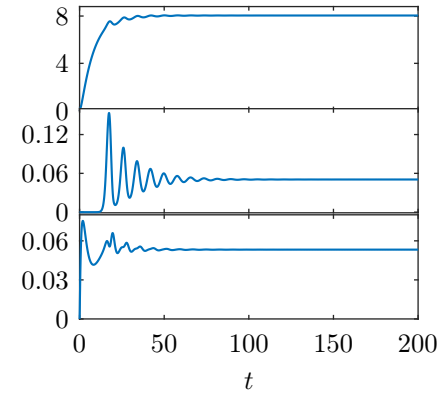

Figure 3.18. For $\tau = 0.04$, the $q = 20$ time evolution of the energies P, N, and F. The solution converges to the H-equilibrium, where all three energies are positive.

3.3.5.4 The limit cycle solution

For $\tau = 0$ and $q = 10$, the solution converges to the oscillating patterns shown in Fig. 3.19. The pressure p is oscillating between two clearly different patterns, while the patterns for Ω, v_x, and v_y are mostly oscillating in terms of amplitude. The time evolution of the energies is shown in Fig. 3.20. The solution still consists of three phases similarly to the low confinement solution for $q = 8$. However, the third phase is now replaced by convergence to a stable limit cycle, where the three energies oscillate at identical frequencies. We denote this solution type the limit cycle solution.

For $\tau = 0.04$ and $q = 16$, the solution converges to the oscillating patterns shown for $t = 200$ in Fig. 3.21. For this limit cycle solution, p is oscillating between two clearly different patterns, while the patterns for ω, v_x, and v_y are mostly oscillating in terms of amplitude. The time evolution of the energies is shown in Fig. 3.22. The solution consist of two phases: the first phase is similar to the s-state, but as N begins to increase the solution converges to a stable oscillating phase.

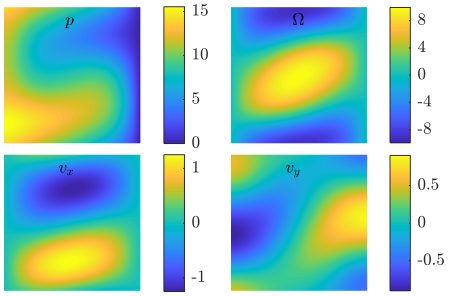

Figure 3.19. For $\tau = 0$, the $q = 10.0$ limit cycle solution at $t = 196$ showing p (upper left), Ω (upper right), v_x (lower left), and v_y (lower right). p is oscillating between two different patterns, while Ω, v_x, and v_y are mostly oscillating in amplitude.

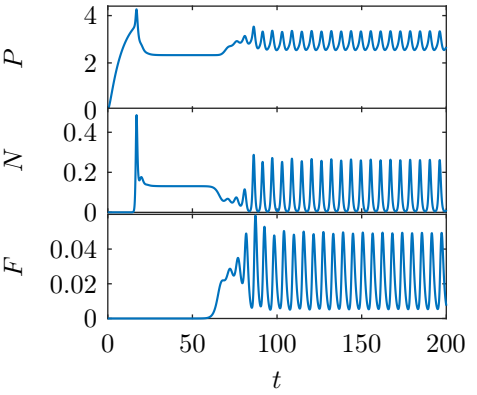

Figure 3.20. For $\tau = 0$, the $q = 10$ time evolution of the energies P, N, and F. The solution converges to stable limit cycle oscillations of P, N, and F. This is the limit cycle solution.

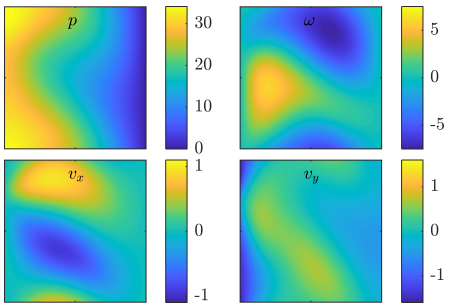

Figure 3.21. For $\tau = 0.04$, the $q = 16.0$ limit cycle solution at $t = 200$ showing p (upper left), ω (upper right), v_x (lower left), and v_y (lower right). p is oscillating between two different patterns, while ω, v_x, and v_y are mostly oscillating in amplitude.

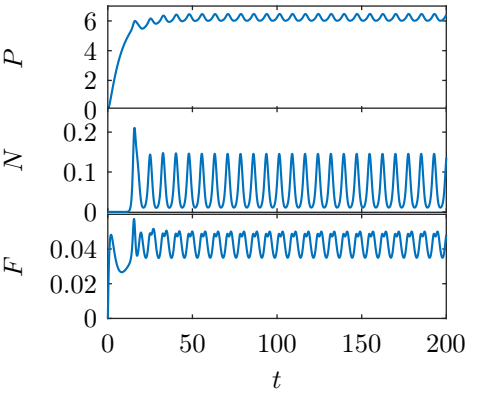

Figure 3.22. For $\tau = 0.04$, the $q = 16$ time evolution of the energies P, N, and F. The solution converges to stable limit cycle oscillations of P, N, and F. This is the limit cycle solution.

3.3.6 Data-based bifurcation diagrams

For $\tau = 0$, simulation data for P, N, and F was generated for $q \in \{0, 0.1, \ldots, 10\}$. For $q > 10$ more bifurcations occur, with the first one being a period doubling bifurcation. The data-based bifurcation diagram shown in Fig. 3.23 is constructed by approximately identifying the location of all equilibrium points for each solution. The unstable s-equilibrium is computed from a modified model with $\boldsymbol{v} = 0$, the unstable L-equilibrium is estimated from the transient part of the solution, and the unstable H-equilibrium is extrapolated from the stable part of the H-equilibrium. Transcritical bifurcations occur at approximately $q_{\mathrm{tc1}} \approx 2.92$ and $q_{\mathrm{tc2}} \approx 6.28$, while a Hopf bifurcation occurs at $q_{\mathrm{H}} \approx 8.15$. The s-equilibrium is stable for $0 \leq q < q_{\mathrm{tc1}}$, the L-equilibrium is stable for $q_{\mathrm{tc1}} < q < q_{\mathrm{tc2}}$, the H-equilibrium is stable for $q_{\mathrm{tc2}} < q < q_{\mathrm{H}}$, and the limit cycle is stable for $q > q_{\mathrm{H}}$.

For $\tau = 0.04$, simulation data for P, N, and F was generated for $q \in \{0, 0.2, \ldots, 24\}$. The value of q was down-ramped to determine the stability of equilibria for the ranges of q with two stable solutions. The data-based bifurcation diagram shown in Fig. 3.24 is constructed by approximately identifying the location of all equilibrium points for each solution. The unstable s-equilibrium is computed from a modified model with $v_x = 0$, and the unstable H-equilibrium is intrapolated from the stable part of the H-equilibrium. Transcritical bifurcations occur at approximately $q_{\mathrm{tc1}} \approx 3.4$ and $q_{\mathrm{tc2}} \approx 20.4$, saddle-node bifurcations occurs at $q_{\mathrm{sn1}} \approx 8.8$, $q_{\mathrm{sn2}} \approx 12.3$, $q_{\mathrm{sn3}} \approx 22.1$, while Hopf-bifurcations occur at $q_{\mathrm{H1}} \approx 11.3$ and $q_{\mathrm{H2}} \approx 19.0$. The s-solution is stable for $0 \leq q < q_{\mathrm{tc1}}$ and again for $q > q_{\mathrm{tc2}}$, the L-solution is stable for $q_{\mathrm{tc1}} < q < q_{\mathrm{sn2}}$, the H-mode is stable for $q_{\mathrm{tsn1}} < q < q_{\mathrm{H1}}$ and again for $q_{\mathrm{H2}} < q < q_{\mathrm{sn3}}$, and the limit cycle is stable for $q_{\mathrm{H1}} < q < q_{\mathrm{H2}}$.

When a 1D reduced model has been identified we shall compare bifurcation diagrams for the reduced model with these bifurcation diagrams for the full model. The level of similarity between the diagrams will be used as one of the measures of how well the reduced model approximates the full model.

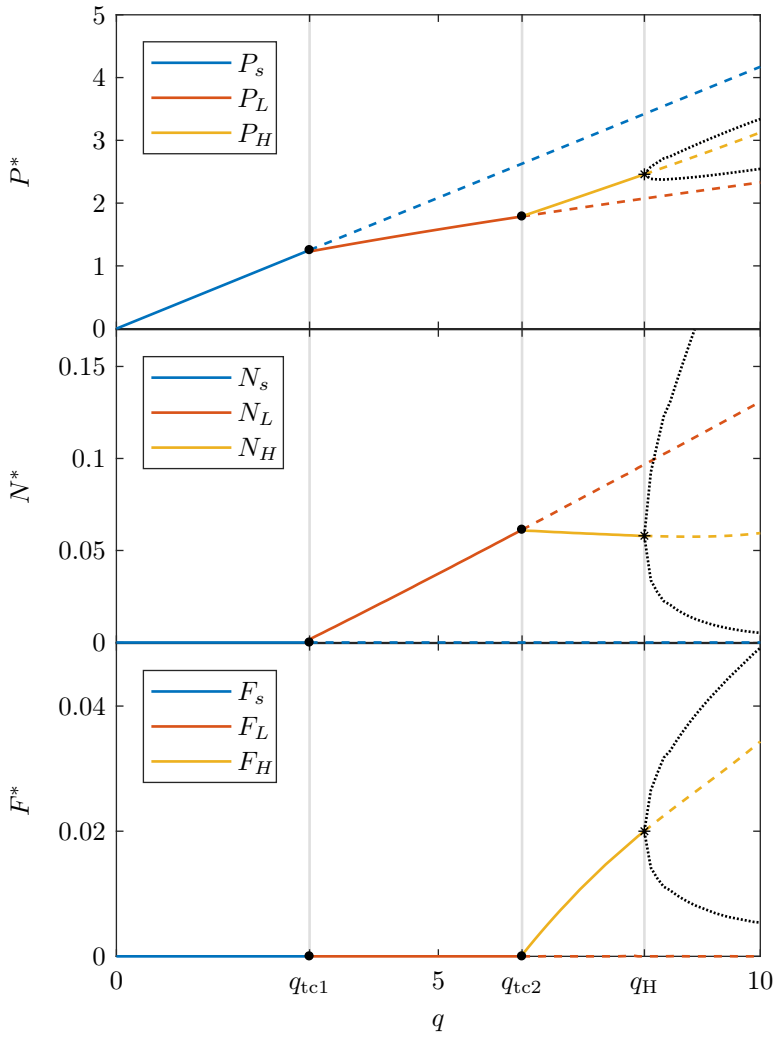

Figure 3.23. Bifurcation diagram generated from simulation data for $\tau = 0$. Solid curves are stable equilibrium points, dashed curves are unstable equilibrium points, while the dotted curves show the amplitude of the stable limit cycle. The transcritical bifurcations occurring at approximately $q_{\mathrm{tc1}} \approx 2.92$ and $q_{\mathrm{tc2}} \approx 6.28$ are marked with dots, while the Hopf bifurcation occurring at $q_{\mathrm{H}} \approx 8.15$ is marked with asterisks.

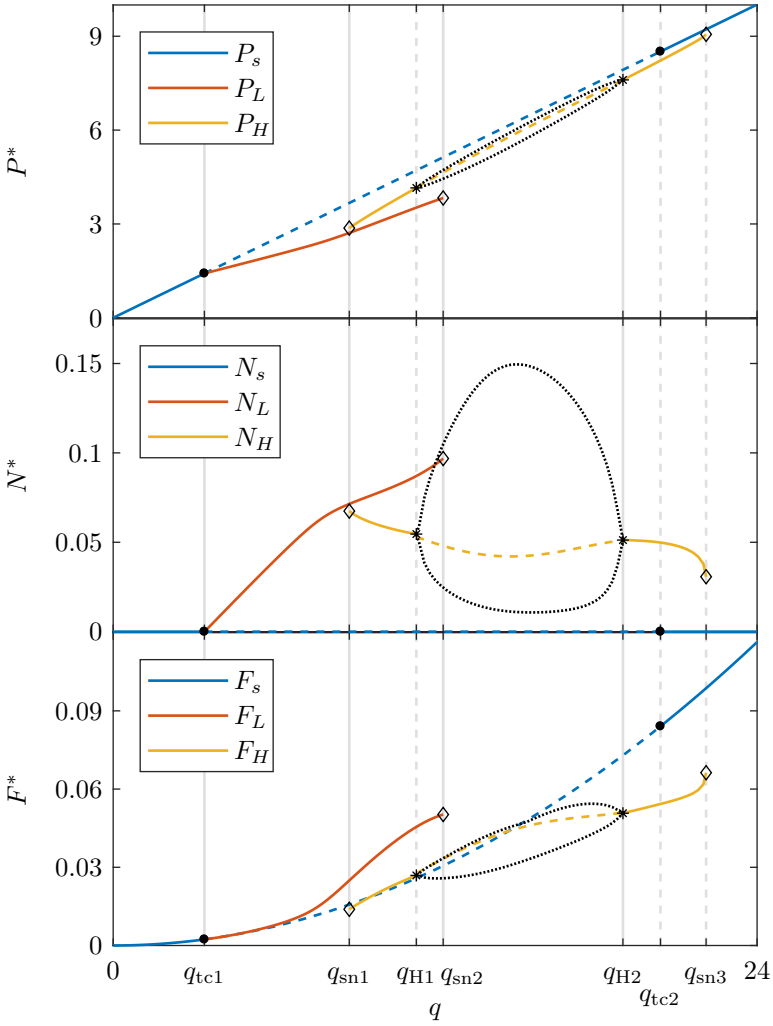

Figure 3.24. Bifurcation diagram generated from simulated data. Solid curves are stable equilibrium points, dashed curves are unstable equilibrium points, while the dotted curve show the amplitude of oscillations. The blue curve is the s-equilibrium, the red curve is the L-equilibrium, and the yellow curve is the H-equilibrium. The transcritical bifurcations occurring at approximately $q_{\mathrm{tc1}} \approx 3.4$ and $q_{\mathrm{tc2}} \approx 20.4$ are marked with dots, the saddle-node bifurcations occurring at $q_{\mathrm{sn1}} \approx 8.8$, $q_{\mathrm{sn2}} \approx 12.3$, $q_{\mathrm{sn3}} \approx 22.1$ are marked with diamonds, while the Hopf-bifurcations occurring at $q_{\mathrm{H1}} \approx 11.3$ and $q_{\mathrm{H2}} \approx 19.0$ are marked with asterisks.

3.4 Galerkin dimension reduction

For both $\tau = 0$ and $\tau = 0.04$, the solution patterns for p, ω, v_x, and v_y seem to be dominated by a single sinusoidal mode. We use a Galerkin method to approximate the y-dependence with sinusoidal wave functions and thereby reduce the space-dimension of the system (3.4) from two to one. The approach consists of two steps: a Reynolds decomposition followed by an Fourier series approximation and Galerkin projection onto the Fourier basis functions.

First, we rewrite Eq. (3.4) from vector form to a set of scalar equations. The equations for the fluid velocity (3.4a) and the electrostatic potential (3.4b) are

$$v_x = -\partial_y \phi, \tag{3.13a}$$

$$v_y = \partial_x \phi, \tag{3.13b}$$

$$\partial_{xx}^2 \phi + \partial_{yy}^2 \phi = \omega - \tau(\partial_{xx}^2 p + \partial_{yy}^2 p). \tag{3.13c}$$

We rewrite the convective term in Eq. (3.4c) for the evolution of p,

$$\begin{aligned}
\boldsymbol{v} \cdot \nabla p &= v_x \partial_x p + v_y \partial_y p \\
&= \partial_x \{p v_x\} + \partial_y \{p v_y\} - v_x \partial_x p - p \partial_x v_x - v_y \partial_y p - p \partial_y v_y + v_x \partial_x p + v_y \partial_y p \\
&= \partial_x \{p v_x\} + \partial_y \{p v_y\} - p(\partial_x v_x + \partial_y v_y) \\
&= \partial_x \{p v_x\} + \partial_y \{p v_y\}.
\end{aligned}$$

Similarly, the convective term in Eq. (3.4d) for the evolution of ω can be written

$$\boldsymbol{v} \cdot \nabla \omega = \partial_x \{\omega v_x\} + \partial_y \{\omega v_y\}.$$

Using this, Eqs. (3.4c)–(3.4d) for the evolution of p and ω can be written as

$$\partial_t p = -\partial_x \{p v_x\} - \partial_y \{p v_y\} + \kappa(\partial_{xx}^2 p + \partial_{yy}^2 p) + S(x), \tag{3.13d}$$

$$\partial_t \omega = -\partial_x \{\omega v_x\} - \partial_y \{\omega v_y\} - \partial_y p + \nu(\partial_{xx}^2 \omega + \partial_{yy}^2 \omega). \tag{3.13e}$$

We consider the system (3.13) with the boundary conditions (3.5).

3.4.1 Reynolds decomposition

Reynolds decomposition decompose a function into an average and a fluctuating part. The function can be averaged over time or space. Here, we average over the y-variable, which we denote with an overline, while a tilde denotes the fluctuations

$$\bar{f}(x,t) = \frac{1}{L_y} \int_0^{L_y} f(x,y,t)\, dy,$$

$$\tilde{f}(x,y,t) = f(x,y,t) - \bar{f}(x,t).$$

We note that $\overline{\tilde{f}} = 0$, $\overline{\partial_x f} = \partial_x \bar{f}$, $\overline{\bar{f}g} = \bar{f}\bar{g}$, and that the periodic boundary conditions (3.5a) cause $\overline{\partial_y f} = 0$. We decompose each of the variables v_x, v_y, ϕ, p, and ω into an average over y and a fluctuating part

$$f(x,y,t) = \bar{f}(x,t) + \tilde{f}(x,y,t), \qquad f = v_x, v_y, \phi, p, \omega. \tag{3.14}$$

Inserting the Reynolds decomposition (3.14) into Eqs. (3.13a)–(3.13c), and using $\partial_y \bar{f} = 0$ gives

$$\bar{v}_x + \tilde{v}_x = -\partial_y \tilde{\phi}, \tag{3.15a}$$

$$\bar{v}_y + \tilde{v}_y = \partial_x \bar{\phi} + \partial_x \tilde{\phi}, \tag{3.15b}$$

$$\partial^2_{xx}\bar{\phi} + \partial^2_{xx}\tilde{\phi} + \partial^2_{yy}\tilde{\phi} = \bar{\omega} + \tilde{\omega} - \tau(\partial^2_{xx}\bar{p} + \partial_{xx}\tilde{p} + \partial_{yy}\tilde{p}), \tag{3.15c}$$

$$\begin{aligned}\partial_t \bar{p} + \partial_t \tilde{p} = {} & -\partial_x\{\bar{p}\bar{v}_x + \tilde{p}\tilde{v}_x\} - \partial_y\{\bar{p}\tilde{v}_y + \bar{v}_y\tilde{p} + \tilde{p}\tilde{v}_y\} \\ & + \kappa(\partial^2_{xx}\bar{p} + \partial^2_{xx}\tilde{p} + \partial^2_{yy}\tilde{p}) + S,\end{aligned} \tag{3.15d}$$

$$\begin{aligned}\partial_t \bar{\omega} + \partial_t \tilde{\omega} = {} & -\partial_x\{\bar{\omega}\bar{v}_x + \tilde{\omega}\tilde{v}_x\} - \partial_y\{\bar{\omega}\tilde{v}_y + \bar{v}_y\tilde{\omega} + \tilde{\omega}\tilde{v}_y\} \\ & - \partial_y\tilde{p} + \nu(\partial^2_{xx}\bar{\omega} + \partial^2_{xx}\tilde{\omega} + \partial^2_{yy}\tilde{\omega}).\end{aligned} \tag{3.15e}$$

Averaging Eqs. (3.15) over y yields

$$\bar{v}_x = 0, \tag{3.16a}$$

$$\bar{v}_y = \partial_x \bar{\phi}, \tag{3.16b}$$

$$\partial^2_{xx}\bar{\phi} = \bar{\omega} - \tau\partial^2_{xx}\bar{p}, \tag{3.16c}$$

$$\partial_t \bar{p} = -\partial_x \overline{\tilde{p}\tilde{v}_x} + \kappa\partial^2_{xx}\bar{p} + S, \tag{3.16d}$$

$$\partial_t \bar{\omega} = -\partial_x \overline{\tilde{\omega}\tilde{v}_x} + \nu\partial^2_{xx}\bar{\omega}. \tag{3.16e}$$

Since $\tilde{f} = f - \bar{f}$, we obtain the equations for the fluctuations by subtracting the averaged equations (3.16) from the decomposed equations (3.15):

$$\tilde{v}_x = -\partial_y \tilde{\phi}, \tag{3.17a}$$

$$\tilde{v}_y = \partial_x \tilde{\phi}, \tag{3.17b}$$

$$\partial^2_{xx}\tilde{\phi} + \partial^2_{yy}\tilde{\phi} = \tilde{\omega} - \tau(\partial_{xx}\tilde{p} + \partial_{yy}\tilde{p}), \tag{3.17c}$$

$$\begin{aligned}\partial_t \tilde{p} = {} & -\partial_x\{\bar{p}\tilde{v}_x + \tilde{p}\bar{v}_x + \tilde{p}\tilde{v}_x - \overline{\tilde{p}\tilde{v}_x}\} - \partial_y\{\bar{p}\tilde{v}_y + \bar{v}_y\tilde{p} + \tilde{p}\tilde{v}_y\} \\ & + \kappa(\partial^2_{xx}\tilde{p} + \partial^2_{yy}\tilde{p}),\end{aligned} \tag{3.17d}$$

$$\begin{aligned}\partial_t \tilde{\omega} = {} & -\partial_x\{\bar{\omega}\tilde{v}_x + \tilde{\omega}\bar{v}_x + \tilde{\omega}\tilde{v}_x - \overline{\tilde{\omega}\tilde{v}_x}\} - \partial_y\{\bar{\omega}\tilde{v}_y + \bar{v}_y\tilde{\omega} + \tilde{\omega}\tilde{v}_y\} \\ & - \partial_y\tilde{p} + \nu(\partial^2_{xx}\tilde{\omega} + \partial^2_{yy}\tilde{\omega}).\end{aligned} \tag{3.17e}$$

The Reynolds decomposition is exact, meaning no approximations have been made to rewrite the set of equations (3.13) into the set of averaged equations (3.16) with no y-dependence and the set of equations (3.17) for the fluctuations.

3.4.2 Galerkin projection

To reduce the set of equations (3.16)–(3.17), we approximate the fluctuation variables with their truncated Fourier series,

$$\tilde{f}(x,y,t) = \sum_{k=-N}^{N} f_k(x,t)e^{ikay}, \quad a = \frac{2\pi}{L_y}, \quad f = v_x, v_y, \phi, p, \omega.$$

Here, f_k, $k = 0, 1, \ldots, N$ are the Fourier coefficients, and $f_{-k} = f_k^*$, where the asterisk denotes the complex conjugate. To simplify the equations as much as possible, we truncate the series at $N = 1$. Since these variables are zero on average, $f_0 = 0$, and we obtain the truncation

$$\tilde{f}(x,y,t) = f_1(x,t)e^{iay} + f_1^*(x,t)e^{-iay}, \quad f = v_x, v_y, \phi, p, \omega. \tag{3.18}$$

Eqs. (3.16a)–(3.16c) contain no fluctuation terms and require no rewriting. In Eq. (3.16d), the expression $\overline{\tilde{p}\tilde{v}_x}$ enters as the flux of $\bar{p}$. Inserting the truncated expansions (3.18) into this expression yields

$$\begin{aligned}\overline{\tilde{p}\tilde{v}_x} &= \overline{(p_1 e^{iay} + p_1^* e^{-iay})(v_{x,1}e^{iay} + v_{x,1}^* e^{-iay})} \\ &= p_1 v_{x,1}\overline{e^{2iay}} + p_1 v_{x,1}^* + p_1^* v_{x,1} + p_1^* v_{x,1}^* \overline{e^{-2iay}} \\ &= p_1 v_{x,1}^* + p_1^* v_{x,1},\end{aligned}$$

where we have used that $\overline{e^{\pm 2iay}} = 0$ due to L_y-periodicity of that function. Similarly, for the flux of $\bar{\omega}$ in Eq. (3.16e) we get

$$\overline{\tilde{\omega}\tilde{v}_x} = \omega_1 v_{x,1}^* + \omega_1^* v_{x,1}.$$

Inserting the truncated series (3.18) into Eq. (3.17a) gives

$$v_{x,1}e^{iay} + v_{x,1}^* e^{-iay} = -ia\phi_1 e^{iay} + ia\phi_1^* e^{-iay}. \tag{3.19}$$

We now project Eq. (3.19) onto e^{iay} by taking the inner product of each term with e^{iay}. In the current notation the inner product $\langle \cdot, \cdot \rangle$ of two functions f and g is

$$\langle f, g \rangle = \overline{fg^*}.$$

Hence, the projection of Eq. (3.19) onto e^{iay} is

$$v_{x,1} = -ia\phi_1. \tag{3.20a}$$

Similarly, inserting the truncated expansions (3.18) into Eqs. (3.17b)–(3.17c) and projecting onto e^{iay} gives

$$v_{y,1} = \partial_x \phi_1, \tag{3.20b}$$

$$\partial_{xx}^2 \phi_1 = a^2 \phi_1 + \omega_1 - \tau\left(\partial_{xx} p_1 - a^2 p_1\right), \tag{3.20c}$$

$$\partial_t p_1 = -\partial_x\{\bar{p}v_{x,1}\} - ia(\bar{p}v_{y,1} + \bar{v}_y p_1) + \kappa(\partial_{xx}^2 p_1 - a^2 p_1), \tag{3.20d}$$

$$\partial_t \omega_1 = -\partial_x\{\bar{\omega}v_{x,1}\} - ia(\bar{\omega}v_{y,1} + \bar{v}_y \omega_1) - iap_1 + \nu(\partial_{xx}^2 \omega_1 - a^2 \omega_1). \tag{3.20e}$$

To summarize, the reduced model is

$$\bar{v}_y = \partial_x \bar{\phi}, \tag{3.21a}$$
$$\partial_{xx}^2 \bar{\phi} = \bar{\omega} - \tau \partial_{xx}^2 \bar{p}, \tag{3.21b}$$
$$\partial_t \bar{p} = -\partial_x \left\{ p_1 v_{x,1}^* + p_1^* v_{x,1} \right\} + \kappa \partial_{xx}^2 \bar{p} + S, \tag{3.21c}$$
$$\partial_t \bar{\omega} = -\partial_x \left\{ \omega_1 v_{x,1}^* + \omega_1^* v_{x,1} \right\} + \nu \partial_{xx}^2 \bar{\omega}, \tag{3.21d}$$
$$v_{x,1} = -ia\phi_1, \tag{3.21e}$$
$$v_{y,1} = \partial_x \phi_1, \tag{3.21f}$$
$$\partial_{xx}^2 \phi_1 = a^2 \phi_1 + \omega_1 - \tau(\partial_{xx}^2 p_1 - a^2 p_1), \tag{3.21g}$$
$$\partial_t p_1 = -\partial_x \{\bar{p} v_{x,1}\} - ia(\bar{p} v_{y,1} + \bar{v}_y p_1) + \kappa \left(\partial_{xx}^2 p_1 - a^2 p_1 \right), \tag{3.21h}$$
$$\partial_t \omega_1 = -\partial_x \{\bar{\omega} v_{x,1}\} - ia(\bar{\omega} v_{y,1} + \bar{v}_y \omega_1) - iap_1 + \nu(\partial_{xx}^2 \omega_1 - a^2 \omega_1). \tag{3.21i}$$

The pressure source is

$$S(x) = q \mathrm{e}^{-\frac{x^2}{2\sigma^2}}. \tag{3.21j}$$

For the averaged pressure $\bar{p}$ and the fluctuation Fourier coefficient p_1, we apply a Neumann boundary condition at the left boundary, and a zero Dirichlet boundary condition at the right boundary,

$$\partial_x \bar{p}(0,t) = \partial_x p_1(0,t) = 0, \qquad \bar{p}(L_x,t) = p_1(L_x,t) = 0. \tag{3.22a}$$

For the averaged electrostatic potential and perturbed vorticity, and the fluctuation Fourier coefficients of the electrostatic potential and perturbed vorticity, we apply Dirichlet boundary conditions at both the left and right boundaries,

$$\bar{f}(0,t) = \bar{f}(L_x,t) = 0, \qquad f_1(0,t) = f_1(L_x,t) = 0, \quad f = \phi, \omega. \tag{3.22b}$$

As initial condition, each of the averaged system variables is set to zero at $t = 0$,

$$\bar{f}(x,0) = 0, \qquad f = p, \omega, \phi. \tag{3.23a}$$

Some of the fluctuation Fourier coefficients must have nonzero initial values to be allowed to grow. The initial conditions for these coefficients are

$$p_1(x,0) = 10^{-3} \cos\left(\tfrac{\pi x}{2L_x}\right), \quad \omega_1(x,0) = 10^{-3} \sin\left(\tfrac{2\pi x}{L_x}\right), \quad \phi_1(x,0) = 0. \tag{3.23b}$$

Utilizing the approximation (3.18), the three energies (3.12) can be written as

$$P = \langle x\bar{p} \rangle, \qquad N = \langle |v_{x,1}|^2 + |v_{y,1}|^2 \rangle, \qquad F = \frac{1}{2} \langle \bar{v}_y^2 \rangle. \tag{3.24}$$

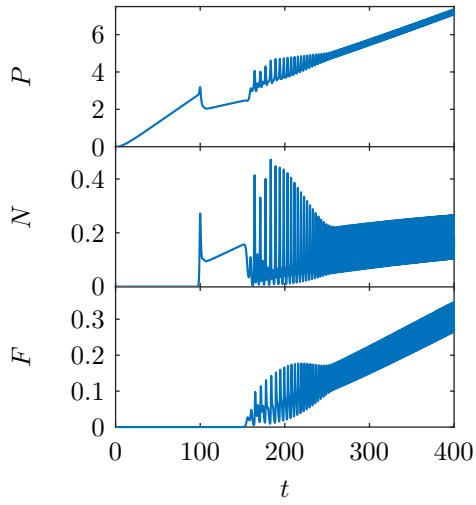

Figure 3.25. For $\tau = 0.00$ and $q(t) = 30t/400$, the time evolution of the energies P, N, and F for the solution to the reduced model.

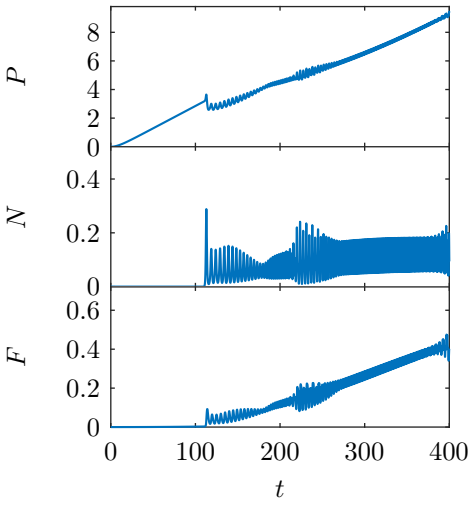

Figure 3.26. For $\tau = 0.02$ and $q(t) = 30t/400$, the time evolution of the energies P, N, and F for the solution to the reduced model.

3.4.3 Solution examples

To compare the reduced problem (3.21)–(3.23) with the full problem (3.4)–(3.6), we again show plots of some solutions where q increases linearly in time from zero to 30.

Figures 3.25–3.28 show the solutions for $\tau = 0.00$, $\tau = 0.02$, $\tau = 0.04$, and $\tau = 0.06$, respectively. These solutions look very similar to the corresponding solutions for full model in Figs. 3.3–3.6. For $\tau = 0$, the solution to the reduced model qualitatively identical to the solution to the full model, but the transitions between states occur at slightly different times. For $\tau = 0.02$, the solution to the full model converges to an equilibrium in the second phase, but the reduced model replaces this phase with an additional oscillating phase. For $\tau = 0.04$, the solutions to the reduced model is again qualitatively identical to the solution to the full model, but the transitions occur at slightly different times. For $\tau = 0.06$, the solutions to the full and reduced models are visually identical.

Solution comparisons for other parameter values are shown in the appendix of this chapter, Section 3.A.

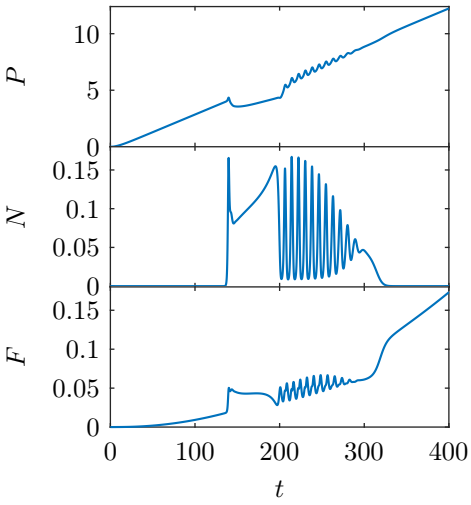

Figure 3.27. For $\tau = 0.04$ and $q(t) = 30t/400$, the time evolution of the energies P, N, and F for the solution to the reduced model.

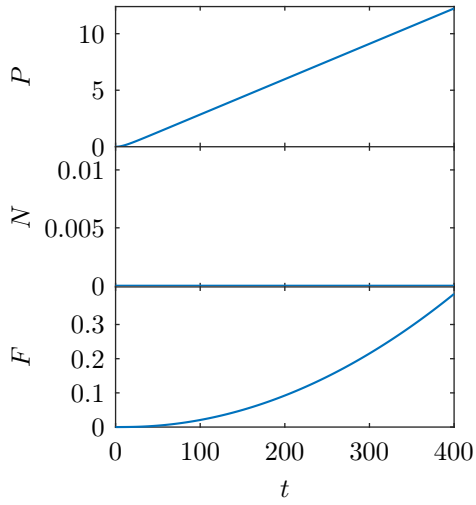

Figure 3.28. For $\tau = 0.06$ and $q(t) = 30t/400$, the time evolution of the energies P, N, and F for the solution to the reduced model.

3.4.4 Data-based bifurcation diagrams

For $\tau = 0$, simulation data for P, N, and F was generated for $q \in \{0, 0.1, \ldots, 10\}$ by solving the reduced model (3.21)–(3.23). By approximately identifying the location of all equilibrium points for each solution, the data-based bifurcation diagram shown in Fig. 3.29 was generated. This bifurcation diagram is very similar to the data-based bifurcation diagram for the original PDE problem in Fig. 3.23: The same types of bifurcations occur, but they occur at slightly different shifted values of q.

Similarly, for $\tau = 0.04$, simulation data for P, N, and F was generated for $q \in \{0, 0.2, \ldots, 24\}$ by solving the reduced model (3.21)–(3.23). By approximately identifying the location of all equilibrium points for each solution, the data-based bifurcation diagram shown in Fig. 3.30 was generated. This bifurcation diagram is similar to the data-based bifurcation diagram for the original PDE problem in Fig. 3.24: The same types of bifurcations occur, but they occur at slightly different shifted values of q.

For these chosen parameter values, the reduced model approximates the full model well.

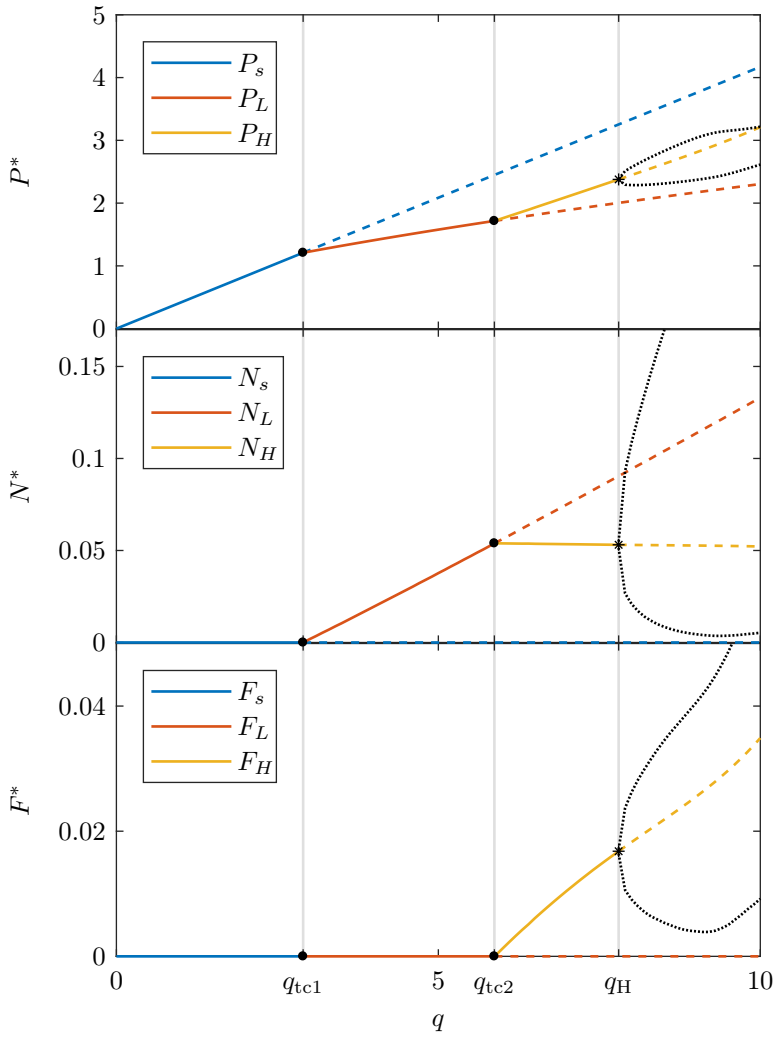

Figure 3.29. Bifurcation diagram generated from simulation data for $\tau = 0$. Solid curves are stable equilibrium points, dashed curves are unstable equilibrium points, while the dotted curves show the amplitude of the stable limit cycle. The transcritical bifurcations occurring at approximately $q_{\mathrm{tc1}} \approx 2.90$ and $q_{\mathrm{tc2}} \approx 5.87$ are marked with dots, while the Hopf bifurcation occurring at $q_{\mathrm{H}} \approx 7.80$ is marked with asterisks.

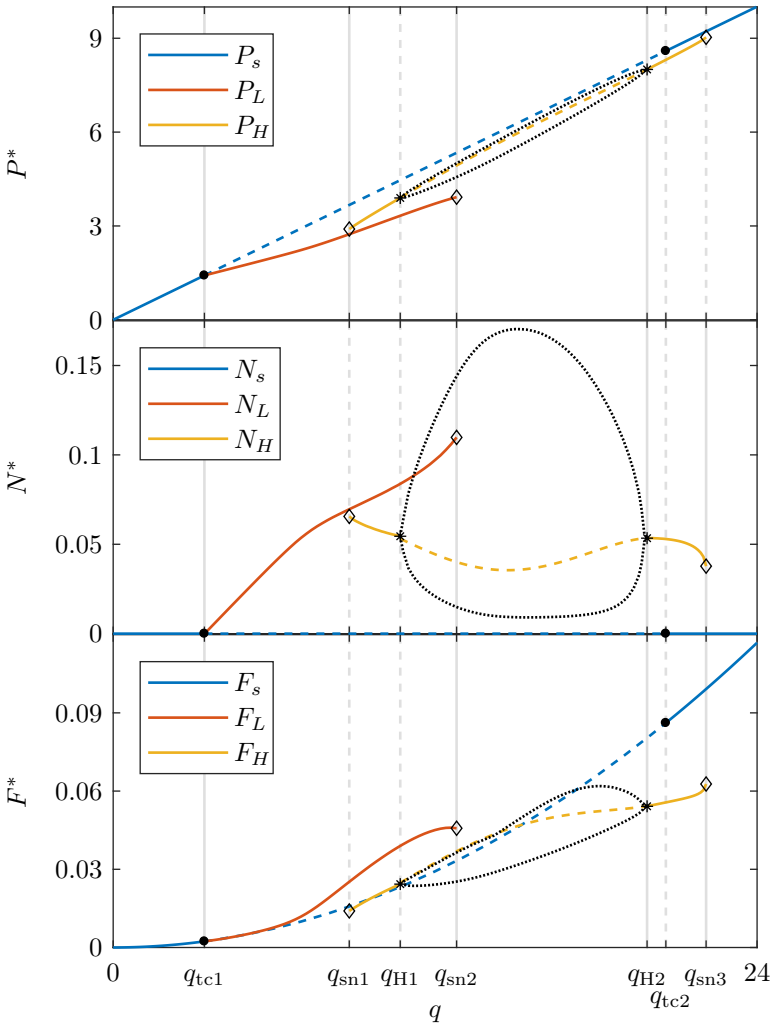

Figure 3.30. Bifurcation diagram generated from simulated data for $\tau = 0.04$. Solid curves are stable equilibrium points, dashed curves are unstable equilibrium points, while the dotted curve show the amplitude of oscillations. The blue curve is the s-equilibrium, the red curve is the L-equilibrium, and the yellow curve is the H-equilibrium. The transcritical bifurcations occurring at approximately $q_{\mathrm{tc1}} \approx 3.4$ and $q_{\mathrm{tc2}} \approx 20.6$ are marked with dots, the saddle-node bifurcations occurring at $q_{\mathrm{sn1}} \approx 8.8$, $q_{\mathrm{sn2}} \approx 12.8$, $q_{\mathrm{sn3}} \approx 22.1$ are marked with diamonds, while the Hopf-bifurcations occurring at $q_{\mathrm{H1}} \approx 10.7$ and $q_{\mathrm{H2}} \approx 19.9$ are marked with asterisks.

3.5 Conclusion

A convection problem with a pressure source centered at the left boundary models the plasma dynamics at the edge of a magnetically confined plasma. The vorticity is perturbed by a term directly proportional to the pressure curvature. The introduction of this perturbation is inspired by the generalized vorticity in the HESEL model [44]. The perturbation of the vorticity generates an additional zonal flow in the plasma.

The solution to the convection problem is characterized by three state variables: the potential energy related to the pressure gradient, P, the fluctuation energy, N, and the zonal flow energy, F. Depending on the strength of the pressure source, q, we identified four different types of solutions to the convection problem. Three of these solution types corresponded to equilibrium points and the fourth type corresponded to a limit cycle in the (P, N, F)-state space. For perturbed and unperturbed vorticity, simulation data was generated for multiple fixed values of q by computing and saving the three energy variables P, N, and F at each output time step while solving the convection problem. Data-based bifurcation diagrams were constructed for the convection model with the unperturbed vorticity and with the perturbed vorticity. The perturbation of the vorticity alters the bifurcation diagram significantly, resulting in phenomena such as dual-stability and hysteresis.

By carrying out a Reynolds decomposition of each state variable in the 2D convection model, followed by a Fourier series approximation and Galerkin projection, we derive a reduced convection model, which requires significantly less computational resources to solve. The data-based bifurcation diagrams for the reduced model reveal that the reduced model has the same bifurcation structure as the full model.

We have demonstrated an approach to derive 1D reduced models from 2D plasma models. For the set of investigated parameter values, the reduced model contains the same physics as the full model. In comparison to the full 2D model, the less computationally demanding 1D model allows easier analysis of parameter dependence and the connection of specific terms to specific physics.

3.A Appendix: Solution comparisons for other parameter values

This section contains comparisons of solutions to the full model (3.4)–(3.6) and the reduced model (3.21)–(3.23) for parameter values different from the ones listed in Table 3.1. In all cases the source strength ramps up as linearly in time as $q(t) = 30t/400$, and the solution is obtained for $t \in [0, 400]$.

Figures 3.31–3.38 show comparisons for $\mathrm{Ra} = 625$ corresponding to $\nu = \kappa = 0.04$ for $\tau = 0$, 0.02, 0.04, and 0.06. For the same set of parameter values, the exact solutions to the full model and the reduced model differ visibly, but qualitatively the solutions seem to be follow the same pattern of transitions between different modes as q increases.

Figures 3.39–3.42 show comparisons for $\mathrm{Ra} = 2500$ corresponding to $\nu = \kappa = 0.02$ for $\tau = 0$ and $\tau = 0.02$. For the same set of parameter values, we see again the same qualitative transitional behavior for the full model and the reduced model.

Figures 3.43–3.48 show comparisons for $L_y = 1.2$ for $\tau = 0$, 0.02, and 0.04. For the same set of parameter values, the same solutions are qualitative similar for the full model and the reduced model.

Figures 3.49–3.50 show comparisons for $L_y = 1.4$ for $\tau = 0$. Here, no zonal flow is generated in the full model, while the solution to the reduced model is qualitatively similar to the $L_y = 1.2$ solution. Accordingly, the solutions to the full model and the reduced model are qualitatively different for $L_y = 1.4$.

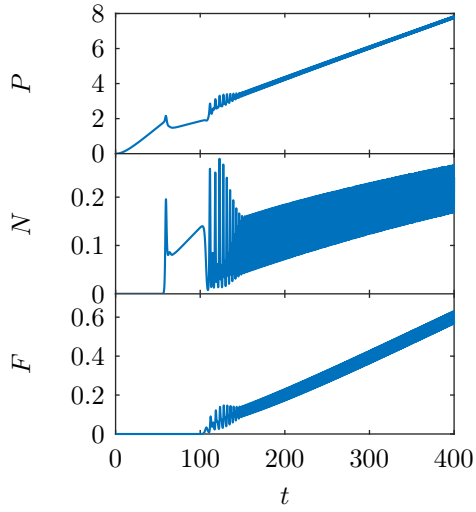

Figure 3.31. For Ra = 625, the $\tau = 0$ solution to the full problem for $q(t) = 30t/400$.

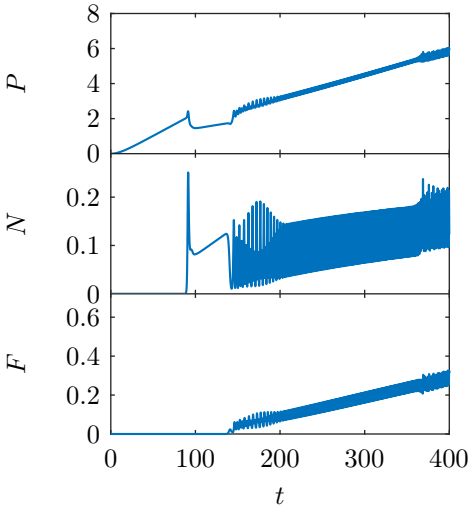

Figure 3.32. For Ra = 625, the $\tau = 0$ solution to the reduced problem for $q(t) = 30t/400$.

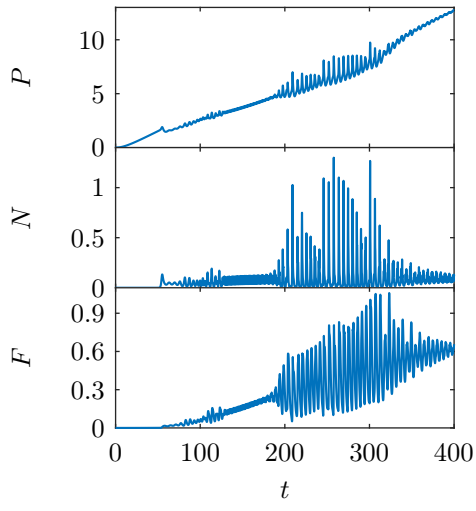

Figure 3.33. For Ra = 625, the $\tau = 0.02$ solution to the full problem for $q(t) = 30t/400$.

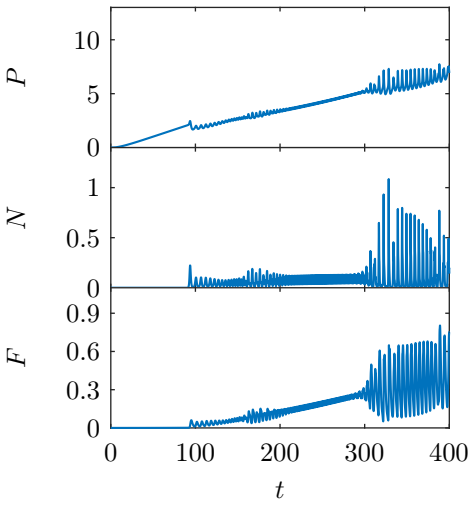

Figure 3.34. For Ra = 625, the $\tau = 0.02$ solution to the reduced problem for $q(t) = 30t/400$.

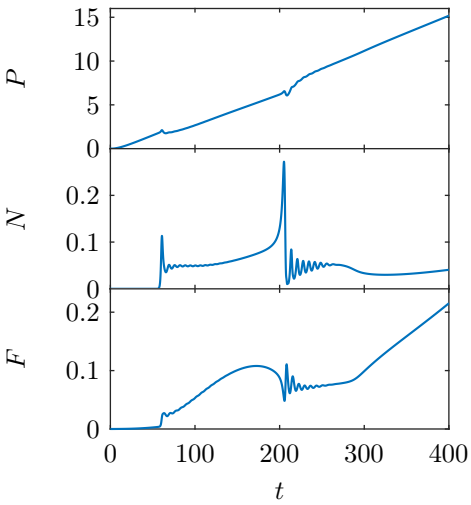

Figure 3.35. For Ra = 625, the $\tau = 0.04$ solution to the full problem for $q(t) = 30t/400$.

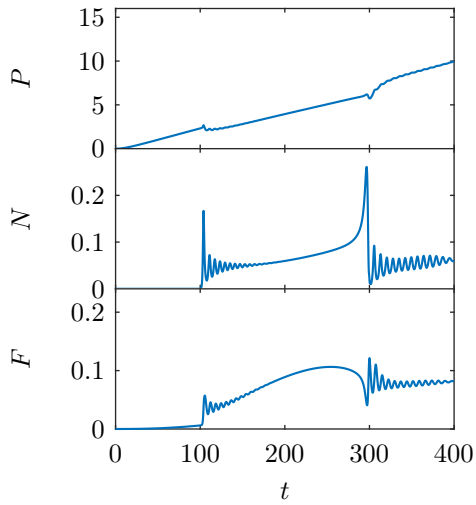

Figure 3.36. For Ra = 625, the $\tau = 0.04$ solution to the reduced problem for $q(t) = 30t/400$.

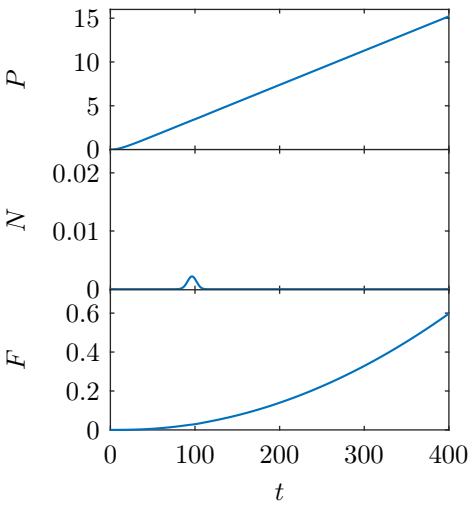

Figure 3.37. For Ra = 625, the $\tau = 0.06$ solution to the full problem for $q(t) = 30t/400$.

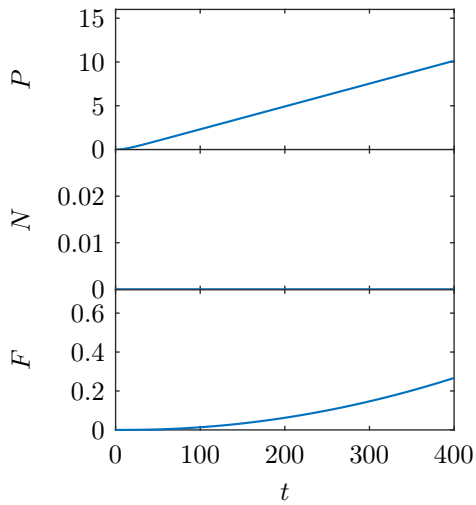

Figure 3.38. For Ra = 625, the $\tau = 0.06$ solution to the reduced problem for $q(t) = 30t/400$.

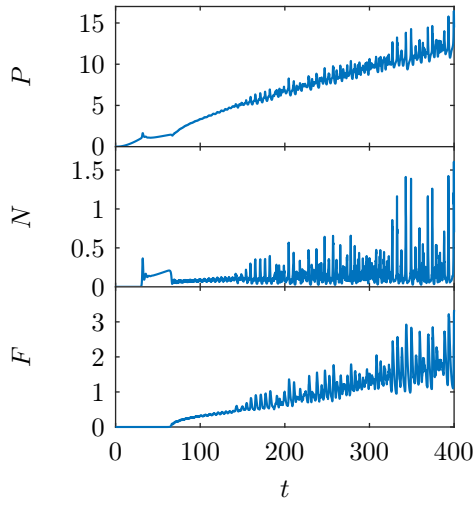

Figure 3.39. For Ra = 2500, the $\tau = 0$ solution to the full problem for $q(t) = 30t/400$.

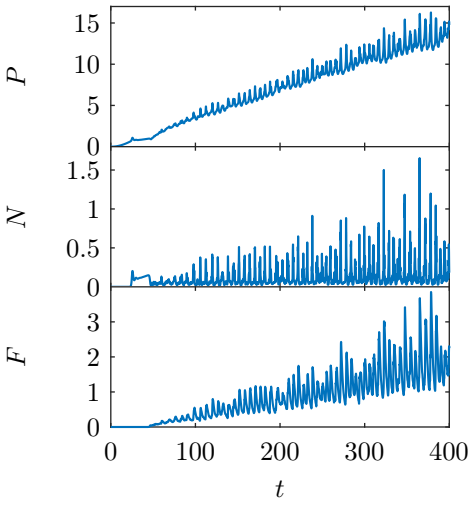

Figure 3.40. For Ra = 2500, the $\tau = 0$ solution to the reduced problem for $q(t) = 30t/400$.

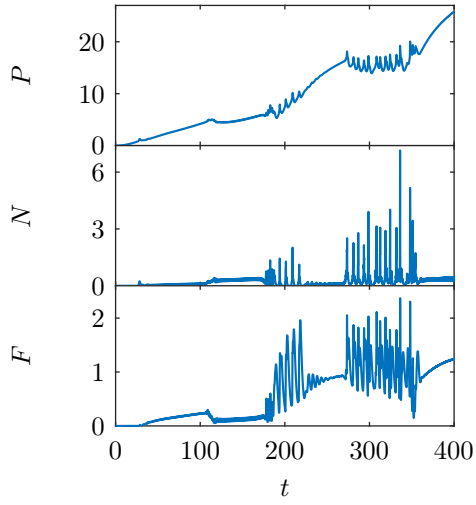

Figure 3.41. For Ra = 2500, the $\tau = 0.02$ solution to the full problem for $q(t) = 30t/400$.

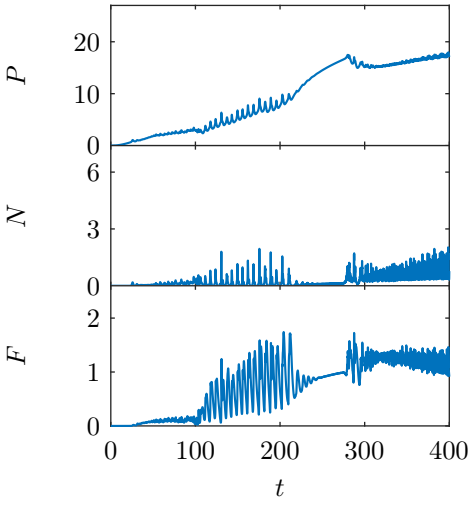

Figure 3.42. For Ra = 2500, the $\tau = 0.02$ solution to the reduced problem for $q(t) = 30t/400$.

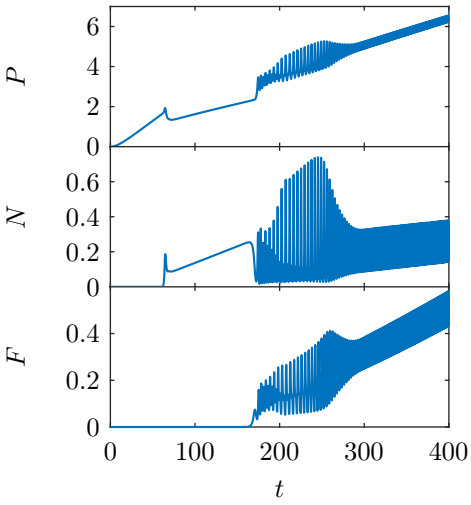

Figure 3.43. For $L_y = 1.2$, the $\tau = 0$ solution to the full problem for $q(t) = 30t/400$.

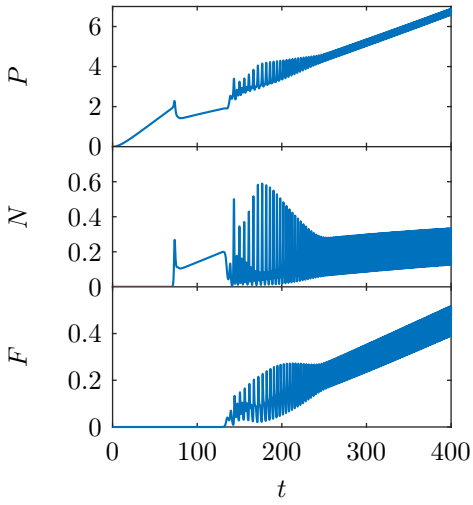

Figure 3.44. For $L_y = 1.2$, the $\tau = 0$ solution to the reduced problem for $q(t) = 30t/400$.

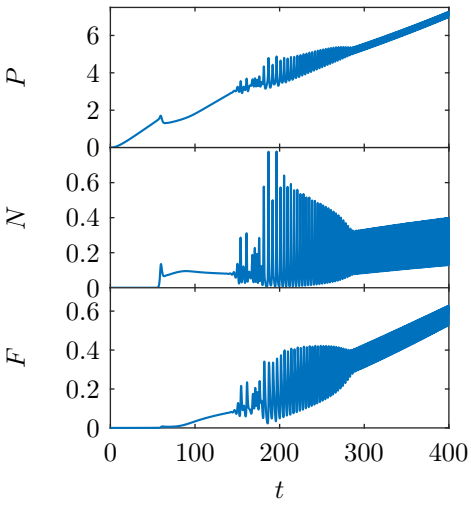

Figure 3.45. For $L_y = 1.2$, the $\tau = 0.02$ solution to the full problem for $q(t) = 30t/400$.

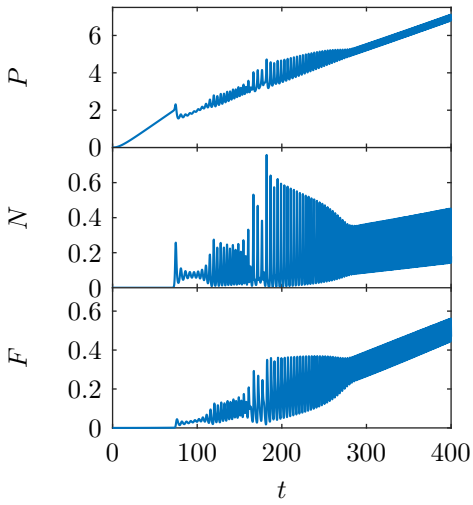

Figure 3.46. For $L_y = 1.2$, the $\tau = 0.02$ solution to the reduced problem for $q(t) = 30t/400$.

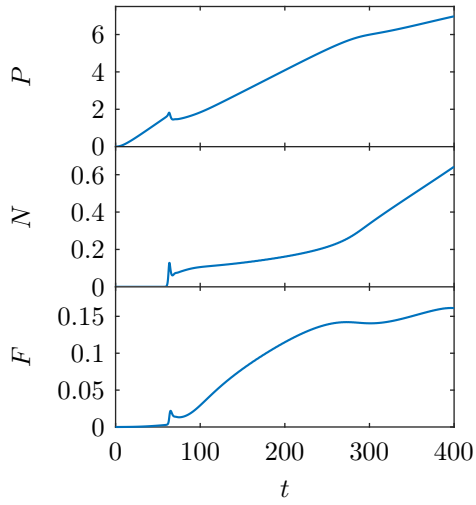

Figure 3.47. For $L_y = 1.2$, the $\tau = 0.04$ solution to the full problem for $q(t) = 30t/400$.

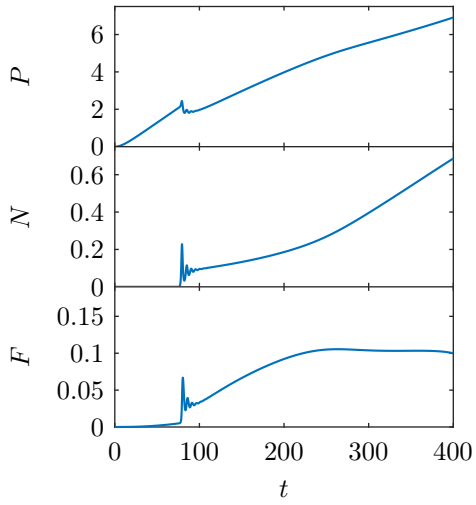

Figure 3.48. For $L_y = 1.2$, the $\tau = 0.04$ solution to the reduced problem for $q(t) = 30t/400$.

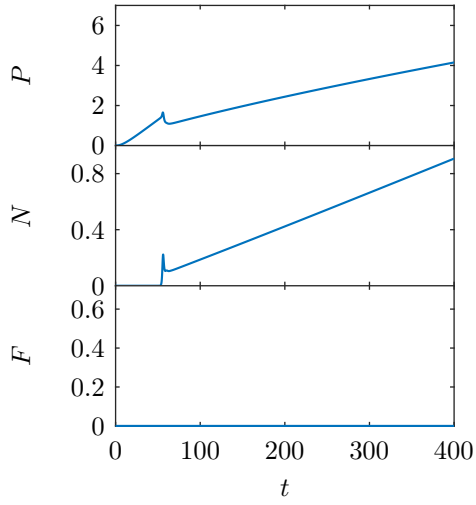

Figure 3.49. For $L_y = 1.4$, the $\tau = 0$ solution to the full problem for $q(t) = 30t/400$.

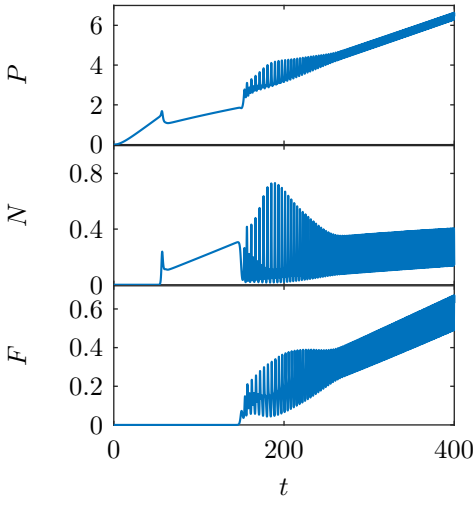

Figure 3.50. For $L_y = 1.4$, the $\tau = 0$ solution to the reduced problem for $q(t) = 30t/400$.

Chapter 4

Sparse identification of a predator-prey system from simulation data of a convection model

The use of low-dimensional dynamical systems as reduced models for plasma dynamics is useful as solving an initial value problem requires much less computational resources than fluid simulations. We utilize a data-driven modeling approach to identify a reduced model from simulation data of a convection problem. A convection model with a pressure source centered at the inner boundary models the edge dynamics of a magnetically confined plasma. The convection problem undergoes a sequence of bifurcations as the strength of the pressure source increases. The time evolution of the energies of the pressure profile, the turbulent flow, and the zonal flow capture the fundamental dynamic behavior of the full system. By applying the sparse identification of nonlinear dynamics (SINDy) method, we identify a predator-prey type dynamical system that approximates the underlying dynamics of the three energy state variables. A bifurcation analysis of the system reveals consistency between the bifurcation structures, observed for the simulation data, and the identified underlying system. An attempt to identify a reduced model from simulation data of a perturbed vorticity convection problem was unsuccessful.

The results in this chapter are published in Physics of Plasmas [23].

4.1 Introduction

The perpendicular edge transport of a magnetically confined plasma is largely governed by convective plasma flows. The plasma flows can be decomposed into a non-zonal (turbulent, fluctuating) flow and a zonal flow. The non-zonal flow increases the radial transport and generates a Reynolds stress that drives the zonal flow. The zonal flow is in the poloidal direction along the magnetic flux surfaces and varies radially. This sheared poloidal flow constitutes a transport barrier that decreases the radial transport of plasma. While the zonal flow is turbulence-driven, it also suppresses the turbulent flow. This type of interaction between the turbulent energy and the zonal flow energy resembles mathematically the interaction between populations of predators and preys. The interaction between turbulent flow and zonal flow has therefore been modeled by predator-prey systems, where the zonal flow acts as the predator and the turbulent flow acts as the prey [38, 62]. The creation of an edge transport barrier formed by a sheared zonal flow is closely related to the L–H transition [69]. Ordinary differential equation (ODE) models for the L–H transition are based on the predator-prey relationship between zonal flow and turbulent flow, and incorporate a potential energy related to the pressure profile as an additional state variable [6, 8, 22, 46, 56, 68, 78–80]. Miki et al. [60] and Wu et al. [77] have both suggested 1D partial differential equation (PDE) models for the L–H transition based on this predator-prey relationship.

Reduced ODE models, describing the interaction between zonal flow and turbulent flow, are very useful. ODE models require much less computational resources to solve and they are much easier to analyze than the corresponding fluid equations. When building a mathematical model, there are basically two different approaches to choose among. The first one is physical modeling, where the model is derived from theory. The second approach is system identification [53], where observed data from the real system is used to model the system. System identification is a large and diverse field and many methods exist for determining the governing equations of a system from data. The choice of an identification method depends on the desired model type, prior knowledge about the model structure, and other model assumptions.

Most current predator-prey models for the interaction between zonal flow and turbulent flow are obtained by physical modeling with many approximations and assumptions. The Ball-Dewar-Sugama model [8] is loosely derived from approximate resistive magnetohydrodynamics momentum and pressure convection equations, and the Kim-Diamond model [46] is loosely derived from the linearized wave-kinetic equation. Even though these models reproduce qualitative dynamics similar to experimental observations, they fail to be quantitatively predictive. Kobayashi, Gürcan, and Diamond [48] use an identification approach, where

they assume that a Lotka-Volterra model describes the interaction between zonal flow and turbulent flow, and fit the model coefficients to data obtained from full gyrokinetic simulations. However, this simple model fails to describe the dynamics away from the limit cycle attractor.

This chapter demonstrates an alternative approach for building ODE models for plasma dynamics. We extract a model from data instead of obtaining the model using physics-based arguments. Specifically, we determine the underlying structure of a nonlinear dynamical system from simulations of a convection problem with a pressure source centered at the left boundary. The convection problem undergoes a sequence of transitions as the strength of the pressure source increases. These transitions are similar to the ones observed in more accurate plasma models. The time evolution of the energies of the pressure profile, the turbulent flow, and the zonal flow captures the bifurcating behavior of the full convection problem. We model these three energy state variables with a continuous deterministic dynamical system and assume no prior knowledge about the structure of the dynamical system. For the system identification process we apply the sparse identification of nonlinear dynamics (SINDy) method [17] and aim to build a model that quantitatively reproduces the dynamics and bifurcations observed in the simulation data. The method is general enough that the same approach can be used if the simulation data were replaced by measurement data.

4.2 Sparse identification of nonlinear dynamics (SINDy)

System identification is a modeling approach where observed data from a real system is used to built a model of the system [54]. System identification is a large and diverse field and many methods exist for determining the governing equations of a system from data [53]. Which identification method to choose depends on which type of model we want, how much prior knowledge we have about the model structure, and which other assumptions we make about the model. In the present case, we assume no prior knowledge about the structure of the dynamical system, and we want to model the system with a continuous deterministic nonlinear dynamical system. To obtain this we choose to use the method called SINDy (Sparse identification of nonlinear dynamics) [17].

In their paper, Brunton, Proctor, and Kutz [17] describe thoroughly the SINDy algorithm. Here, we give a summary of the algorithm, followed by a test of our implementation of the algorithm in Matlab.

4.2.1 The SINDy algorithm

SINDy [17] is a method that seeks to identify an underlying dynamical system from time-series data. We give here a brief summary of the algorithm description. Based on a set of data we seek a dynamical system,

$$\dot{\boldsymbol{x}} = \boldsymbol{f}(\boldsymbol{x}), \qquad \boldsymbol{x} \in \mathbb{R}^n. \tag{4.1}$$

Here, $\boldsymbol{x}(t) = \begin{bmatrix} x_1(t) & x_2(t) & \cdots & x_n(t) \end{bmatrix}^\intercal$ is the state variable vector and $\boldsymbol{f} = \begin{bmatrix} f_1(x) & f_2(x) & \cdots & f_n(x) \end{bmatrix}^\intercal$ is the vector field. We want to determine the function $\boldsymbol{f}$ from data. In the data-collection process, we sample a time-series of the state $\boldsymbol{x}(t)$ and either measure the derivative $\dot{\boldsymbol{x}}(t)$ or approximate it numerically from the time-series of $\boldsymbol{x}(t)$. The data $\boldsymbol{x}(t_\ell)$ and $\dot{\boldsymbol{x}}(t_\ell)$, $\ell = 1, \ldots, m$ is arranged into two matrices

$$\boldsymbol{X} = \begin{bmatrix} \boldsymbol{x}^\intercal(t_1) \\ \boldsymbol{x}^\intercal(t_2) \\ \vdots \\ \boldsymbol{x}^\intercal(t_m) \end{bmatrix} = \begin{bmatrix} x_1(t_1) & x_2(t_1) & \cdots & x_n(t_1) \\ x_1(t_2) & x_2(t_2) & \cdots & x_n(t_2) \\ \vdots & \vdots & \ddots & \vdots \\ x_1(t_m) & x_2(t_m) & \cdots & x_n(t_m) \end{bmatrix},$$

$$\dot{\boldsymbol{X}} = \begin{bmatrix} \dot{\boldsymbol{x}}^\intercal(t_1) \\ \dot{\boldsymbol{x}}^\intercal(t_2) \\ \vdots \\ \dot{\boldsymbol{x}}^\intercal(t_m) \end{bmatrix} = \begin{bmatrix} \dot{x}_1(t_1) & \dot{x}_2(t_1) & \cdots & \dot{x}_n(t_1) \\ \dot{x}_1(t_2) & \dot{x}_2(t_2) & \cdots & \dot{x}_n(t_2) \\ \vdots & \vdots & \ddots & \vdots \\ \dot{x}_1(t_m) & \dot{x}_2(t_m) & \cdots & \dot{x}_n(t_m) \end{bmatrix}.$$

We construct an augmented library $\boldsymbol{\Theta}(\boldsymbol{X})$ consisting of candidate functions of the columns of $\boldsymbol{X}$. The candidate functions could be a constant, polynomials, trigonometric terms, etc. Here, we will be using polynomial terms as candidate functions,

$$\boldsymbol{\Theta}(\boldsymbol{X}) = \begin{bmatrix} \boldsymbol{1} & \boldsymbol{X} & \boldsymbol{X}^{P_2} & \boldsymbol{X}^{P_3} & \cdots \end{bmatrix},$$

where $\boldsymbol{X}^{P_i}$ are ith order polynomials of $\boldsymbol{X}$. Each column of $\boldsymbol{\Theta}(\boldsymbol{X})$ represents a candidate function for the vectorfield $\boldsymbol{f}(\boldsymbol{x})$. We assume that only a few of these terms are active in each row of $\boldsymbol{f}(\boldsymbol{x})$. We can then write $\boldsymbol{f}(\boldsymbol{X}) = \boldsymbol{\Theta}(\boldsymbol{X})\boldsymbol{\Xi}$, where $\boldsymbol{\Xi} = \begin{bmatrix} \boldsymbol{\xi}_1 & \boldsymbol{\xi}_2 & \cdots & \boldsymbol{\xi}_n \end{bmatrix}$ is a sparse matrix of coefficients. The coefficients matrix $\boldsymbol{\Xi}$ can be determined from the sparse regression problem

$$\dot{\boldsymbol{X}} = \boldsymbol{\Theta}(\boldsymbol{X})\boldsymbol{\Xi}. \tag{4.2}$$

Each column $\boldsymbol{\xi}_k$ of $\boldsymbol{\Xi}$ is a sparse vector of coefficients and determines which terms are active in the right-hand side of the corresponding row equation $\dot{x}_k = f_k(\boldsymbol{x})$ in (4.1). Once $\boldsymbol{\Xi}$ has been determined, each row of $\boldsymbol{f}$ may be determined by

$$\dot{x}_k = f_k(\boldsymbol{x}) = \boldsymbol{\Theta}(\boldsymbol{x}^\intercal)\boldsymbol{\xi}_k, \quad k = 1, \ldots, n.$$

To solve for $\boldsymbol{\Xi}$ in (4.2), we implement the algorithm described in Ref. [17]. Let $\boldsymbol{\Theta}(\boldsymbol{X})$ have dimensions $m \times p$ where p is the number of candidate functions and m the number of time samples. We assume $m \gg p$ since there are many more time samples of data than there are candidate functions. Since both $\boldsymbol{X}$ and $\dot{\boldsymbol{X}}$ are generally contaminated with noise, (4.2) does not hold exactly. Instead

$$\dot{\boldsymbol{X}} = \boldsymbol{\Theta}(\boldsymbol{X})\boldsymbol{\Xi} + \eta \boldsymbol{Z}, \tag{4.3}$$

where $\boldsymbol{Z}$ is a matrix of independent identically distributed Gaussian entries with zero mean, and η is the noise magnitude. We seek to solve for $\boldsymbol{\Xi}$ in (4.3). To ensure the restricted isometry property holds, we normalize the columns of $\boldsymbol{\Theta}(\boldsymbol{X})$ to a length of 1 by dividing each column by the ℓ^2-norm of that column [74]. Let $\boldsymbol{l}_2$ denote the vector of ℓ^2-norms of the columns of $\boldsymbol{\Theta}(\boldsymbol{X})$. We use that $\mathrm{diag}(1/\boldsymbol{l}_2) = [\mathrm{diag}(\boldsymbol{l}_2)]^{-1}$ to define a scaled coefficients matrix such that the structure of (4.3) is unchanged,

$$\boldsymbol{\Theta}(\boldsymbol{X})\boldsymbol{\Xi} = \underbrace{\boldsymbol{\Theta}(\boldsymbol{X})\mathrm{diag}(1/\boldsymbol{l}_2)}_{\boldsymbol{\Theta}_{\mathrm{sc}}(\boldsymbol{X})} \underbrace{\mathrm{diag}(\boldsymbol{l}_2)\boldsymbol{\Xi}}_{\boldsymbol{\Xi}_{\mathrm{sc}}} = \boldsymbol{\Theta}_{\mathrm{sc}}(\boldsymbol{X})\boldsymbol{\Xi}_{\mathrm{sc}}.$$

The implementation in Matlab for the normalization of $\boldsymbol{\Theta}(\boldsymbol{X})$ is

```
l2 = sqrt(sum(Theta.^2,1))'; % The l2—norm of each column of Theta
% Arrange 1/l2 in a sparse diagonal matrix of size p x p
l2diaginv = spdiags(1./l2,0,p,p);
Theta = Theta*l2diaginv; % Normalize each column of Theta to 1
```

The normalized coefficient matrix $\boldsymbol{\Xi}_{\mathrm{sc}}$ is now computed with the sequential thresholded least-squares algorithm

```
%% compute Sparse regression: sequential least squares
Xi = Theta\dXdt; % initial guess: Least—squares
% lambda is our vector of sparsification knobs.
for k=1:10
    smallinds = (abs(Xi)<ones(p,1)*lambda); % find small
        coefficients
    Xi(smallinds)=0; % and threshold
    for ind = 1:n % n is state dimension
        biginds = ~smallinds(:,ind);
        % Regress dynamics onto remaining terms to find sparse Xi
        Xi(biginds,ind) = Theta(:,biginds)\dXdt(:,ind);
    end
end
```

In the algorithm, $\boldsymbol{\Xi}_{\mathrm{sc}}$ is initialized as the least-squares solution. In each column of $\boldsymbol{\Xi}_{\mathrm{sc}}$, all elements in the coefficient vector $\boldsymbol{\xi}_{k,\mathrm{sc}}$, smaller than a threshold value

λ_k, are set to zero. Then, a new least-squares solution for $\boldsymbol{\Xi}_{\text{sc}}$ is obtained for the remaining non-zero indices. These new coefficients are again set to zero if they are smaller than their column's threshold value, λ_k, and the procedure is continued until the non-zero elements of $\boldsymbol{\Xi}_{\text{sc}}$ converge. Finally, the non-normalized coefficient matrix is given by $\boldsymbol{\Xi} = \text{diag}(1/\boldsymbol{l}_2)\boldsymbol{\Xi}_{\text{sc}}$. The implementation code in Matlab for this is

```
Xi = l2diaginv*Xi; % The non-normalized Xi
```

The algorithm is easily adjusted to include dependence on a parameter, i.e., to consider systems on the form

$$\dot{\boldsymbol{x}} = \boldsymbol{f}(\boldsymbol{x}; \mu), \qquad \boldsymbol{x} \in \mathbb{R}^n. \tag{4.4}$$

The parameter μ is simply treated as an additional state variable with zero time derivative in the algorithm. The identification must then be based on a collection of time series of the state variables obtained for multiple fixed values of the parameter. The algorithm also allows time-dependence and external forcing of the vector field, i.e., systems on the form

$$\dot{\boldsymbol{x}} = \boldsymbol{f}(\boldsymbol{x}, \boldsymbol{u}(t), t), \qquad \boldsymbol{x} \in \mathbb{R}^n. \tag{4.5}$$

Here, the time variable t and the external forcing $\boldsymbol{u}(t)$ are just added in the algorithm as additional variables.

4.2.2 Algorithm test

To test the implementation of the algorithm in Matlab, we use simulation data collected from a known dynamical system, to test whether the algorithm can identify the dynamical system from the data alone. We consider the following model, which is a modification of the Ball-Dewar-Sugama L–H transition model [5, 8] to include only polynomial terms of the state variables P, N and F:

$$\dot{P} = q - \chi P - \gamma PN, \tag{4.6a}$$

$$\dot{N} = \gamma PN - \beta N^2 - \alpha NF, \tag{4.6b}$$

$$\dot{F} = \alpha NF - aPNF. \tag{4.6c}$$

We use the parameter values listed in Table 4.1. We collect simulation data from $t = 0$ to $t = 50$ with a time step of $\Delta t = 0.05$. A plot of the resulting solution is shown in Fig. 4.1. The time-derivatives are calculated by inserting the solution $(P(t), N(t), F(t))$ into the right-hand side of Eq. (4.6).

q	χ	γ	β	α	a
0.5	0.1	5.0	20.0	200	280

Table 4.1. Parameter values for Eqs. (4.6) and (4.8).

φ	b
0.05	0.4

Table 4.2. Parameter values for the non-polynomial terms in Eq. (4.8).

We choose the augmented library $\boldsymbol{\Theta}(\mathbf{X})$ to consist of candidate polynomials up to third order,

$$\boldsymbol{\Theta}(\mathbf{X}) = \begin{bmatrix} \mathbf{1} & \mathbf{P} & \mathbf{N} & \mathbf{F} & \mathbf{P}^2 & \cdots & \mathbf{F}^2 & \mathbf{P}^3 & \cdots & \mathbf{F}^3 \end{bmatrix}. \tag{4.7}$$

The SINDy algorithm rediscover all the right terms and the values of the six parameters are determined with high precision. This shows that the algorithm works exactly as intended.

For this test, we included candidate polynomials up to third order. If the order of polynomials included becomes too high, a degeneracy in the sparse identification algorithm occurs, where the low-order polynomials are being approximated by high-order polynomials. This can be avoided by initially running the SINDy algorithm with only low-order terms, and then subsequently include higher order terms until the algorithm either converges or diverges.

The paper by Brunton, Proctor, and Kutz [17] includes a demonstration of how well the algorithm works when the data is contaminated with noise. The data, we will be working with, is simulated and represents a true solution to the problem. However, it is very likely that the data can not be represented by a polynomial dynamical system.

To test how well the algorithm works when we attempt to identify a non-polynomial dynamical system by using only polynomial candidate functions, we consider the Ball-Dewar-Sugama model [5, 8] for the L–H transition given by Eqs. (4.6a), (4.6b) and

$$\dot{F} = \alpha N F - \mu F + \varphi F^{1/2}, \tag{4.8a}$$

$$\mu = b P^{-3/2} + a P N. \tag{4.8b}$$

Compared to the polynomial model (4.6), the equation for F now has two additional non-polynomial terms. For the polynomial terms, we again use the parameter values listed in Table 4.1, and for the non-polynomial terms, we use the parameter values listed in Table 4.2. The parameter values are chosen such that the dynamics is still dominated by the polynomial terms. Simulation data is collected following the same procedure as in the previous case.

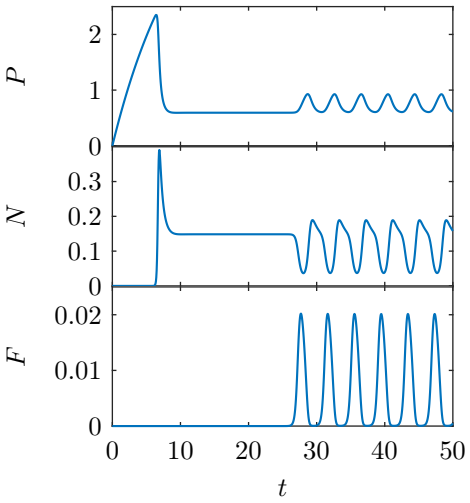

Figure 4.1. Solution example of the dynamical system (4.6) with the parameter values listed in Table 4.1 and initial condition $P(0) = N(0) = F(0) = 10^{-20}$.

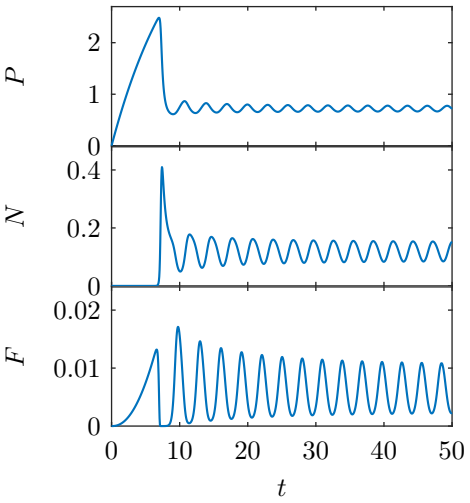

Figure 4.2. Solution example of the model (4.6a)–(4.6b) and (4.8) with the parameter values listed in Table 4.1–4.2 and initial condition $P(0) = 10^{-3}$, $N(0) = F(0) = 10^{-20}$.

Figure 4.2 shows a plot of the simulation data. We use the same augmented library (4.7) as before with candidate polynomials up to third order. The coefficients in the equations for P and N, i.e. Eqs. (4.6a) and (4.6b) are again identified with high precision. The equation for F is identified to be on the form

$$\dot{F} = \alpha_2 NF - aPNF$$

with $\alpha_2 = 189.7377$, $a = 268.1396$. In this case, where the polynomial terms are dominating, the two non-polynomial terms are identified as modifications to the coefficients of the correctly identified polynomial terms.

When working with data generated by non-polynomial systems, the sparsity coefficients λ_k in the SINDy algorithm must be chosen by the trial and error method until SINDy identifies a satisfactory number of active terms. The number of desired terms is a modeling choice that must be made based on a combination of prior knowledge about the model structure and by computing test solutions to the different possible models, to see which model most accurately reproduces the data.

4.3 Simulation data generation

We consider viscous plasma flow in a rectangular domain at the edge of a magnetically confined plasma in the plane perpendicular to the magnetic field $\boldsymbol{B} = B_0 \boldsymbol{e}_z$. The flow is described using Cartesian coordinates $(x, y) \in M$, where $M = [-\frac{2}{5}L_x, \frac{3}{5}L_x] \times [-\frac{1}{2}L_y, \frac{1}{2}L_y]$.

We again model the plasma dynamics with the convection model (3.4) and use the parameters in Table 3.1. The different states the solutions approach and the data-based bifurcation diagrams for the solutions to the model with $\tau = 0$ and $\tau = 0.04$ are shown in Section 3.3.5.

For each time step, we store the potential energy related to the pressure profile P, the turbulent energy N, and the zonal flow energy F, defined by

$$P = \langle \overline{xp} \rangle, \qquad N = \frac{1}{2}\langle \overline{\tilde{v}_x^2} + \overline{\tilde{v}_y^2} \rangle, \qquad F = \frac{1}{2}\langle \bar{v}_y^2 \rangle. \tag{4.9}$$

In addition, we save for each time step the numerically computed time-derivatives $\dot{P}$, $\dot{N}$, and $\dot{F}$.

For $\tau = 0$, the time-derivatives of the energies (4.9) for the system (3.4) can be written as

$$\dot{P} = q\frac{\sigma^2}{L_x}\left(1 - \mathrm{e}^{-\frac{L_x^2}{2\sigma^2}}\right) + \kappa\langle \overline{x\partial_{xx}^2 p} \rangle + \langle \overline{v_x p} \rangle, \tag{4.10a}$$

$$\dot{N} = -\langle \overline{v_x p} \rangle - \nu\langle \overline{\Omega^2} \rangle - \nu\langle \bar{v}_y \partial_{xx}^2 \bar{v}_y \rangle + \langle \bar{v}_y \partial_x \overline{\tilde{v}_x \tilde{v}_y} \rangle, \tag{4.10b}$$

$$\dot{F} = -\langle \bar{v}_y \partial_x \overline{\tilde{v}_x \tilde{v}_y} \rangle + \nu\langle \bar{v}_y \partial_{xx}^2 \bar{v}_y \rangle. \tag{4.10c}$$

A physical modeling approach would use this set of equations as a starting point. In Eq. (4.10a), the source term, which is proportional to q, causes an increase in P. The diffusion term dampens P. The last term in Eq. (4.10a) and the first term in Eq. (4.10b) is the pressure energy flux that transfers energy between the potential energy and the turbulent flow energy. The first viscosity term in Eq. (4.10b), $\nu\langle \overline{\Omega^2} \rangle$, suppresses N, while the two last terms are equal to $-\dot{F}$. The last term in Eq. (4.10b) and the first term in Eq. (4.10c) derive from the Reynolds stress, $\overline{\tilde{v}_x \tilde{v}_y}$. The Reynolds stress is generated by the turbulent flow and drives the zonal flow. The last term in Eq. (4.10c) dampens the zonal flow energy due to viscosity.

4.4 Identification of transition dynamics for the unperturbed model

This section considers simulation data from the convection model with $\tau = 0$. As shown in Fig. 3.23, the simulation data transitions between four qualitatively different types of solutions when q varies in $[0, 10]$. We identify the governing system by modeling the four states of the system stepwise to progressively include more complicated dynamics in the model. We restrict the candidate polynomials of the model to be up to second order. It is observed that the inclusion of third order polynomials fails to improve the model further.

4.4.1 Modeling the s-state

When $q < q_{\mathrm{tc1}}$, the solution converges to the static equilibrium, where $P > 0$, $N = F = 0$. In the s-state, $\boldsymbol{v} = 0$ and $\Omega = 0$, and the Reynolds decomposition (3.16) of the convection model reduces to

$$\partial_t \bar{p} = S + \kappa \partial_{xx}^2 \bar{p}.$$

Hence, the time-derivative of $P = \langle x\bar{p} \rangle$ is

$$\dot{P} = \langle xS \rangle + \kappa \langle x \partial_{xx}^2 \bar{p} \rangle.$$

Assuming $\partial_{xx}^2 \bar{p}$ is proportional to $\bar{p}$, we expect $\dot{P}$ to depend linearly on P and q.

We apply the SINDy algorithm to identify the governing equation for the time evolution of P. For this we use simulation data generated by solving Eq. (3.4) for $q \in \{0.0, 0.1, \ldots, 2.9\}$ such that the data includes 30 time series of $P(t)$ and $\dot{P}(t)$ at increasing q-values. We choose as candidate functions a linear function of q, and first and second order polynomial terms of P:

$$\boldsymbol{\Theta}(\boldsymbol{q}, \boldsymbol{P}) = \begin{bmatrix} \boldsymbol{q} & \boldsymbol{P} & \boldsymbol{P}^2 \end{bmatrix}.$$

From the simulation data, SINDy identifies the following sparse model:

$$\dot{P} = rq - \chi P, \tag{4.11}$$

with $r = 4.311 \times 10^{-2}$ and $\chi = 0.1031$. Comparing Eq. (4.11) with Eq. (3.4c), we see that the first term on the right-hand side of Eq. (4.11) derives from the source term S and the second term derives from the diffusion term, $\kappa \nabla_\perp^2 p$. The model (4.11) has the unique equilibrium point

$$P_s = \frac{r}{\chi} q.$$

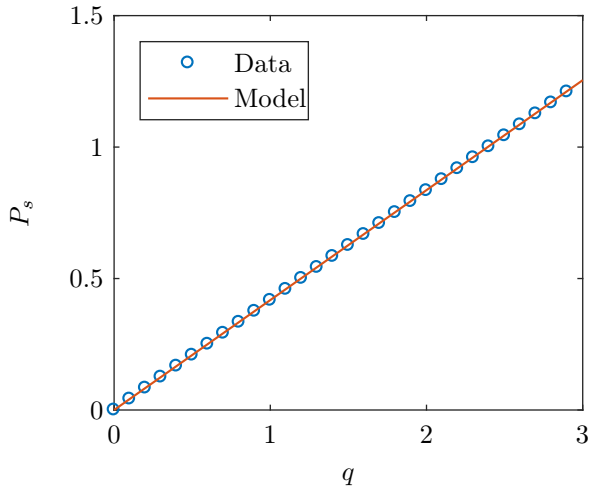

Figure 4.3. The static equilibrium value P_s as a function of q for the data (circles) and the model (solid line).

The plot in Fig. 4.3 compares the values of P_s as a function of q for the simulation data and the model. The position of the s-equilibrium is accurately described by the model. Figure 4.4 shows comparisons of the time series data for P and solutions to the model (4.11) with initial condition $P(0) = 0$ for three different values of q. Figure 4.5 shows the corresponding comparisons of the time-derivative $\dot{P}$. The model solutions approximate the dynamics of the simulation data sufficiently well that we will be using this model to describe the s-state.

4.4.2 Modeling the L-state

When $q_{\mathrm{tc1}} < q < q_{\mathrm{tc2}}$, the solution converges to the L-equilibrium, where $P, N > 0$ and $F = 0$. We apply the SINDy method to identify the underlying system for the time evolution of P and N. For this we use simulation data for $q = \{0.0, 0.1, \ldots, 6.2\}$. We restrict the equations for $\dot{P}$ and $\dot{N}$ to be up to second order polynomials:

$$\boldsymbol{\Theta}(\boldsymbol{q}, \boldsymbol{P}, \boldsymbol{N}) = \begin{bmatrix} \boldsymbol{q} & \boldsymbol{P} & \boldsymbol{N} & \boldsymbol{P}^2 & \boldsymbol{PN} & \boldsymbol{N}^2 \end{bmatrix}.$$

To pass on the parameter values determined, we model $\dot{P} - rq + \chi P$ with the values of r and χ determined in Section 4.4.1.

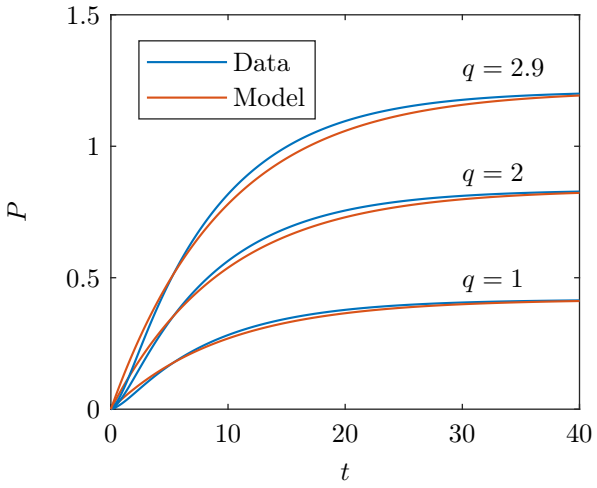

Figure 4.4. The time evolution of P as given by the simulation data and as described by the model for three different values of q.

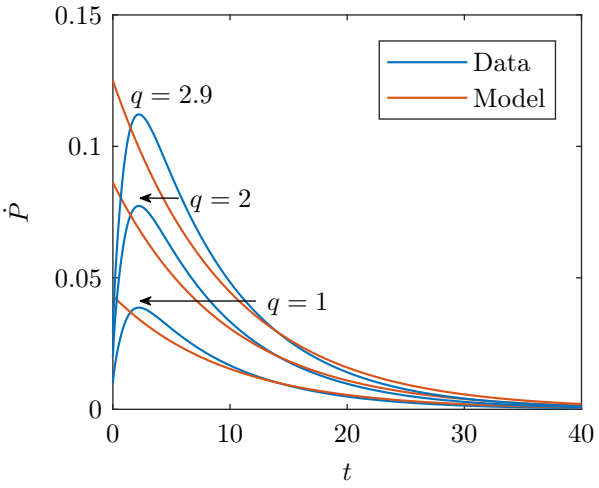

Figure 4.5. The time evolution of $\dot{P}$ as given by the simulation data and as described by the model for three different values of q.

With these settings, the SINDy algorithm identifies the following model:

$$\dot{P} = rq - \chi P - \eta_1 N - \eta_2 N^2 + \eta_3 NP, \tag{4.12a}$$

$$\dot{N} = N(\gamma P - \beta_1 - \beta_2 N) \tag{4.12b}$$

with $r = 4.311 \times 10^{-2}$, $\chi = 0.1031$, $\eta_1 = 7.317$, $\eta_2 = 41.13$, $\eta_3 = 4.700$, $\gamma = 1.953$, $\beta_1 = 2.422$, $\beta_2 = 17.72$. The model (4.12) for the L-state reduces to the model (4.11) for the s-state when $N = 0$ as intended. In Eq. (4.12a), three additional terms have been added when compared with Eq. (4.11).

When the L-equilibrium becomes stable and N converges to the positive value N_L, then P converges to P_L, which is smaller than P_s. So the fluctuating energy N causes a decrease in P. This effect is modeled by the two terms with coefficients η_1 and η_2. When N initially begins to increase, the value of P also increases temporarily, resulting in a little bump on the curve of $P(t)$. This effect is described by the term with coefficient η_3.

Equation (4.12b) describes the evolution of the fluctuation energy N. When the pressure gradient becomes sufficiently steep, the constant profile characterizing the s-solution becomes unstable and a fluctuating flow is generated. This effect is modeled in Eq. (4.12b) by the term with coefficient γ. Dissipation causes the fluctuation energy N to be self-damped. This is described by the terms with coefficients β_1 and β_2.

The L-equilibrium becomes stable at a transcritical bifurcation at $q_{\mathrm{tc1}} = \beta_1\chi/(\gamma r) = 2.967$, which is close to the data-derived value of $q_{\mathrm{tc1}} \approx 2.92$. The plots in Fig. 4.6 compare P_L and N_L as functions of q for the simulation data and the model. The model approximates the position of the L-equilibrium well.

Figure 4.7 shows comparisons of the simulation data and solutions to the model (4.12) for three different values of q. As initial conditions for system (4.12), we used $P(0) = 0$, while $N(0)$ was chosen to make the initial increase in N fit the corresponding simulation data: $N(0) = 1 \times 10^{-9}$ for $q = 4$, $N(0) = 2 \times 10^{-11}$ for $q = 5$, and $N(0) = 2.5 \times 10^{-12}$ for $q = 6$. The plots in Fig. 4.7 show that the small bump in the curve of $P(t)$ created by the sudden increase in $N(t)$ is captured by the model. The fast increase in N and the subsequent monotonic decrease to the equilibrium value N_L is also contained in the model.

Since the model captures the position of the L-equilibrium and approximately reproduces the time series data quantitatively correct, we will use this model to describe the L-state.

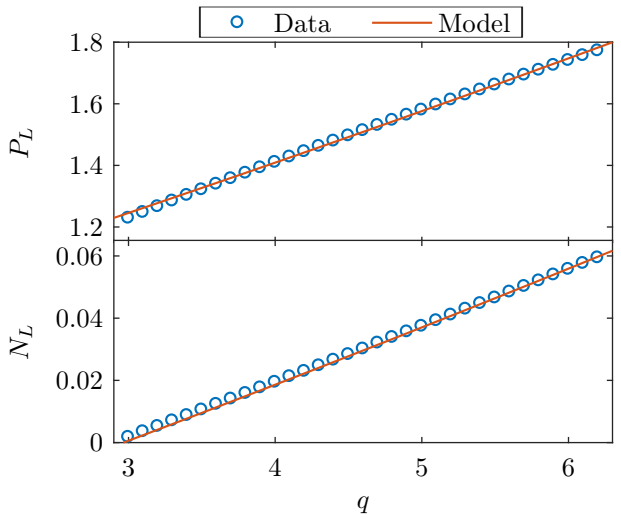

Figure 4.6. P_L (top) and N_L (bottom) as functions of q for the data (circles) and the model (solid lines).

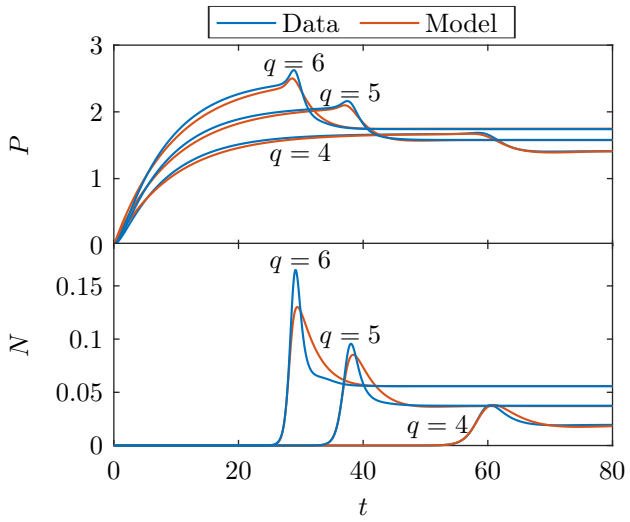

Figure 4.7. Comparisons of the time evolution of P (top) and N (bottom) as given by the simulation data and for the model solution for different values of q.

4.4.3 Modeling the H-state and the limit cycle state

When $q_{\mathrm{tc2}} < q < q_{\mathrm{H}}$, the solution converges to the H-equilibrium, where $P, N, F > 0$. For $q > q_{\mathrm{H}}$, the H-equilibrium is unstable and the solution converges to a limit cycle.

We apply SINDy to identify the governing equations for both of these states simultaneously. The system is identified in the space of polynomials (P, N, F) up to the second order:

$$\boldsymbol{\Theta}(\boldsymbol{q}, \boldsymbol{P}, \boldsymbol{N}, \boldsymbol{F}) = \begin{bmatrix} \boldsymbol{q} & \boldsymbol{P} & \boldsymbol{N} & \boldsymbol{F} & \boldsymbol{P}^2 & \boldsymbol{PN} & \cdots & \boldsymbol{F}^2 \end{bmatrix}.$$

We again restrict the model to contain the previously found terms, i.e., instead of identifying equations for $\dot{P}$ and $\dot{N}$ directly, we identify equations for $\dot{P} - rq + \chi P + \eta_1 N + \eta_2 N^2 - \eta_3 NP$ and $\dot{N} - N(\gamma P - \beta_1 - \beta_2 N)$ with the previously determined coefficients.

In this case, SINDy identifies different models depending on which values of q we include data for. This indicates that the dynamics can not be accurately described in terms of the candidate polynomials. In the data-based bifurcation diagram in Fig. 3.23, we see that when the H-equilibrium is stable, P_H and F_H are increasing as functions of q, while N_H is slightly decreasing as a function of q.

When including data for $q \in \{0.0, 0.1, \ldots, 9.2\}$, SINDy identifies the equation for the time evolution of F as $\dot{F} = F(\alpha_2 N - \mu)$. This expression makes $N_H = \mu/\alpha_2$ independent of q. When including data for $q \in \{0.0, 0.1, \ldots, 10.0\}$, SINDy identifies the equation for the time evolution of F as $\dot{F} = F(\alpha_2 N - \mu P)$. This gives a linear relationship between N_H and P_H, and both P_H and N_H are increasing as functions of q.

None of these expressions describe the N_H-dependency of q qualitatively correct. However, the first expression for $\dot{F}$ approximates the behavior better than the second expression, so we retain that. For the equations for $\dot{P}$ and $\dot{N}$, we use the result obtained when including data for $q \in \{0.0, 0.1, \ldots, 10.0\}$. This results in the model

$$\begin{aligned} \dot{P} &= rq - \chi P - \eta_1 N - \eta_2 N^2 + \eta_3 PN \\ &\quad - \varphi_1 F - \varphi_2 F^2 + \varphi_3 PF, \end{aligned} \tag{4.13a}$$

$$\dot{N} = N(\gamma P - \beta_1 - \beta_2 N - \alpha_1 F), \tag{4.13b}$$

$$\dot{F} = F(\alpha_2 N - \mu). \tag{4.13c}$$

The coefficients identified by SINDy result in a poor approximation of the position of the H-equilibrium as a function of q. Instead, the ratio μ/α_2 is chosen

r	χ	η_1	η_2	η_3	γ	β_1
4.311×10^{-2}	0.1031	7.317	41.13	4.700	1.953	2.422
β_2	φ_1	φ_2	φ_3	α_1	α_2	μ
17.72	70.50	1151	34.12	63.32	33.00	2.023

Table 4.3. The parameter values for the system (4.13). $q \in [0, 10]$ is a bifurcation parameter.

to reproduce the data-derived value of q_{tc2} in the model. The value of α_1 is determined by a linear fit to a plot of $\gamma P_H - \beta_1 - \beta_2 N_H$ as a function of F_H. The value of α_2 is chosen to approximately reproduce the frequency of the oscillations. Finally, φ_1, φ_2, and φ_3 are computed to obtain the best possible approximation of F_H as a function of q and to reproduce the data-derived value of q_{H} in the model. Table 4.3 lists the parameter values for system (4.13).

In Eq. (4.13a), the zonal flow energy enters into the equation for $\dot{P}$ similarly to the turbulent flow. In Eq. (4.13b), the zonal flow suppresses the turbulent flow and in Eq. (4.13c), the turbulent flow drives the zonal flow. This predator-prey type coupling between the zonal flow and the turbulent flow is attributable to the Reynolds stress. The zonal flow energy is linearly self-damping due to the viscocity term. Near the H-equilibrium the zonal flow dampens P, but the zonal flow also dampens N, which causes a decrease in the damping of P, so the overall effect is that P increases when F increases.

The plots in Fig. 4.8 compare P_H, N_H, and F_H as functions of q for the simulation data and the model. The model approximates the value of F_H accurately, since the parameter values were chosen to obtain the best possible fit of F_H as a function of q for the model. The model also approximates P_H and N_H within a small relative error.

The plots in Figs. 4.9–4.12 compare the simulation data and the model solutions for $q = 7$, $q = 8$, $q = 9$, and $q = 10$, respectively. The initial conditions were chosen such that N and F begins to increase at about the same time as in the corresponding data.

For $q = 7$, the initial condition for the model solution shown in Fig. 4.9 was $(P(0), N(0), F(0)) = (0, 1 \times 10^{-12}, 1 \times 10^{-28})$. For the model solution, F increases a little faster than the corresponding data, but otherwise the model solution approximates the data very well both qualitatively and quantitatively.

For $q = 8$, the initial condition for the model solution shown in Fig. 4.10 was $(P(0), N(0), F(0)) = (0, 1 \times 10^{-12}, 1 \times 10^{-38})$. The solution spirals into

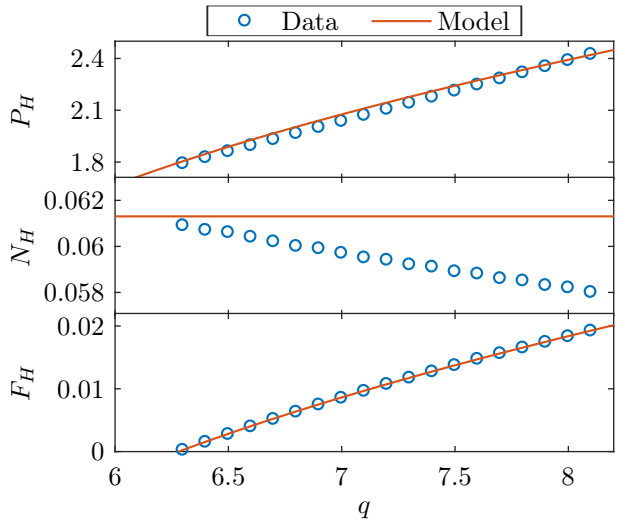

Figure 4.8. P_H (top), N_H (middle), and F_H (bottom) as functions of q for the data (circles) and the model (solid lines).

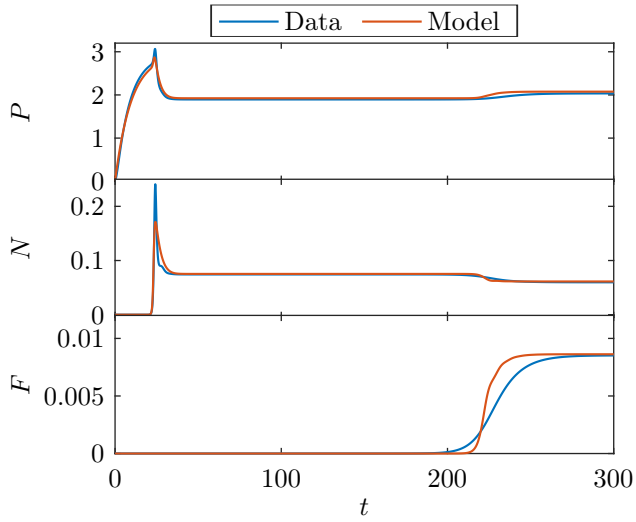

Figure 4.9. Comparison of the time evolution of P (top), N (middle), and F (bottom) for the simulation data and for the model solution for $q = 7$.

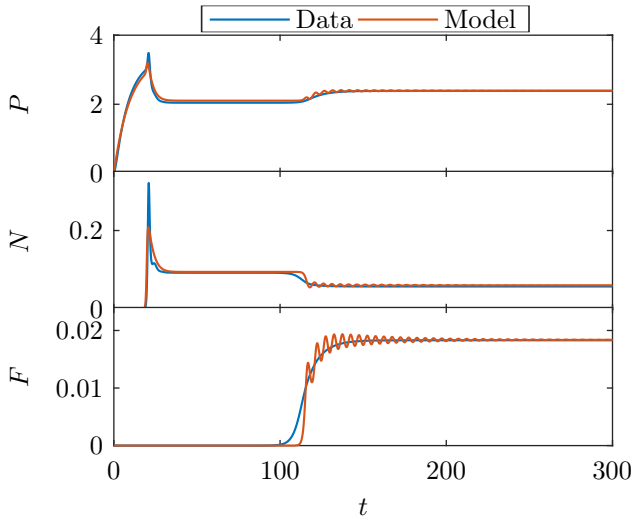

Figure 4.10. Comparison of the time evolution of P (top), N (middle), and F (bottom) for the simulation data and for the model solution for $q = 8$.

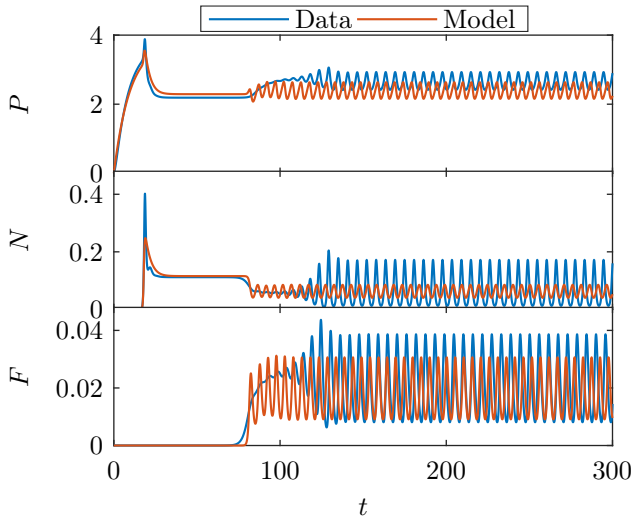

Figure 4.11. Comparison of the time evolution of P (top), N (middle), and F (bottom) for the simulation data and for the model solution for $q = 9$.

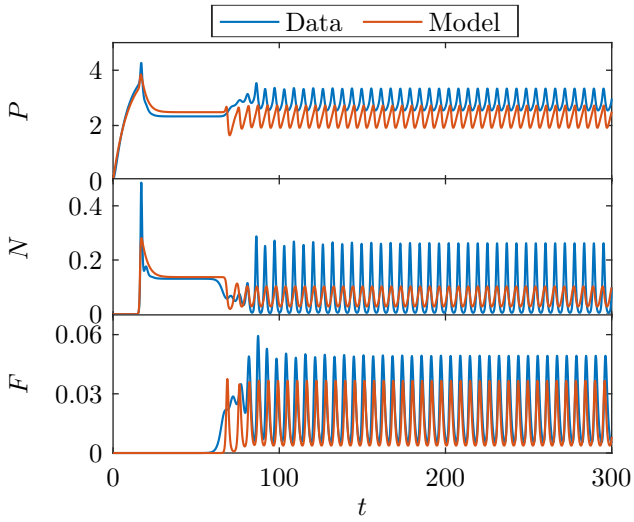

Figure 4.12. Comparison of the time evolution of P (top), N (middle), and F (bottom) for the simulation data and for the model solution for $q = 10$.

the H-equilibrium, while the corresponding data approaches the H-equilibrium monotonically. Otherwise the model solution approximates the data very well.

For $q = 9$, the initial condition for the model solution shown in Fig. 4.11 was $(P(0), N(0), F(0)) = (0, 1 \times 10^{-13}, 1 \times 10^{-44})$. The solution converges to a stable limit cycle like the data. The model fails to reproduce the amplitude and frequency of the oscillations.

For $q = 10$, the initial condition for the model solution shown in Fig. 4.12 was $(P(0), N(0), F(0)) = (0, 1 \times 10^{-13}, 1 \times 10^{-53})$. The model solution still converges to a stable limit cycle like the data. The model solution now correctly reproduces the frequency of the oscillations, but it fails to reproduce the amplitude of the oscillations. The mean value of P during the oscillations is lower for the model solution than for the data. This might indicate that we are approaching the maximum value of q for which the model is valid. The failure to reproduce the correct amplitude of the oscillations is expected, since amplitude fitting was not chosen as a criterion during the modeling process.

Overall, the final model (4.13) reproduces the simulation data very well both qualitatively and quantitatively for $q \in [0, 10]$.

4.5 Bifurcation analysis

Using the SINDy algorithm, we have derived the model (4.13) with the parameters listed in Table 4.3 for the time evolution of the three energies P, N, F computed from solutions to the convection problem (3.4). We now carry out a bifurcation analysis for the model (4.13) and summarize the results in a bifurcation diagram.

4.5.1 Equilibrium points

Nullclines are the surfaces in state-space on which a single component of the vector field defining a dynamical system vanishes. The nullclines of the system (4.13) are given by

$$\begin{aligned}
\mathcal{N}_P &= \{rq = \chi P + \eta_1 N + \eta_2 N^2 - \eta_3 PN + \varphi_1 F + \varphi_2 F^2 - \varphi_3 PF\},\\
\mathcal{N}_N &= \{N = 0\} \cup \{\gamma P = \beta_1 + \beta_2 N + \alpha_1 F\},\\
\mathcal{N}_F &= \{F = 0\} \cup \{\alpha_2 N = \mu\}.
\end{aligned}$$

We note that $\{N = 0\}$ and $\{F = 0\}$ are invariant manifolds of the system. This prevent N and F from becoming negative when they are initialized as being strictly positive. However, the model does not generally prevent P from becoming negative. The intersections of all three nullclines gives the equilibrium points. The system has a total of five equilibrium points, but we list and name only the three equilibrium points which are stable for some value of $q \in [0, 10]$. The s-equilibrium is

$$(P_s, N_s, F_s) = \left(\frac{r}{\chi}q, 0, 0\right), \qquad q > 0. \tag{4.14}$$

The L-equilibrium enters the physical domain in a transcritical bifurcation at $q = q_{\text{tc1}} = \beta_1\chi/(\gamma r)$. Define

$$\begin{aligned}
a_{P_L} &= \gamma(\beta_2\eta_3 - \gamma\eta_2),\\
b_{P_L} &= -(\beta_1\beta_2\eta_3 + \beta_2^2\chi + \beta_2\gamma\eta_1 - 2\beta_1\gamma\eta_2),\\
c_{P_L} &= \beta_2^2 rq + \beta_1\beta_2\eta_1 - \beta_1^2\eta_2
\end{aligned}$$

and

$$\begin{aligned}
a_{N_L} &= \beta_2\eta_3 - \gamma\eta_2,\\
b_{N_L} &= -(\beta_2\chi + \gamma\eta_1 - \beta_1\eta_3),\\
c_{N_L} &= \gamma rq - \beta_1\chi.
\end{aligned}$$

Then, the components of the L-equilibrium (P_L, N_L, F_L), $q > q_{\mathrm{tc1}}$ are

$$P_L = \frac{1}{2a_{P_L}} \left(-b_{P_L} - \sqrt{b_{P_L}^2 - 4a_{P_L} c_{P_L}} \right), \tag{4.15a}$$

$$N_L = \frac{1}{2a_{N_L}} \left(-b_{N_L} - \sqrt{b_{N_L}^2 - 4a_{N_L} c_{N_L}} \right), \tag{4.15b}$$

$$F_L = 0. \tag{4.15c}$$

The H-equilibrium enters the physical domain in a transcritical bifurcation at $q = q_{\mathrm{tc2}}$, where

$$q_{\mathrm{tc2}} = \frac{1}{\gamma r} \left(\beta_1 \chi - b_{N_L} \frac{\mu}{\alpha_2} - a_{N_L} \frac{\mu^2}{\alpha_2^2} \right).$$

We define

$$\begin{aligned}
a_{P_H} &= \alpha_2^2 \gamma (\gamma \varphi_2 - \alpha_1 \varphi_3), \\
b_{P_H} &= -\alpha_2 \big(\alpha_1^2 \eta_3 \mu - \alpha_1^2 \alpha_2 \chi - \alpha_1 \alpha_2 \beta_1 \varphi_3 - \alpha_1 \alpha_2 \gamma \varphi_1 \\
&\quad - \alpha_1 \beta_2 \mu \varphi_3 + 2\alpha_2 \beta_1 \gamma \varphi_2 + 2\beta_2 \gamma \mu \varphi_2 \big), \\
c_{P_H} &= -(\alpha_1^2 \alpha_2^2 r q - \alpha_1^2 \alpha_2 \eta_1 \mu - \alpha_1^2 \eta_2 \mu^2 + \alpha_1 \alpha_2^2 \beta_1 \varphi_1 \\
&\quad + \alpha_1 \alpha_2 \beta_2 \mu \varphi_1 - \alpha_2^2 \beta_1^2 \varphi_2 - 2\alpha_2 \beta_1 \beta_2 \mu \varphi_2 - \beta_2^2 \mu^2 \varphi_2)
\end{aligned}$$

and

$$\begin{aligned}
a_{F_H} &= \alpha_2^2 (\gamma \varphi_2 - \alpha_1 \varphi_3), \\
b_{F_H} &= \alpha_2 (\alpha_1 \alpha_2 \chi - \alpha_1 \eta_3 \mu - \alpha_2 \beta_1 \varphi_3 + \alpha_2 \gamma \varphi_1 - \beta_2 \mu \varphi_3), \\
c_{F_H} &= -\big(\alpha_2^2 \gamma r q - \alpha_2^2 \beta_1 \chi + \alpha_2 \beta_1 \eta_3 \mu - \alpha_2 \beta_2 \chi \mu - \alpha_2 \eta_1 \gamma \mu + \beta_2 \eta_3 \mu^2 - \eta_2 \gamma \mu^2 \big).
\end{aligned}$$

Then, the H-equilibrium can be written as (P_H, N_H, F_H), $q > q_{\mathrm{tc2}}$ with

$$P_H = \frac{1}{2a_{P_H}} \left(-b_{P_H} + \sqrt{b_{P_H}^2 - 4a_{P_H} c_{P_H}} \right), \tag{4.16a}$$

$$N_H = \frac{\mu}{\alpha_2}, \tag{4.16b}$$

$$F_H = \frac{1}{2a_{F_H}} \left(-b_{F_H} + \sqrt{b_{F_H}^2 - 4a_{F_H} c_{F_H}} \right). \tag{4.16c}$$

Figure 4.13 shows a plot of the three nullclines for $q = 10$ within a rectangular cuboid region of the phase space. At the intersections of all three nullclines are shown the s-, L-, and H-equilibrium points. For this value of q, all three equilibrium points are unstable and the solution converges to the limit cycle.

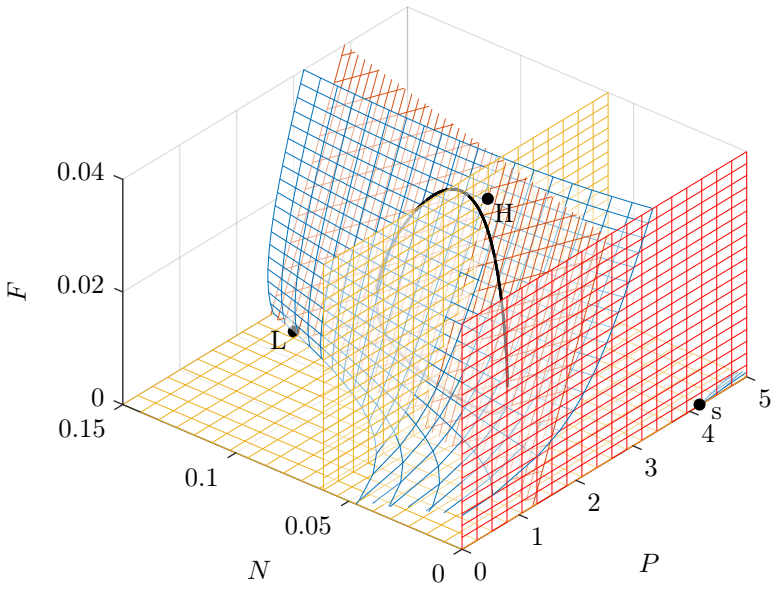

Figure 4.13. The nullclines for $q = 10$: $\mathcal{N}_P$ is blue, $\mathcal{N}_N$ is red, and $\mathcal{N}_F$ is yellow. Only $\mathcal{N}_P$ depend on q. The positions of the s-, L-, and H-equilibrium are marked at the intersection points of all three nullclines. The black closed curve is the stable limit cycle.

4.5.2 Stability of equilibrium points

The stability type of the equilibrium points are determined by the eigenvalues of the Jacobian matrix of system (4.13) evaluated at the equilibrium point. The Jacobian matrix in a general point is

$$\mathcal{D}f = \begin{pmatrix} -\chi + \eta_3 N + \varphi_3 F & -\eta_1 - 2\eta_2 N + \eta_3 P & -\varphi_1 - 2\varphi_2 F + \varphi_3 P \\ \gamma N & \gamma P - \beta_1 - 2\beta_2 N - \alpha_1 F & -\alpha_1 N \\ 0 & \alpha_2 F & \alpha_2 N - \mu \end{pmatrix}. \tag{4.17}$$

We will here determine the stability of each of the three equilibrium points sequentially.

4.5.2.1 Stability of the s-equilibrium

The Jacobian matrix (4.17) evaluated at the static equilibrium is

$$\boldsymbol{A}_s = \begin{pmatrix} -\chi & -\eta_1 + \eta_3 P_s & -\varphi_1 + \varphi_3 P_s \\ 0 & \frac{\gamma r}{\chi} q - \beta_1 & 0 \\ 0 & 0 & -\mu \end{pmatrix}.$$

This is a upper triangular matrix, so the eigenvalues are given by the diagonal elements

$$\lambda_1 = -\chi, \qquad \lambda_2 = \frac{\gamma r}{\chi} q - \beta_1, \qquad \lambda_3 = -\mu.$$

All three eigenvalues are real. Figure 4.14 shows a plot of the three eigenvalues as functions of q. λ_1 and λ_3 are negative constants, while λ_2 is negative for $q < q_{\mathrm{tc1}}$ and positive for $q > q_{\mathrm{tc1}}$. Consequently, the s-equilibrium is a stable node for $q < q_{\mathrm{tc1}}$ and a saddle for $q > q_{\mathrm{tc1}}$.

4.5.2.2 Stability of the L-equilibrium

The Jacobian matrix (4.17) evaluated at the L-equilibrium is

$$\boldsymbol{A}_L = \begin{pmatrix} -\chi + \eta_3 N_L & -\eta_1 - 2\eta_2 N_L + \eta_3 P_L & -\varphi_1 + \varphi_3 P_L \\ \gamma N_L & -\beta_2 N_L & -\alpha_1 N_L \\ 0 & 0 & \alpha_2 N_L - \mu \end{pmatrix}.$$

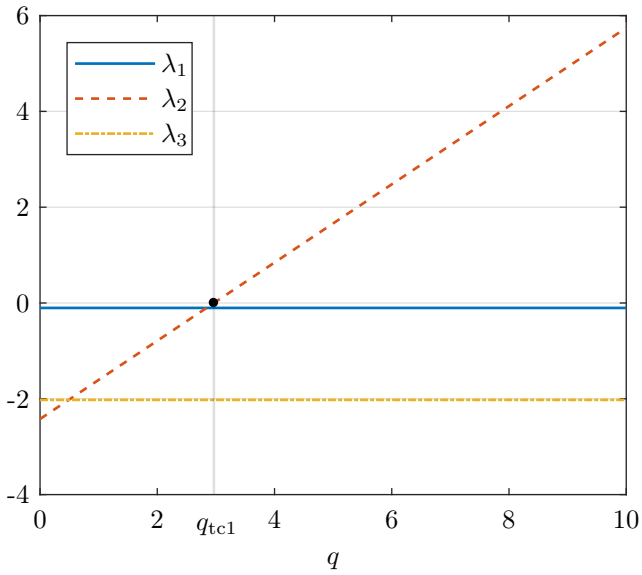

Figure 4.14. The eigenvalues of $\boldsymbol{A}_s$ as functions of q. λ_2 changes sign at $q = q_{\mathrm{tc1}}$, while λ_1 and λ_3 are negative constants.

Define

$$b_L = \beta_2 N_L + \chi - \eta_3 N_L,$$
$$c_L = -N_L((\beta_2\eta_3 - 2\gamma\eta_2)N_L + \gamma\eta_3 P_L - \beta_2\chi - \gamma\eta_1).$$

Then, the eigenvalues of $\boldsymbol{A}_L$ are

$$\lambda_1 = -\frac{1}{2}\left(b_L - \sqrt{b_L^2 - 4c_L}\right),$$
$$\lambda_2 = -\frac{1}{2}\left(b_L + \sqrt{b_L^2 - 4c_L}\right),$$
$$\lambda_3 = \alpha_2 N_L - \mu.$$

Figure 4.15 shows a plot of the real and imaginary parts of the eigenvalues of $\boldsymbol{A}_L$. $\mathrm{Re}(\lambda_1)$ is positive for $q < q_{\mathrm{tc1}}$ and negative for $q > q_{\mathrm{tc1}}$, $\mathrm{Re}(\lambda_2)$ is negative for all q. $\mathrm{Re}(\lambda_3)$ is negative for $q < q_{\mathrm{tc2}}$ and positive for $q > q_{\mathrm{tc2}}$. consequently, the L-equilibrium is a saddle for $q < q_{\mathrm{tc1}}$, it is a stable node or focus-node for $q_{\mathrm{tc1}} < q < q_{\mathrm{tc2}}$, and an unstable saddle-focus or node for $q > q_{\mathrm{tc2}}$.

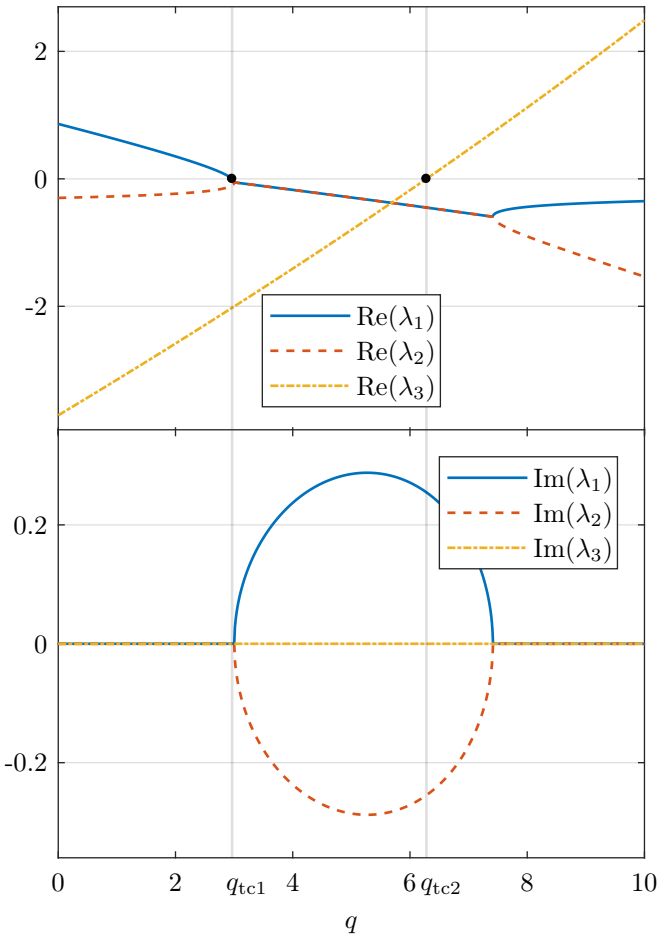

Figure 4.15. The real part (top) and the imaginary part (bottom) of the eigenvalues of $\boldsymbol{A}_L$ as functions of q. $\mathrm{Re}(\lambda_1)$ changes sign at $q = q_{\mathrm{tc}1}$, λ_3 changes sign at $q = q_{\mathrm{tc}2}$, while $\mathrm{Re}(\lambda_2)$ is negative everywhere.

4.5.2.3 Stability of the H-equilibrium

The Jacobian matrix (4.17) evaluated at the H-equilibrium is

$$\boldsymbol{A}_H = \begin{pmatrix} -\chi + \eta_3 N_H + \varphi_3 F_H & -\eta_1 - 2\eta_2 N_H + \eta_3 P_H & -\varphi_1 - 2\varphi_2 F_H + \varphi_3 P_H \\ \gamma N_H & -\beta_2 N_H & -\alpha_1 N_H \\ 0 & \alpha_2 F_H & 0 \end{pmatrix}.$$

Let $\tau = \mathrm{tr}(\boldsymbol{A}_H)$ be the trace, σ the sum of principal minors, and $\delta = \det(\boldsymbol{A}_H)$ the determinant of $\boldsymbol{A}_H$,

$$\begin{aligned} \tau &= -\chi + \eta_3 N_H + \varphi_3 F_H - \beta_2 N_H, \\ \sigma &= N_H(\alpha_1\alpha_2 F_H + \beta_2\chi - \beta_2\eta_3 N_H - \beta_2\varphi_3 F_H + \gamma\eta_1 + 2\gamma\eta_2 N_H - \gamma\eta_3 P_H), \\ \delta &= \alpha_2 N_H F_H(-\alpha_1\chi + \alpha_1\eta_3 N_H + \alpha_1\varphi_3 F_H - \gamma\varphi_1 - 2\gamma\varphi_2 F_H + \gamma\varphi_3 P_H). \end{aligned}$$

Then the characteristic polynomial is given by

$$p(\lambda) = \lambda^3 - \tau\lambda^2 + \sigma\lambda - \delta.$$

The eigenvalues are obtained as the three complex solutions to $p(\lambda) = 0$. Figure 4.16 shows plots of the real and imaginary parts of the eigenvalues of $\boldsymbol{A}_H$ as functions of q. Inserting $\lambda = i\omega$ and solving $p(i\omega) = 0$ shows that a Hopf bifurcation occurs when $\sigma\tau = \delta$. By numerically solving this equation for q we obtain $q_{\mathrm{H}} = 8.152$. The eigenvalue λ_1 is positive for $q < q_{\mathrm{tc2}}$ and negative for $q > q_{\mathrm{tc2}}$. $\mathrm{Re}(\lambda_2)$ and $\mathrm{Re}(\lambda_3)$ are negative for $q < q_{\mathrm{H}}$ and positive for $q > q_{\mathrm{H}}$. consequently, the H-equilibrium is a saddle or a saddle-focus for $q < q_{\mathrm{tc2}}$, it is a stable focus-node for $q_{\mathrm{tc2}} < q < q_{\mathrm{H}}$, and it is a saddle-focus for $q > q_{\mathrm{H}}$.

4.5.3 Bifurcation diagram

The positions and the stability of the equilibrium points for system (4.13) as functions of q are summarized in the bifurcation diagram in Fig. 4.17. A comparison of the bifurcation diagram for the model with the data-based bifurcation diagram in Fig. 3.23, demonstrates that the model approximates the positions of the three equilibrium points and three bifurcation points very well. The average position and amplitude of the limit cycle oscillations differ between the two bifurcation diagrams, but these were not expected to be fully identical.

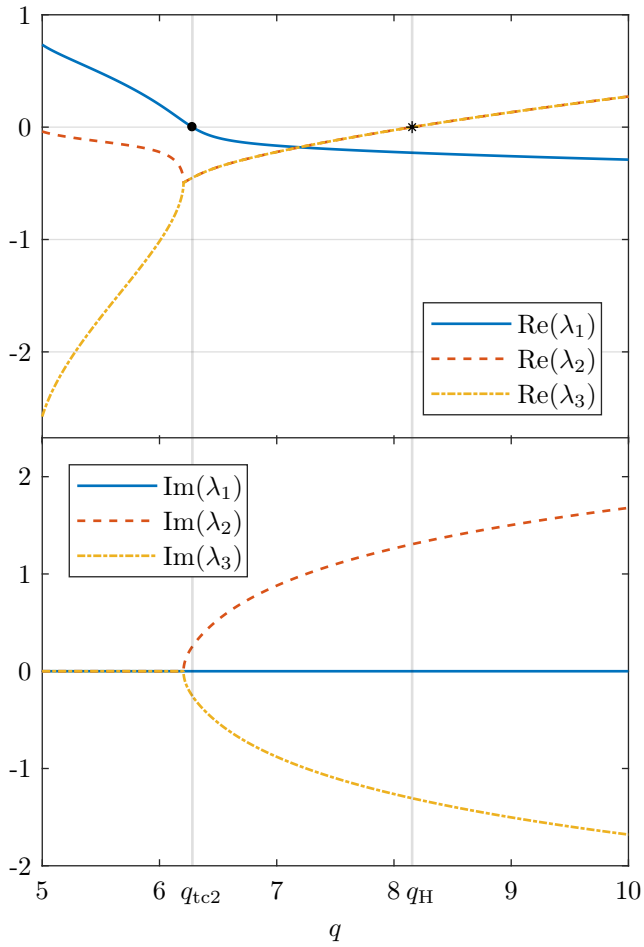

Figure 4.16. The real part (top) and the imaginary part (bottom) of the eigenvalues of $\boldsymbol{A}_H$. $\mathrm{Re}(\lambda_1)$ is positive for $q < q_{tc2}$ and negative for $q > q_{tc2}$. $\mathrm{Re}(\lambda_2)$ and $\mathrm{Re}(\lambda_3)$ are negative for $q < q_H$ and positive for $q > q_H$.

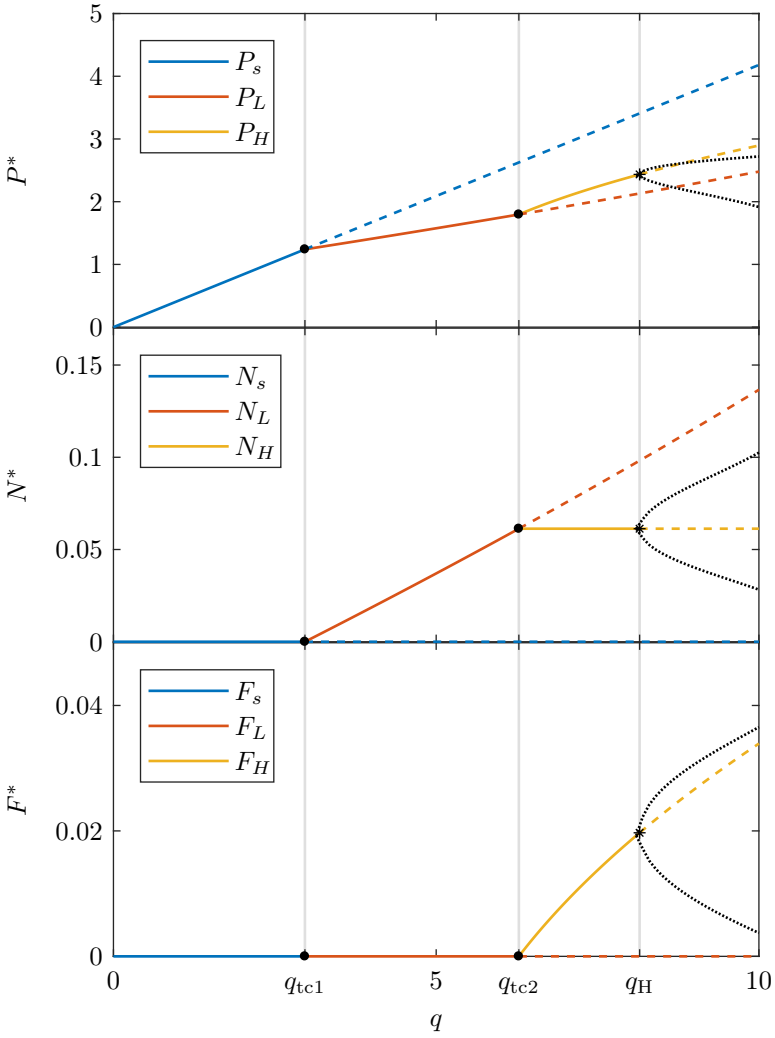

Figure 4.17. Bifurcation diagram for the model. Solid curves are stable equilibrium points, dashed curves are unstable equilibrium points, while the dotted curve show the amplitude of the limit cycle solution. The transcritical bifurcations occurring at approximately $q_{tc1} = 2.967$ and $q_{tc2} = 6.281$ are marked with dots, while the Hopf bifurcation occurring at $q_H = 8.152$ is marked with asterisks.

4.6 Identification of transition dynamics for the perturbed model

This section considers simulation data from the convection model with $\tau = 0.04$. As shown in Fig. 3.24 the simulation data transitions between four qualitatively different types of solutions when q varies in $[0, 24]$. Unlike the $\tau = 0$ case, for some ranges of q the system has two stable states, and which of these states the solution converges to depends on the initial conditions.

We attempt to identify the governing system by modeling the four states of the system stepwise to progressively include more complicated dynamics in the model. However, we only succeed in modeling the static state. The quality of the model is determined by visually comparing how well the model describes the position of equilibrium points and how well solutions to the model reproduce the simulated time series data.

4.6.1 Modeling the s-state

When $q < q_{\text{tc1}}$, the solution converges to the s-equilibrium, where $P, N > 0$ and $N = 0$. In the s-state, $v_x = 0$ and $\omega = 0$, and the Reynolds decomposition (3.16) of the convection model reduces to

$$\partial_t \bar{p} = S + \kappa \partial_{xx}^2 \bar{p}, \tag{4.18a}$$

$$\bar{v}_y = -\tau \partial_x \bar{p}. \tag{4.18b}$$

Hence, the time derivative of $\bar{v}_y$ is

$$\begin{aligned} \partial_t \bar{v}_y &= -\tau \partial_x \partial_t \bar{p} \\ &= -\tau(\partial_x S + \kappa \partial_{xxx}^3 \bar{p}), \end{aligned}$$

and the time derivative of $\bar{v}_y^2$ is

$$\begin{aligned} \partial_t \bar{v}_y^2 &= 2\bar{v}_y \partial_t \bar{v}_y \\ &= 2\tau^2 \left((\partial_x \bar{p})(\partial_x S) + \kappa (\partial_x \bar{p})(\partial_{xxx}^3 \bar{p}) \right). \end{aligned}$$

Since $P = \langle x\bar{p} \rangle$ and $F = \frac{1}{2}\langle \bar{v}_y^2 \rangle$, the derivatives of P and F are

$$\begin{aligned} \dot{P} &= \langle xS \rangle + \kappa \langle x \partial_{xx}^2 \bar{p} \rangle, \\ \dot{F} &= \tau^2 \langle (\partial_x \bar{p})(\partial_x S) \rangle + \tau^2 \kappa \langle (\partial_x \bar{p})(\partial_{xxx}^3 \bar{p}) \rangle. \end{aligned}$$

r	χ	μ	b_1	b_2	b_3
4.311×10^{-2}	0.1031	0.9401	2.408×10^{-4}	1.250×10^{-3}	2.705×10^{-3}

Table 4.4. The parameter values for the system (4.19). $q \in [0, 3.4]$ is a bifurcation parameter.

This suggest that $\dot{P}$ does not depend on F, and it is appropriate to approximate $\dot{P}$ with first order polynomials of P and q. Assuming the spatial derivatives of $\bar{p}$ are proportional to $\bar{p}$, we should approximate $\dot{F}$ with up to second order polynomials in P, F, and q.

We apply SINDy to identify the governing equations for the time evolution of P and N. We use simulation data for $q \in \{0.0, 0.2, \ldots, 3.4\}$. We choose as candidate functions to be up to second order polynomials in q, P, and F

$$\boldsymbol{\Theta}(\boldsymbol{q}, \boldsymbol{P}, \boldsymbol{F}) = \begin{bmatrix} \boldsymbol{q} & \boldsymbol{P} & \boldsymbol{F} & \boldsymbol{q}^2 & \boldsymbol{qP} & \boldsymbol{qF} & \boldsymbol{P}^2 & \boldsymbol{PF} & \boldsymbol{F}^2 \end{bmatrix}.$$

From the simulation data, SINDy identifies the system

$$\dot{P} = rq - \chi P, \tag{4.19a}$$

$$\dot{F} = -\mu F + b_1 q^2 - b_2 qP + b_3 P^2 \tag{4.19b}$$

with the parameters listed in Table 4.4. The system has the equilibrium point

$$(P_s, N_s, F_s) = \left(\tfrac{r}{\chi} q, 0, \tfrac{1}{\mu}(b_1 - b_2 \tfrac{r}{\chi} + b_3 \tfrac{r^2}{\chi^2}) q^2 \right).$$

Figure 4.18 compares the values of P_s and F_s as functions of q for the simulation data and the model. The position of the s-equilibrium is accurately described by the model.

Figure 4.19 shows comparisons of the time series data for P and F and solutions to the model (4.19) with initial condition $(P(0), F(0)) = (0, 0)$ for three different values of q.

The model solutions approximate the dynamics of the simulation data well. However, in the model (4.19), $\dot{P}$ is independent of F, which is inconsistent with the model (4.13) identified for $\tau = 0$, where $\dot{P}$ depends explicitly on F. This suggests that the model (4.13) needs a modification. The inconsistency could also originate from the choice of state variables: The energy of the flow generated by the pressure curvature might need to be treated separately as a mean flow energy, instead of being included as part of the zonal flow energy.

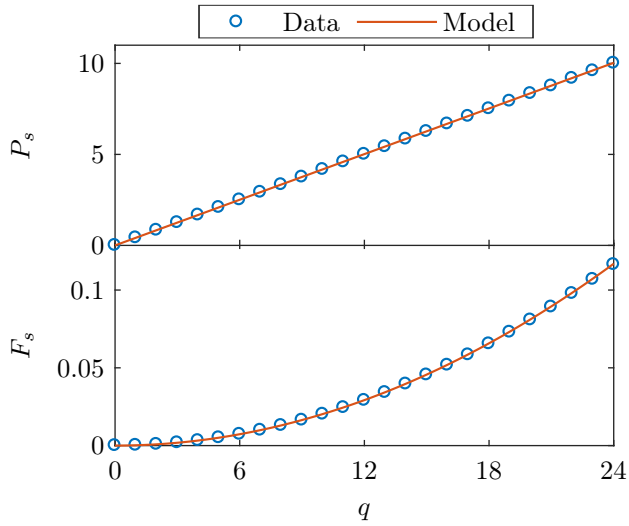

Figure 4.18. The static equilibrium values P_s (top) and F_s (bottom) as functions of q for the data (circles) and the model (solid lines).

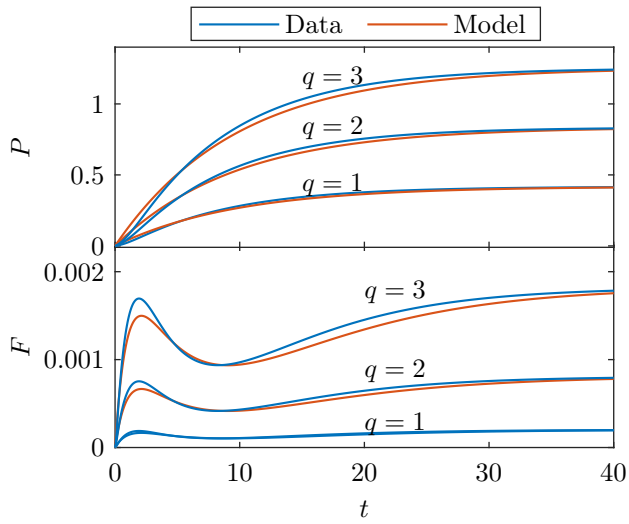

Figure 4.19. The time evolution of P and F as given by the simulation data and by the model for different values of q.

4.6.2 Attempt to model the other states

For $q_{\mathrm{tc1}} < q_{\mathrm{sn1}}$, the L-equilibrium is the only stable equilibrium. However, all three variables are positive in the L-equilibrium, and there are no more additional variables to add new dynamics after this: The model for the L-equilibrium must be the full model. According to the data-based bifurcation diagram in Fig. 3.24, the system has for $q_{\mathrm{sn1}} < q < q_{\mathrm{sn2}}$ four equilibrium points, which should be included in the identified model. We tried unsuccessfully to have SINDy identify a model directly from sets of data.

For $\tau = 0$, we identified the dynamics of the system to be given by Eq. (4.13). Combining the system (4.13) with the system (4.19) gives

$$\dot{P} = rq - \chi P - \eta_1 N - \eta_2 N^2 + \eta_3 NP, \tag{4.20a}$$

$$\dot{N} = N(\gamma P - \beta_1 - \beta_2 N - \alpha_1 F), \tag{4.20b}$$

$$\dot{F} = F(\alpha_2 N - \mu) + b_1 q^2 - b_2 qP + b_3 P^2. \tag{4.20c}$$

Solving this model with the parameter values listed in Tables 4.3–4.4 did not give good approximations to the simulation data. Hence, the perturbation of the vorticity adds a lot more complexity to the system than just an increased zonal flow. More research is needed to determine a system that models the dynamical behavior of P, N, and F when $\tau = 0.04$.

4.7 Conclusion

The solution to a convection problem with a pressure source centered at the left boundary can be characterized by three state variables: the potential energy related to the pressure gradient, P, the fluctuation energy, N, and the zonal flow energy, F. Depending on the strength of the pressure source, q, we identified four different types of solutions to the convection problem. Three of these solution types corresponded to equilibrium points and the fourth type corresponded to a limit cycle in the (P, N, F)-state space. Simulation data was generated for multiple fixed values of $q \in [0, 10]$ by computing and saving the three energy variables P, N, and F and their time derivatives at each output time step while solving the convection problem.

Purely based on the simulation data we used SINDy [17] and some data fitting to identify a nonlinear dynamical system that models the time evolution of the three state variables. This approach revealed a predator-prey relationship between the zonal flow energy and the turbulent flow energy. We investigated the quality of

the model by comparing positions of equilibrium points, bifurcation points, and solutions with the corresponding data from which the model was extracted. The model proved to be very accurate for each of these parameters.

We introduced a perturbation to the vorticity in the convection problem. For the perturbed vorticity convection problem, we attempted to use SINDy to identify the underlying dynamics of the three energy variables P, N, and F. We only succeeded in making a model for the static state.

We have demonstrated an approach to recover reduced models for plasma dynamics, which serves as an alternative to the physical modeling approach. This modeling approach could ultimately also be applied to derive models from experimental data. A model for the convection model with perturbed vorticity might possibly be obtained by replacing the SINDy algorithm with the more advanced implicit-SINDy algorithm [57], which extends SINDy to allow rational functions. By defining the energy state variables differently, a model for the energies of the convection model with perturbed vorticity might also be obtainable with SINDy. More research is needed to identify such a model.

Bibliography

[1] Justin R. Angus, Sergei I. Krasheninnikov, and Maxim V. Umansky. "Effects of parallel electron dynamics on plasma blob transport". In: *Phys. Plasmas* 19.8 (2012), p. 082312. DOI: 10.1063/1.4747619.

[2] Justin R. Angus and Maxim V. Umansky. "Modeling of large amplitude plasma blobs in three-dimensions". In: *Phys. Plasmas* 21.1 (2014), p. 012514. DOI: 10.1063/1.4863503.

[3] A. Y. Aydemir. "Convective transport in the scrape-off layer of tokamaks". In: *Phys. Plasmas* 12.6 (2005), p. 062503. DOI: 10.1063/1.1927539.

[4] P. G. Bakker. *Bifurcations in Flow Patterns*. Vol. 2. Nonlinear Topics in the Mathematical Sciences. Springer Netherlands, 1991. DOI: 10.1007/978-94-011-3512-2.

[5] R. Ball. "Dynamical systems modelling of turbulence-shear flow interactions in magnetized fusion plasmas". In: *Journal of Physics: Conference Series* 7.1 (2005), p. 191. DOI: 10.1088/1742-6596/7/1/016.

[6] R. Ball. "Suppression of turbulence at low power input in a model for plasma confinement transitions". In: *Phys. Plasmas* 12.9, 090904 (2005). DOI: 10.1063/1.2034327.

[7] R. Ball and R. L. Dewar. "Singularity Theory Study of Overdetermination in Models for $L - H$ Transitions". In: *Phys. Rev. Lett.* 84 (14 Apr. 2000), pp. 3077–3080. DOI: 10.1103/PhysRevLett.84.3077.

[8] R. Ball, R. L. Dewar, and H. Sugama. "Metamorphosis of plasma turbulence–shear-flow dynamics through a transcritical bifurcation". In: *Phys. Rev. E* 66 (6 Dec. 2002), p. 066408. DOI: 10.1103/PhysRevE.66.066408.

[9] S. Benkadda et al. "Bursty transport in tokamak turbulence: Role of zonal flows and internal transport barriers". In: *Nucl. Fusion* 41.8 (2001), p. 995. DOI: 10.1088/0029-5515/41/8/304.

[10] N. H. Bian and O. E. Garcia. "Structures, profile consistency, and transport scaling in electrostatic convection". In: *Phys. Plasmas* 12.4, 042307 (2005). DOI: 10.1063/1.1867994.

[11] N. Bian et al. "Blobs and front propagation in the scrape-off layer of magnetic confinement devices". In: *Phys. Plasmas* 10.3 (2003), pp. 671–676. DOI: 10.1063/1.1541021.

[12] N. Bian et al. "The quasilinear behavior of convective turbulence with sheared flows". In: *Phys. Plasmas* 10.5 (2003), pp. 1382–1388. DOI: 10.1063/1.1566442.

[13] Henk Broer et al. *Bifurcations in Hamiltonian Systems.* Vol. 1806. Lecture Notes in Mathematics. Springer Berlin Heidelberg, 2003. DOI: 10.1007/b10414.

[14] Morten Brøns. "Streamline Topology: Patterns in Fluid Flows and their Bifurcations". In: *Adv. Appl. Mech.* 41 (2007), pp. 1–42. DOI: 10.1016/S0065-2156(07)41001-8.

[15] Morten Brøns, Lars Køllgaard Voigt, and Jens Nørkær Sørensen. "Streamline topology of steady axisymmetric vortex breakdown in a cylinder with co- and counter-rotating end-covers". In: *J. Fluid Mech.* 401 (1999), pp. 275–292. DOI: 10.1017/S0022112099006588.

[16] Morten Brøns et al. "Streamline topology in the near wake of a circular cylinder at moderate Reynolds numbers". In: *J. Fluid Mech.* 584 (2007), pp. 23–43. DOI: 10.1017/S0022112007006234.

[17] Steven L. Brunton, Joshua L. Proctor, and J. Nathan Kutz. "Discovering governing equations from data by sparse identification of nonlinear dynamical systems". In: *Proc. Natl. Acad. Sci. U.S.A.* 113.15 (2016), pp. 3932–3937. DOI: 10.1073/pnas.1517384113.

[18] Francis F. Chen. *An Indispensable Truth. How Fusion Power Can Save the Planet.* Springer New York, 2011. DOI: 10.1007/978-1-4419-7820-2.

[19] Francis F. Chen. *Introduction to Plasma Physics and Controlled Fusion.* Springer International Publishing, 2016. DOI: 10.1007/978-3-319-22309-4.

[20] COMSOL. *COMSOL Multiphysics® v. 5.3.* COMSOL AB, Stockholm, Sweden. 2017. URL: http://www.comsol.com.

[21] D. A. D'Ippolito, J. R. Myra, and S. J. Zweben. "Convective transport by intermittent blob-filaments: Comparison of theory and experiment". In: *Phys. Plasmas* 18.6 (2011), p. 060501. DOI: 10.1063/1.3594609.

[22] Magnus Dam et al. "Bifurcation analysis and dimension reduction of a predator-prey model for the L-H transition". In: *Phys. Plasmas* 20.10, 102302 (2013). DOI: 10.1063/1.4823719.

[23] Magnus Dam et al. "Sparse identification of a predator-prey system from simulation data of a convection model". In: *Phys. Plasmas* 24.2 (2017), p. 022310. DOI: 10.1063/1.4977057.

[24] Magnus Dam et al. "Topological bifurcations in the evolution of coherent structures in a convection model". In: *Phys. Plasmas* 24.8 (2017), p. 082301. DOI: 10.1063/1.4993613.

[25] L. Easy et al. "Three dimensional simulations of plasma filaments in the scrape off layer: A comparison with models of reduced dimensionality". In: *Phys. Plasmas* 21.12 (2014), p. 122515. DOI: 10.1063/1.4904207.

[26] V. Erckmann et al. "H mode of the W 7-AS stellarator". In: *Phys. Rev. Lett.* 70 (14 Apr. 1993), pp. 2086–2089. DOI: 10.1103/PhysRevLett.70.2086.

[27] Jeffrey P. Freidberg. *Plasma Physics and Fusion Energy*. Cambridge University Press, 2007. DOI: 10.1017/CBO9780511755705.

[28] W. Fundamenski. "Power and particle exhaust in tokamaks: Integration of plasma scenarios with plasma facing materials and components". In: *J. Nucl. Mater.* 390–391.1 (2009), pp. 10–19. DOI: 10.1016/j.jnucmat.2009.01.038.

[29] Wojciech Fundamenski. *Power Exhaust in Fusion Plasmas*. Cambridge University Press, 2009. DOI: 10.1017/CBO9780511770609.

[30] O. E. Garcia, N. H. Bian, and W. Fundamenski. "Radial interchange motions of plasma filaments". In: *Phys. Plasmas* 13.8 (2006), p. 082309. DOI: 10.1063/1.2336422.

[31] O. E. Garcia et al. "Confinement and bursty transport in a flux-driven convection model with sheared flows". In: *Plasma Phys. and Control. Fusion* 45.6 (2003), p. 919. DOI: 10.1088/0741-3335/45/6/306.

[32] O. E. Garcia et al. "Interchange turbulence in the TCV scrape-off layer". In: *Plasma Phys. Control. Fusion* 48.1 (2006), p. L1. DOI: 10.1088/0741-3335/48/1/101.

[33] O. E. Garcia et al. "Mechanism and scaling for convection of isolated structures in nonuniformly magnetized plasmas". In: *Phys. Plasmas* 12.9 (2005), p. 090701. DOI: 10.1063/1.2044487.

[34] O. E. Garcia et al. "Turbulence and intermittent transport at the boundary of magnetized plasmas". In: *Phys. Plasmas* 12.6, 062309 (2005). DOI: 10.1063/1.1925617.

[35] O. E. Garcia et al. "Turbulence simulations of blob formation and radial propagation in toroidally magnetized plasmas". In: *Phys. Scr.* T122 (2006), pp. 89–103. DOI: 10.1088/0031-8949/2006/t122/013.

[36] O. E. Garcia et al. "Two-dimensional convection and interchange motions in fluids and magnetized plasmas". In: *Phys. Scr.* T122 (2006), pp. 104–124. DOI: 10.1088/0031-8949/2006/t122/014.

[37] Alexander V. Getling. *Rayleigh-Bénard Convection - Structures and Dynamics*. Vol. 11. Advanced Series in Nonlinear Dynamics. World Scientific, 1998. DOI: 10.1142/3097.

[38] Ö. D. Gürcan and P. H. Diamond. "Zonal flows and pattern formation". In: *J. Phys. A: Math. Theor.* 48.29 (2015), p. 293001. DOI: 10.1088/1751-8113/48/29/293001.

[39] Federico D. Halpern et al. "Three-dimensional simulations of blob dynamics in a simple magnetized torus". In: *Phys. Plasmas* 21.2 (2014), p. 022305. DOI: 10.1063/1.4864324.

[40] Heinz Hanßmann. *Local and Semi-Local Bifurcations in Hamiltonian Dynamical Systems*. Vol. 1893. Lecture Notes in Mathematics. Springer Berlin Heidelberg, 2007. DOI: 10.1007/3-540-38894-X.

[41] R. D. Hazeltine and J. D. Meiss. *Plasma Confinement*. Dover Publications, 2003.

[42] Matthias Heil et al. "Topological fluid mechanics of the formation of the Kármán-vortex street". In: *J. Fluid Mech.* 812 (2017), pp. 199–221. DOI: 10.1017/jfm.2016.792.

[43] M. Held et al. "The influence of temperature dynamics and dynamic finite ion Larmor radius effects on seeded high amplitude plasma blobs". In: *Nucl. Fusion* 56.12 (2016), p. 126005. DOI: 10.1088/0029-5515/56/12/126005.

[44] J. Juul Rasmussen et al. "Numerical modeling of the transition from low to high confinement in magnetically confined plasma". In: *Plasma Phys. Control. Fusion* 58.1 (2016), p. 014031. DOI: 10.1088/0741-3335/58/1/014031.

[45] J. Kasten et al. "Acceleration feature points of unsteady shear flows". eng. In: *Arch. Mech.* 68.1 (2016), pp. 55–80. URL: http://am.ippt.pan.pl/am/article/view/v68p55.

[46] Eun-jin Kim and P. H. Diamond. "Mean shear flows, zonal flows, and generalized Kelvin–Helmholtz modes in drift wave turbulence: A minimal model for L-H transition". In: *Phys. Plasmas* 10.5 (2003), pp. 1698–1704. DOI: 10.1063/1.1559006.

[47] Eun-jin Kim and P. H. Diamond. "Zonal Flows and Transient Dynamics of the *L-H* Transition". In: *Phys. Rev. Lett.* 90 (18 May 2003), p. 185006. DOI: 10.1103/PhysRevLett.90.185006.

[48] Sumire Kobayashi, Özgür D. Gürcan, and Patrick H. Diamond. "Direct identification of predator-prey dynamics in gyrokinetic simulations". In: *Phys. Plasmas* 22.9, 090702 (2015). DOI: 10.1063/1.4930127.

[49] R. Kube and O. E. Garcia. "Effect of dynamical friction on interchange motion of plasma filaments". In: *Phys. Plasmas* 19.4 (2012), p. 042305. DOI: 10.1063/1.4704793.

[50] R. Kube and O. E. Garcia. "Velocity scaling for filament motion in scrape-off layer plasmas". In: *Phys. Plasmas* 18.10 (2011), p. 102314. DOI: 10.1063/1.3647553.

[51] R. Kube, O. E. Garcia, and M. Wiesenberger. "Amplitude and size scaling for interchange motions of plasma filaments". In: *Phys. Plasmas* 23.12 (2016), p. 122302. DOI: 10.1063/1.4971220.

[52] Wonjae Lee et al. "Electromagnetic effects on dynamics of high-beta filamentary structures". In: *Phys. Plasmas* 22.1 (2015), p. 012505. DOI: 10.1063/1.4905639.

[53] Lennart Ljung. *System Identification: Theory for the user*. 2nd. Prentice-hall Information and System Sciences Series. Prentice Hall, 1999.

[54] Lennart Ljung and Torkel Glad. *Modeling of Dynamic Systems*. Prentice-hall Information and System Sciences Series. Prentice Hall, 1994.

[55] Jens Madsen et al. "The influence of finite Larmor radius effects on the radial interchange motions of plasma filaments". In: *Phys. Plasmas* 18.11 (2011), p. 112504. DOI: 10.1063/1.3658033.

[56] M. A. Malkov and P. H. Diamond. "Weak hysteresis in a simplified model of the L-H transition". In: *Phys. Plasmas* 16.1, 012504 (2009). DOI: 10.1063/1.3062834.

[57] N. M. Mangan et al. "Inferring Biological Networks by Sparse Identification of Nonlinear Dynamics". In: *IEEE Trans. Mol. Biol. Multi-Scale Commun.* 2.1 (June 2016), pp. 52–63. DOI: 10.1109/TMBMC.2016.2633265.

[58] James D. Meiss. *Differential Dynamical Systems*. Vol. 14. Mathematical Modeling and Computation. Society for Industrial and Applied Mathematics, 2007. DOI: 10.1137/1.9780898718232.

[59] K. Miki et al. "Spatio-temporal evolution of the H-L back transition". In: *Phys. Plasmas* 20.6, 062304 (2013). DOI: 10.1063/1.4812555.

[60] K. Miki et al. "Spatio-temporal evolution of the L-I-H transition". In: *Phys. Plasmas* 19.9, 092306 (2012). DOI: 10.1063/1.4753931.

[61] Kenro Miyamoto. *Plasma Physics for Controlled Fusion*. 2nd. Springer Berlin Heidelberg, 2016. DOI: 10.1007/978-3-662-49781-4.

[62] P. Morel, Ö. D. Gürcan, and V. Berionni. "Characterization of predator–prey dynamics, using the evolution of free energy in plasma turbulence". In: *Plasma Phys. Control. Fusion* 56.1 (2014), p. 015002. DOI: 10.1088/0741-3335/56/1/015002.

[63] Peter Müller. *The Equations of Oceanic Motions*. Cambridge University Press, 2006. DOI: 10.1017/cbo9780511617843.

[64] J. R. Myra et al. "Edge sheared flows and the dynamics of blob-filaments". In: *Nucl. Fusion* 53.7 (2013), p. 073013. DOI: 10.1088/0029-5515/53/7/073013.

[65] A. H. Nielsen et al. "Numerical simulations of blobs with ion dynamics". In: *Plasma Phys. Control. Fusion* 59.2 (2017), p. 025012. DOI: 10.1088/1361-6587/59/2/025012.

[66] Jeppe Olsen et al. "Temperature dynamics and velocity scaling laws for interchange driven, warm ion plasma filaments". In: *Plasma Phys. Control. Fusion* 58.4 (2016), p. 044011. DOI: 10.1088/0741-3335/58/4/044011.

[67] J. T. Omotani et al. "The effects of shape and amplitude on the velocity of scrape-off layer filaments". In: *Plasma Phys. Controlled Fusion* 58.1 (2016), p. 014030. DOI: 10.1088/0741-3335/58/1/014030.

[68] H. Sugama and W. Horton. "L-H confinement mode dynamics in three-dimensional state space". In: *Plasma Phys. and Control. Fusion* 37.3 (1995), p. 345. DOI: 10.1088/0741-3335/37/3/012.

[69] F. Wagner. "A quarter-century of H-mode studies". In: *Plasma Phys. Control. Fusion* 49.12B (2007), B1. DOI: 10.1088/0741-3335/49/12b/s01.

[70] F. Wagner et al. "Regime of Improved Confinement and High Beta in Neutral-Beam-Heated Divertor Discharges of the ASDEX Tokamak". In: *Phys. Rev. Lett.* 49 (19 Nov. 1982), pp. 1408–1412. DOI: 10.1103/PhysRevLett.49.1408.

[71] N. R. Walkden, B. D. Dudson, and G. Fishpool. "Characterization of 3D filament dynamics in a MAST SOL flux tube geometry". In: *Plasma Phys. Control. Fusion* 55.10 (2013), p. 105005. DOI: 10.1088/0741-3335/55/10/105005.

[72] N. R. Walkden et al. “Dynamics of 3D isolated thermal filaments”. In: *Plasma Phys. Controlled Fusion* 58.11 (2016), p. 115010. DOI: 10.1088/0741-3335/58/11/115010.

[73] N. R. Walkden et al. “Numerical investigation of isolated filament motion in a realistic tokamak geometry”. In: *Nucl. Fusion* 55.11 (2015), p. 113022. DOI: 10.1088/0029-5515/55/11/113022.

[74] Wen-Xu Wang et al. “Predicting Catastrophes in Nonlinear Dynamical Systems by Compressive Sensing”. In: *Phys. Rev. Lett.* 106 (15 Apr. 2011), p. 154101. DOI: 10.1103/PhysRevLett.106.154101.

[75] M. Wiesenberger, J. Madsen, and A. Kendl. “Radial convection of finite ion temperature, high amplitude plasma blobs”. In: *Phys. Plasmas* 21.9 (2014), p. 092301. DOI: 10.1063/1.4894220.

[76] Stephen Wiggins. *Introduction to Applied Nonlinear Dynamical Systems and Chaos*. Vol. 2. Texts in Applied Mathematics. Springer-Verlag New York, 2003. DOI: 10.1007/b97481.

[77] Xingquan Wu et al. “One-dimensional modelling of limit-cycle oscillation and H-mode power scaling”. In: *Nucl. Fusion* 55.5 (2015), p. 053029. DOI: 10.1088/0029-5515/55/5/053029.

[78] G. S. Xu et al. “Study of the L–I–H transition with a new dual gas puff imaging system in the EAST superconducting tokamak”. In: *Nucl. Fusion* 54.1 (2014), p. 013007. DOI: 10.1088/0029-5515/54/1/013007.

[79] H. Zhu, S. C. Chapman, and R. O. Dendy. “Robustness of predator-prey models for confinement regime transitions in fusion plasmas”. In: *Phys. Plasmas* 20.4, 042302 (2013). DOI: 10.1063/1.4800009.

[80] H. Zhu et al. “Transitions to improved confinement regimes induced by changes in heating in zero-dimensional models for tokamak plasmas”. In: *Phys. Plasmas* 21.6, 062307 (2014). DOI: 10.1063/1.4884126.

[81] P. Zhu, C. R. Sovinec, and C. C. Hegna. “The formation of blobs from a pure interchange process”. In: *Phys. Plasmas* 22.2 (2015), p. 022311. DOI: 10.1063/1.4913476.